

Searches for continuous gravitational waves from neutron stars: A twenty-year retrospective

Karl Wette^{a,b}

^aCentre for Gravitational Astrophysics, Australian National University, Canberra, ACT, 2601, Australia

^bAustralian Research Council Centre of Excellence for Gravitational Wave Discovery (OzGrav), Hawthorn, VIC, 3122, Australia

Abstract

Seven years after the first direct detection of gravitational waves, from the collision of two black holes, the field of gravitational wave astronomy is firmly established. A first detection of continuous gravitational waves from rapidly-spinning neutron stars could be the field's next big discovery. I review the last twenty years of efforts to detect continuous gravitational waves using the LIGO and Virgo gravitational wave detectors. I summarise the model of a continuous gravitational wave signal, the challenges to finding such signals in noisy data, and the data analysis algorithms that have been developed to address those challenges. I present a quantitative analysis of 297 continuous wave searches from 80 papers, published from 2003 to 2022, and compare their sensitivities and coverage of the signal model parameter space.

Keywords: gravitational waves, neutron stars, data analysis

1. Introduction

Together with a young collaborator, I arrived at the interesting result that gravitational waves do not exist, though they had been assumed a certainty to the first approximation. This shows that the non-linear general relativistic field equations can tell us more or, rather, limit us more than we have believed up to now.

Einstein, in a letter to Born, 1936 [1].

Progress in science is rarely, if ever, a story of uninterrupted success; rather, a journey of trial and error, initial presumptions giving way to new discoveries. The century-long study of gravitational waves, from theoretical conjecture in 1916 [2, 3] to direct detection in 2015 [4], certainly follows this template. On that difficult journey, it is understandable that even Einstein at one time doubted their existence [5]; yet it is just as well that his initial predictions have stood. Gravitational waves – wave-like solutions to the Einstein field equations – are fulfilling their promise to “tell us more” about the Universe that could be achieved through traditional astronomy. Analysis of the growing catalogue of detections of gravitational waves from colliding pairs of black holes and neutron stars [6–10] by the LIGO and Virgo detectors [11, 12] has, e.g.: confirmed the existence of stellar-mass black holes [4]; strengthened links between the merger of binary neutron stars, short-hard gamma-ray bursts, kilonovae, and the production of

heavy elements [13]; yielded insights into the mass spectrum of black holes, and by inference their stellar progenitors [14, 15]; and opened an independent avenue towards resolving tensions in cosmology regarding measurement of the Hubble constant [16–18].

As well as the important discoveries and insights from observing binary black hole and neutron star mergers, it is hoped that the gravitational wave view of the Universe will continue to widen in the coming years. Perhaps we will observe the gravitational aftermath of a supernova, the faint hum of gravitational waves from rapidly-spinning neutron stars, signatures of dark matter or particles beyond the Standard Model, or the even fainter murmur of gravitational waves from the very early Universe. It is the second of these – the search for so-called *continuous gravitational waves* – that is the subject of this review.

General relativity predicts gravitational waves from an astronomical body only when it possesses a time-varying quadrupole moment. As an example, if the body is not symmetric about its rotation axis, so that the distribution of its mass is seen to “move” when rotated, its *mass* quadrupole moment will vary with time. (Velocity perturbations within the star may also give rise to a time-varying *current* quadrupole moment; see Sec. 2.1.3.) While the orbit of neutron stars or black holes around each other presents an obvious asymmetry, the extent to which a single neutron may sustain a non-axisymmetric shape is expected to be much smaller [19, 20]. It is assumed that all neutron stars possess a magnetic field [21] which, so long as it is not aligned with the star's rotation axis, will distort the star in a non-axisymmetric way [22]. It is likely therefore that all neutron stars radiate *some* continuous gravitational waves. It remains to be discovered, however,

Email address: karl.wette@anu.edu.au (Karl Wette)

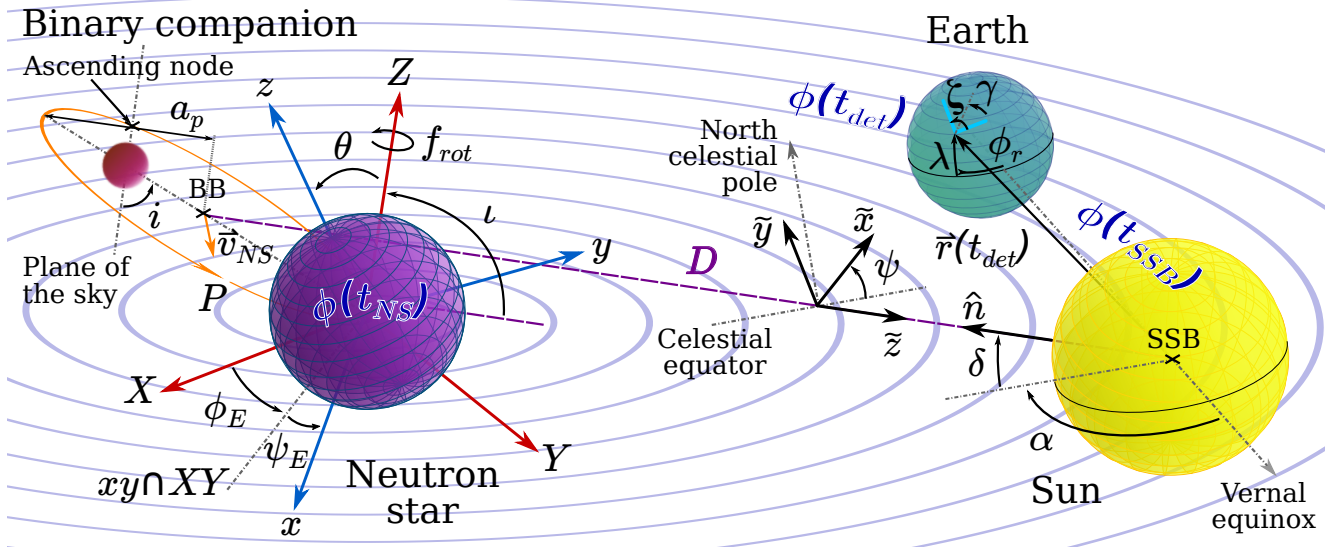


Figure 1: CW signal model, illustrated by a rigidly rotating neutron star with a possible binary companion. Parameters are: f_{rot} is the rotation frequency of the star; (ϕ_E, θ, ψ_E) orient the body frame (x, y, z) with respect to an inertial frame (X, Y, Z) ; (a_p, P) are the projected semi-major axis and period of the neutron star’s orbit around the binary companion, if present; \vec{v}_{NS} is the linear velocity of the neutron star, or of the binary barycentre (BB) if a binary companion is present; \hat{n} is a unit vector pointing from the Solar System barycentre (SSB) to the neutron star or BB; ι is the angle from the line of sight (parallel to \hat{n}) to the inertial Z axis; D is the distance from the SSB to the neutron star or BB; (α, δ, ψ) orient the wave frame $(\tilde{x}, \tilde{y}, \tilde{z})$ in equatorial coordinates; $\vec{r}(t_{\text{det}})$ denotes the position of the detector with respect to the SSB; $(\phi_r, \lambda, \gamma)$ orient the interferometric detector with respect to the Earth; and ζ is the angle between the interferometer arms. The CW signal phase at the neutron star, SSB, and detector are labelled $\phi(t_{\text{NS}})$, $\phi(t_{\text{SSB}})$, and $\phi(t_{\text{det}})$ respectively.

whether the strength of those waves – arising either from magnetic distortion, or through some other mechanism – is sufficient to be *detectable* using the instruments and data analysis techniques available to us.

In this review I look back at the last twenty years of searches for continuous gravitational waves (CWs). I begin in Sec. 2 with an overview of the CW signal model. I then discuss the many challenges faced by CW searches in Sec. 3, and suggest metrics by which we may compare their performance in Sec. 4. After a brief summary of gravitational wave detectors and observations (Sec. 5), I review CW searches performed from 2003 to 2022 in Sec. 6, and the algorithms employed by those searches in Sec. 7. I conclude with a summary, and suggestions for further reading, in Sec. 8.

2. Continuous wave signal model

Figure 1 gives an overview of the CW signal model. Gravitational waves in general relativity exist in two polarisations: *plus* and *cross*. A gravitational wave is modelled as a time series $h(t)$ in the calibrated output of a gravitational wave detector:

$$h(t) = F_+(t)h_+(t) + F_\times(t)h_\times(t). \quad (1)$$

The functions $F_+(t)$ and $F_\times(t)$ are the responses of the detector to each polarisation. These depend on the polarisation basis $(\tilde{x}, \tilde{y}, \tilde{z})$, oriented by the polarisation angle ψ , and a model of the response of the detector to a gravitational wave. An interferometric detector may be

described [23] by its location on Earth – its latitude λ , and local sidereal time ϕ_r at a given reference time – the orientation of its arms γ and the angle ζ between them.

A CW signal is described by the two functions $h_+(t)$ and $h_\times(t)$ in terms of numerous parameters (Fig. 1). Conventionally the CW signal parameters are divided into: *amplitude parameters* (Sec. 2.1), which control the overall amplitude of the signal; and *phase parameters* (Sec. 2.2), which control its phase.

2.1. Amplitude parameters

The basic model of a CW source is a rotating, non-axisymmetrically-deformed neutron star which generates gravitational waves through a time-changing mass quadrupole (Sec. 2.1.1). It is assumed that the non-axisymmetry is *rigid*, i.e. does not change over typical observation periods. As a result, the CW amplitude parameters of this model may be considered independently of the precise mechanism responsible for the deformation. Extensions to the basic model are free precession (Sec. 2.1.2), *r*-mode oscillations (Sec. 2.1.3), and accretion from a binary companion star (Sec. 2.1.4).

2.1.1. Rigidly rotating stars

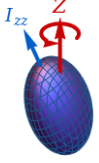
Provided that its internal velocities are non-relativistic, a rigidly-rotating neutron star is described by its classical moment of inertia tensor I_{ij} [25–27]. A reference frame (x, y, z) may always be found in which I_{ij} is diagonal; the diagonal elements are the principal moments I_{xx} , I_{yy} , and

Table 1: CW signal amplitude parameters, for the general case, and for the biaxial, triaxial aligned, and r -mode oscillations cases. Expressions are given for: the amplitudes C_{22}, C_{21} and initial phases Φ_{22}^C, Φ_{21}^C of the $l = 2, m = 2$ and $l = 2, m = 1$ harmonics, respectively; and for the gravitational wave luminosity \dot{E}_{GW} . The graphics at left illustrate the shape and orientation of the neutron star for the rigidly rotating star cases; for the r -mode case, the pattern on the neutron star surface is proportional to the r -mode velocity perturbations [24].

Triaxial non-aligned (general case); see Sec. 2.1.1

$$C_{22} = \frac{1}{2} \left[h_0^2 \cos^4 \theta \cos^4 \psi_E + (h_p \sin^2 \theta - h_0 \sin^2 \psi_E)^2 + 2h_0(h_p \sin^2 \theta + h_0 \sin^2 \psi_E) \cos^2 \theta \cos^2 \psi_E \right]^{1/2}, \quad (\text{T1.1})$$

$$C_{21} = \frac{1}{2} \left[h_0^2 \sin^2 \theta \sin^2 2\psi_E + \frac{1}{4}(h_0 \cos 2\psi_E + h_0 - 2h_p)^2 \sin^2 2\theta \right]^{1/2},$$

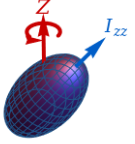


$$\tan(2\phi_E - \Phi_{22}^C) = \frac{h_0 \cos \theta \sin 2\psi_E}{h_0 \sin^2 \psi_E - h_p \sin^2 \theta - h_0 \cos^2 \theta \cos^2 \psi_E}, \quad (\text{T1.2})$$

$$\tan(\phi_E - \Phi_{21}^C) = \cos \theta \left[\cot \psi_E - \frac{2h_p}{h_0} \csc 2\psi_E \right],$$

$$\dot{E}_{\text{GW}} = \frac{\pi^2 c^3}{10G} (64C_{22}^2 + C_{21}^2) D^2 f_{\text{rot}}^2. \quad (\text{T1.3})$$

Biaxial ($h_0 = 0$); see Sec. 2.1.1



$$C_{22} = \frac{1}{2} h_p \sin^2 \theta, \quad C_{21} = \frac{1}{2} h_p \sin 2\theta, \quad (\text{T1.4})$$

$$\Phi_{22}^C = 2\phi_E + \pi = 2\Phi_0 + \pi, \quad \Phi_{21}^C = \phi_E + \frac{\pi}{2} = \Phi_0 + \pi, \quad (\text{T1.5})$$

$$\dot{E}_{\text{GW}} = \frac{8\pi^2 c^3}{5G} \Theta D^2 f_{\text{rot}}^2 h_p^2 = \frac{2048\pi^6 G}{5c^5} \Theta I_{zz}^2 \epsilon_p^2 f_{\text{rot}}^6, \quad \Theta = \frac{(17 - 15 \cos 2\theta) \sin^2 \theta}{32}. \quad (\text{T1.6})$$

Triaxial aligned ($\theta = 0$); see Sec. 2.1.1

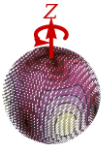


$$C_{22} = \frac{1}{2} h_0, \quad C_{21} = 0, \quad (\text{T1.7})$$

$$\Phi_{22}^C = 2(\phi_E + \psi_E) = \phi_0 + \pi, \quad (\text{T1.8})$$

$$\dot{E}_{\text{GW}} = \frac{2\pi^2 c^3}{5G} D^2 f^2 h_0^2 = \frac{32\pi^6 G}{5c^5} I_{zz}^2 \epsilon^2 f^6. \quad (\text{T1.9})$$

r -mode; see Sec. 2.1.3



$$C_{22} = \frac{1}{2} h_\alpha, \quad C_{21} = 0, \quad (\text{T1.10})$$

$$\Phi_{22}^C = \phi_0 + \pi, \quad (\text{T1.11})$$

$$\dot{E}_{\text{GW}} = \frac{1024\pi^9 G}{25c^7} \alpha^2 \tilde{J}^2 M^2 R^6 f_\alpha^8. \quad (\text{T1.12})$$

I_{zz} . Examining whether or not the principal moments are equal to each other leads to three equivalence classes:

1. $I_{xx} = I_{yy} = I_{zz}$: If all three principal moments are equal, the star is symmetric, and no gravitational waves are emitted.
2. $I_{xx} = I_{yy} \neq I_{zz}$: If two principal moments (conventionally I_{xx} and I_{yy}) are equal, the star is *biaxial*. The degree of deformation along the z axis is characterised by the *poloidal ellipticity*

$$\epsilon_p = \frac{|I_{xx} - I_{zz}|}{I_{zz}}. \quad (2)$$

3. $I_{xx} \neq I_{yy} \neq I_{zz}$: If no principal moments are equal, the star is *triaxial*. In addition to ϵ_p , the degree of deformation perpendicular to the z axis is characterised by the *equatorial ellipticity*

$$\epsilon = \frac{|I_{xx} - I_{yy}|}{I_{zz}}. \quad (3)$$

The body frame (x, y, z) is related to an inertial frame (X, Y, Z) , where the star rotates about the Z axis.

The general form of the CW signal, following the no-

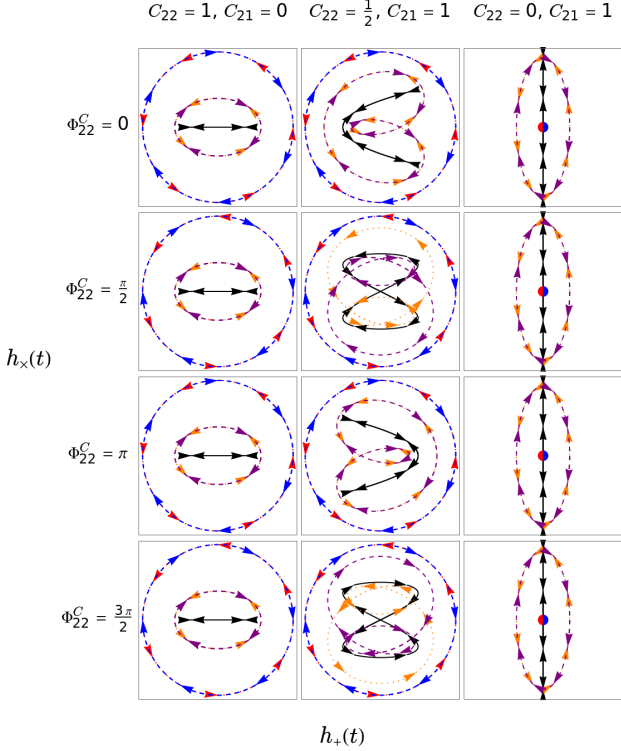


Figure 2: CW signal polarisations $h_{\times}(t)$ versus $h_{+}(t)$, for selected values of C_{22}, C_{21} (columns), and of Φ_{22}^C (rows), with $\Phi_{21}^C = 0$, and with $\iota = 0$ (red, dotted), $\iota = 3\pi/8$ (orange, dotted), $\iota = \pi/2$ (black, solid), $\iota = 5\pi/8$ (purple, dashed), and $\iota = \pi$ (blue, dashed). Arrows indicate the direction of time. Note that the scales of the plots in each column are 4 to 2 to 1 (left to right).

tation of [28–30] (cf. [31]), is

$$h_{+}(t) = -C_{22}(1 + \cos^2 \iota) \cos[2\phi_{\text{rot}}(t) + \Phi_{22}^C] - \frac{1}{2}C_{21} \sin \iota \cos \iota \cos[\phi_{\text{rot}}(t) + \Phi_{21}^C], \quad (4)$$

$$h_{\times}(t) = -2C_{22} \cos \iota \sin[2\phi_{\text{rot}}(t) + \Phi_{22}^C] - \frac{1}{2}C_{21} \sin \iota \sin[\phi_{\text{rot}}(t) + \Phi_{21}^C]. \quad (5)$$

The inclination angle ι is measured from the line of sight (Fig. 1) and its angular momentum vector (which is assumed parallel to the Z axis). The CW signal contains two harmonics, with amplitudes C_{22}, C_{21} and initial phases Φ_{22}^C, Φ_{21}^C , corresponding to the $l = 2, m = 2$ and $l = 2, m = 1$ spherical harmonic components of the mass quadrupole, respectively. The time-dependent phase of the signal scales as $\phi_{\text{rot}}(t) \sim 2\pi f_{\text{rot}} t$ where f_{rot} is the rotation frequency of the star (Sec. 2.2); the two harmonics are therefore at approximately once and twice the star’s rotation frequency. Equations (4) and (5) give the most general form of the signal, and may be specialised [22, 23, 32–34] to particular relationships between (I_{xx}, I_{yy}, I_{zz}) and orientations of (x, y, z) , as discussed in this section.

Figure 2 illustrates the polarisation state of the CW signal. We see that the C_{22} harmonic generates linearly-

polarised waves when $\iota = \pi/2$, right-hand (left-hand) circularly-polarised waves when $\iota = 0$ ($\iota = \pi$), and elliptically-polarised waves at other values of ι . In contrast, the C_{21} harmonic disappears when $\iota \in \{0, \pi\}$, and is linearly polarised (when $\iota = \pi/2$) at right angles to the C_{22} harmonic. When both harmonics are present, emission is still circularly polarised at $\iota \in \{0, \pi\}$ (as the C_{21} harmonic disappears here), and is otherwise non-elliptical in nature.

Table 1 lists expressions for $C_{22}, C_{21}, \Phi_{22}^C$, and Φ_{21}^C [29, 30]. I have given these expressions in terms of the following quantities (cf. [23, 31]):

$$h_0 = \frac{4\pi^2 G}{c^4 D} I_{zz} \epsilon f^2, \quad f = 2f_{\text{rot}}, \quad (6)$$

$$h_p = \frac{16\pi^2 G}{c^4 D} I_{zz} \epsilon_p f_{\text{rot}}^2. \quad (7)$$

Equation (6) is familiar from [23] as the characteristic CW amplitude in the most commonly assumed triaxial aligned case (see below). Note that h_0 is occasionally re-defined in terms of ϵ_p [e.g. 23, 31]; in this review I define h_0 solely as in Eq. (6), and introduce h_p as the equivalent amplitude in terms of ϵ_p . Similarly, in this review f (often referred to as the “gravitational wave frequency” in the context of the triaxial aligned case) is always equal to twice the rotation frequency f_{rot} .

The top panel in Table 1 is for the general case of a *triaxial non-aligned* star, where $I_{xx} \neq I_{yy} \neq I_{zz}$, and the body frame (x, y, z) is orientated arbitrarily with respect to the inertial frame (X, Y, Z) . This orientation is specified by three Euler angles ([28–30], see Fig. 1): ϕ_E ¹ specifies an initial rotation about z , θ gives the inclination of z with respect to Z and ψ_E ² gives the orientation of the x - y plane about z with respect to the X - Y plane.

A triaxial non-aligned star may in general radiate CWs at both $f = 2f_{\text{rot}}$ and f_{rot} , depending on their respective amplitudes C_{22} and C_{21} [Table 1, Eqs. (T1.1)]. Figure 3 shows C_{22}, C_{21} as functions of θ and ψ_E , for 5 choices of h_0, h_p : h_0 only, $h_0 = 2h_p$, $h_0 = h_p$, $h_p = 2h_0$, and h_p only. (The h_0, h_p are normalised so that $h_0^2 + h_p^2 = 1$.) We see that C_{22}, C_{21} exhibit periodicities over θ, ψ_E , with periods [29, 30] depending on the relative contribution to the CW signal from equatorial ($h_0 \propto \epsilon$) and poloidal ($h_p \propto \epsilon_p$) deformations. The gravitational wave luminosity from a triaxial non-aligned star is given by Eq. (T1.3); for equivalent amplitudes ($C_{22} \approx C_{21}$), the f harmonic is much more efficient at radiating energy than the f_{rot} harmonic [36]. (Note that, as $C_{22}, C_{21} \propto 1/D$, \dot{E}_{GW} is independent of distance.)

When h_0 is zero, C_{22}, C_{21} are independent of ψ_E (Fig. 3, rightmost column). This gives the case of a *biaxial* star

¹I use ϕ_E for this angle in preference to the ϕ_0 of [28–30] to avoid confusion, since this convention differs from other conventions [e.g. 23, 35] which also use ϕ_0 or similar notations.

²I use ψ_E for this angle in preference to the ψ of [28, 29] and the λ of [30], to avoid confusion in Fig. 1 with the polarisation angle and the detector latitude respectively.

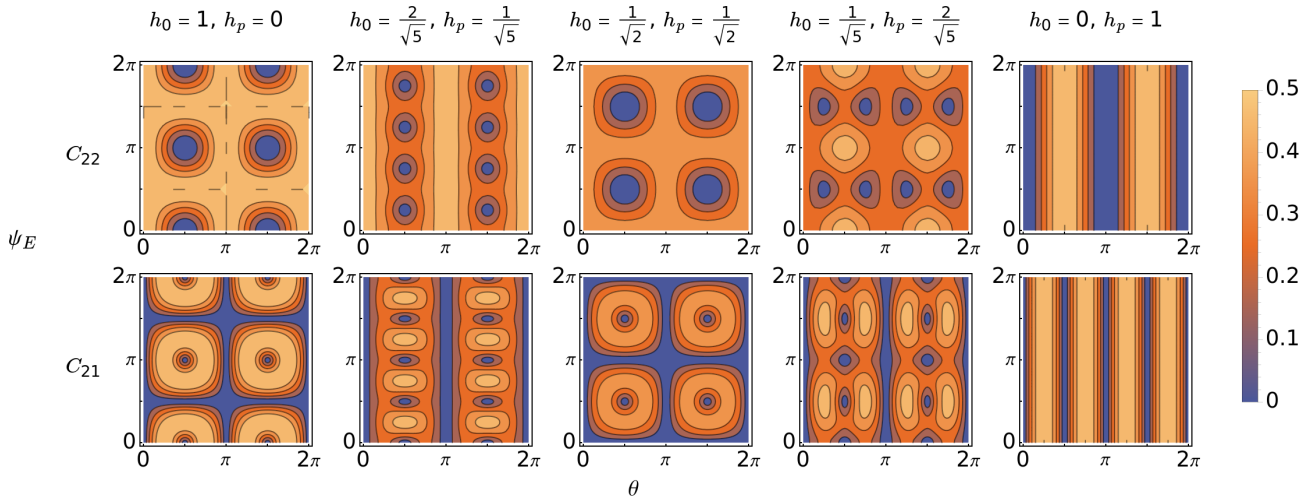


Figure 3: CW signal amplitudes C_{22} (top row), C_{21} (bottom row) as functions of θ, ψ_E for selected values of h_0, h_p (columns).

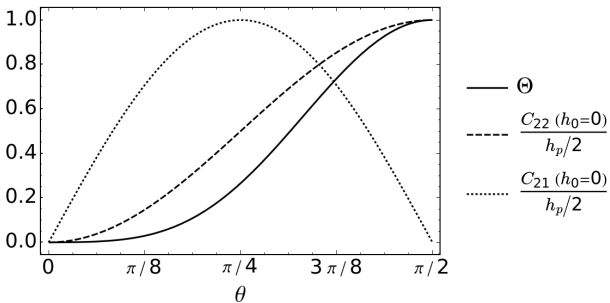


Figure 4: C_{22}, C_{21} , and Θ for a biaxial star as functions of θ .

(2nd panel, Table 1), which is only deformed poloidally. Here the amplitudes C_{22} and C_{21} [Eqs. (T1.4)] simplify to expressions involving only h_p and θ . Figure 4 plots C_{22}, C_{21} (normalised by $h_p/2$) as a function of θ . Emission at f_{rot} is maximal at $\theta = \pi/4$, but disappears at $\theta = \pi/2$; emission at f , however, grows monotonically with θ . The gravitational wave luminosity is proportional to a quantity $\Theta(\theta)$ [Eqs. (T1.6)], plotted in Fig. 4, and is maximal when $\Theta = 1$ at $\theta = \pi/2$.

When one of the body frame axes (conventionally z) aligns with the inertial frame Z axis, $\theta = 0$ and the star rotates about a principal moment of inertia. Such a *triaxial aligned* star emits only at f (3rd panel, Table 1); $C_{21} = 0$, and C_{22} is given in terms of the familiar h_0 . Were such a star also biaxial, rotations about $z = Z$ would be axisymmetric, and there would be no CW emission.

Different conventions exist for defining an overall initial phase. For the biaxial case, Eq. (T1.5) (Table 1) relates ϕ_E [30, Eqs. (A9), (A12), and (A16)] to the Φ_0 of [23]. Note that $\phi_E + \pi/2$ and Φ_0 differ by a factor of π , consistent with the overall negative sign of Eqs. (4) and (5) compared to [23, Eqs. (21) and (22)]. For the triaxial aligned case, Eq. (T1.5) relates ϕ_E to the ϕ_0 of [35].

Equations for the CW amplitudes are often conveniently written with fiducial values for their respective factors. In this review I include a comprehensive set of such expressions, with consistent fiducial values for each factor across all expressions.³ (A Python package [37] also exists for creating and manipulating these type of equations.) Due to typical rounding of fiducial values to a few significant figures, these expressions are less accurate than their exact equivalent equations. Fiducial equations in terms of $D, I_{zz}, f, f_{\text{rot}}$ are given for h_0, h_p :

$$h_0 = 10^{-25} \left(\frac{1 \text{ kpc}}{D} \right) \left(\frac{\epsilon}{1.05 \times 10^{-6}} \right) \times \left(\frac{I_{zz}}{10^{38} \text{ kg m}^2} \right) \left(\frac{f}{300 \text{ Hz}} \right)^2, \quad (8)$$

$$h_p = 10^{-25} \left(\frac{1 \text{ kpc}}{D} \right) \left(\frac{\epsilon_p}{1.05 \times 10^{-6}} \right) \times \left(\frac{I_{zz}}{10^{38} \text{ kg m}^2} \right) \left(\frac{f_{\text{rot}}}{150 \text{ Hz}} \right)^2; \quad (9)$$

for ϵ, ϵ_p :

$$\epsilon = 1.05 \times 10^{-6} \left(\frac{300 \text{ Hz}}{f} \right)^2 \left(\frac{10^{38} \text{ kg m}^2}{I_{zz}} \right) \times \left(\frac{D}{1 \text{ kpc}} \right) \left(\frac{h_0}{10^{-25}} \right), \quad (10)$$

$$\epsilon_p = 1.05 \times 10^{-6} \left(\frac{150 \text{ Hz}}{f_{\text{rot}}} \right)^2 \times \left(\frac{10^{38} \text{ kg m}^2}{I_{zz}} \right) \left(\frac{D}{1 \text{ kpc}} \right) \left(\frac{h_p}{10^{-25}} \right); \quad (11)$$

³Due to the similarities between Eqs. (6) and (7), and the consistent choice of fiducial values (e.g. $f_{\text{rot}} = 150 \text{ Hz}$, $f = 2f_{\text{rot}} = 300 \text{ Hz}$), the fiducial equations for h_0, ϵ will usually be similar to those for h_p, ϵ_p ; nevertheless I include both sets of expressions for clarity.

and for the gravitational wave luminosity:

$$\dot{E}_{\text{GW}} = 1.37 \times 10^{30} \left(\frac{\epsilon}{1.05 \times 10^{-6}} \right)^2 \times \left(\frac{I_{zz}}{10^{38} \text{ kg m}^2} \right)^2 \left(\frac{f}{300 \text{ Hz}} \right)^6 \text{ W}, \quad (12)$$

$$\dot{E}_{\text{GW}} = 1.37 \times 10^{30} \left(\frac{\Theta}{1} \right)^2 \left(\frac{\epsilon_p}{1.05 \times 10^{-6}} \right)^2 \times \left(\frac{I_{zz}}{10^{38} \text{ kg m}^2} \right)^2 \left(\frac{f_{\text{rot}}}{150 \text{ Hz}} \right)^6 \text{ W}. \quad (13)$$

Upper limits on the gravitational wave amplitude may be derived by assuming that gravitational radiation is driven by the rotation of the star [38]. As angular momentum is carried away by gravitational waves, the rotational kinetic energy of the star decreases, and hence its rotation frequency decreases over time. It follows that the gravitational wave luminosity can be no greater than the time derivative of the star's rotational kinetic energy, and this therefore limits the gravitational wave amplitude.

The rotational kinetic energy of a triaxial star is

$$E_{\text{rot}} = 2\pi^2 \left[(I_{xx} \sin^2 \psi_E + I_{yy} \cos^2 \psi_E) \sin^2 \theta + I_{zz} \cos^2 \theta \right] f_{\text{rot}}^2. \quad (14)$$

In the limit of small ϵ, ϵ_p , however, we may approximate $I_{xx} \approx I_{yy} \approx I_{zz}$, and hence $E_{\text{rot}} \approx 2\pi^2 I_{zz} f_{\text{rot}}^2$. The upper limit is then implied by

$$\dot{E}_{\text{GW}} \leq -\dot{E}_{\text{rot}} = -4\pi^2 I_{zz} f_{\text{rot}} \dot{f}_{\text{rot}}, \quad (15)$$

where $\dot{f}_{\text{rot}} = df_{\text{rot}}/dt$ is the (first) *spindown* or time derivative of f_{rot} . Equation (15) defines the *spindown upper limit* on gravitational wave amplitude. Substituting Eqs. (12) and (13) into Eq. (15) gives fiducial equations in terms of \dot{f}_{rot} and $\dot{f} = 2\dot{f}_{\text{rot}}$ for h_0, h_p :

$$h_0 \leq 10^{-25} \left(\frac{1 \text{ kpc}}{D} \right) \left(\frac{300 \text{ Hz}}{f} \right)^{\frac{1}{2}} \times \left(\frac{\dot{f}}{-4.61 \times 10^{-12} \text{ Hz s}^{-1}} \right)^{\frac{1}{2}} \left(\frac{I_{zz}}{10^{38} \text{ kg m}^2} \right)^{\frac{1}{2}}, \quad (16)$$

$$h_p \leq 10^{-25} \left(\frac{1 \text{ kpc}}{D} \right) \left(\frac{150 \text{ Hz}}{f_{\text{rot}}} \right)^{\frac{1}{2}} \left(\frac{1}{\Theta} \right)^{\frac{1}{2}} \times \left(\frac{\dot{f}_{\text{rot}}}{-2.31 \times 10^{-12} \text{ Hz s}^{-1}} \right)^{\frac{1}{2}} \left(\frac{I_{zz}}{10^{38} \text{ kg m}^2} \right)^{\frac{1}{2}}; \quad (17)$$

and for ϵ, ϵ_p :

$$\epsilon \leq 1.05 \times 10^{-6} \left(\frac{300 \text{ Hz}}{f} \right)^{\frac{5}{2}} \left(\frac{10^{38} \text{ kg m}^2}{I_{zz}} \right)^{\frac{1}{2}} \times \left(\frac{\dot{f}}{-4.61 \times 10^{-12} \text{ Hz s}^{-1}} \right)^{\frac{1}{2}}, \quad (18)$$

$$\epsilon_p \leq 1.05 \times 10^{-6} \left(\frac{150 \text{ Hz}}{f_{\text{rot}}} \right)^{\frac{5}{2}} \left(\frac{10^{38} \text{ kg m}^2}{I_{zz}} \right)^{\frac{1}{2}} \times \left(\frac{1}{\Theta} \right)^{\frac{1}{2}} \left(\frac{\dot{f}_{\text{rot}}}{-2.31 \times 10^{-12} \text{ Hz s}^{-1}} \right)^{\frac{1}{2}}. \quad (19)$$

Given an observed value h^{observed} of either h_0 or h_p , the maximum fraction of energy lost in gravitational waves is

$$\frac{\dot{E}_{\text{GW}}}{\dot{E}_{\text{rot}}} = \left(\frac{h^{\text{observed}}}{h^{\text{spindown}}} \right)^2, \quad (20)$$

where h^{spindown} is the right-hand side of either Eqs. (16) or (17) respectively.

The fiducial equations above may be applied when \dot{f}_{rot} is known, e.g. through electromagnetic observations of a pulsar. When \dot{f}_{rot} is unknown, it may be inferred from the following relations [38, 39]:

$$\tau = \frac{1}{n-1} \left(\frac{f_{\text{rot}}}{-\dot{f}_{\text{rot}}} \right), \quad n = \frac{f_{\text{rot}} \dot{f}_{\text{rot}}}{\dot{f}_{\text{rot}}^2}, \quad (21)$$

$$= \frac{1}{n-1} \left(\frac{f}{-\dot{f}} \right), \quad n = \frac{f \dot{f}}{\dot{f}^2}. \quad (22)$$

The *characteristic age* τ is usually approximated by the astronomical age of the star in question, e.g. a neutron star born in a supernova. The *braking index* n appears when Eq. (15) is rearranged to solve for $\dot{f}_{\text{rot}} \propto f_{\text{rot}}^n$. From theory, we expect $n = 5$ when energy is lost purely through gravitational wave emission from a mass quadrupole [Eq. (T1.3)] and $n = 3$ when energy is lost solely through electromagnetic radiation. (In practice, values of n measured for known pulsars vary widely, as discussed in [40–43].)

Substituting Eq. (21), (22) into Eqs. (16)–(19) gives fiducial equations in terms of τ and n for h_0, h_p :

$$h_0 \leq 10^{-25} \left(\frac{1 \text{ kpc}}{D} \right) \left(\frac{516 \text{ kyr}}{\tau} \right)^{\frac{1}{2}} \times \left(\frac{4}{n-1} \right)^{\frac{1}{2}} \left(\frac{I_{zz}}{10^{38} \text{ kg m}^2} \right)^{\frac{1}{2}}, \quad (23)$$

$$h_p \leq 10^{-25} \left(\frac{1 \text{ kpc}}{D} \right) \left(\frac{516 \text{ kyr}}{\tau} \right)^{\frac{1}{2}} \times \left(\frac{4}{n-1} \right)^{\frac{1}{2}} \left(\frac{1}{\Theta} \right)^{\frac{1}{2}} \left(\frac{I_{zz}}{10^{38} \text{ kg m}^2} \right)^{\frac{1}{2}}; \quad (24)$$

and for ϵ, ϵ_p :

$$\epsilon \leq 1.05 \times 10^{-6} \left(\frac{300 \text{ Hz}}{f} \right)^2 \left(\frac{516 \text{ kyr}}{\tau} \right)^{\frac{1}{2}} \times \left(\frac{10^{38} \text{ kg m}^2}{I_{zz}} \right)^{\frac{1}{2}} \left(\frac{4}{n-1} \right)^{\frac{1}{2}}, \quad (25)$$

$$\epsilon_p \leq 1.05 \times 10^{-6} \left(\frac{150 \text{ Hz}}{f_{\text{rot}}} \right)^2 \left(\frac{516 \text{ kyr}}{\tau} \right)^{\frac{1}{2}} \times \left(\frac{10^{38} \text{ kg m}^2}{I_{zz}} \right)^{\frac{1}{2}} \left(\frac{4}{n-1} \right)^{\frac{1}{2}} \left(\frac{1}{\Theta} \right)^{\frac{1}{2}}. \quad (26)$$

2.1.2. Free precession

Free precession of a biaxial neutron star occurs when the star's moment of inertia changes with time, which (assuming conservation of angular momentum) causes its angular velocity to also change with time. With reference to Fig. 1, while the angular momentum vector remains aligned with the Z axis, the angular velocity vector does not, and moreover exhibits a superimposed rotation about the star's axis of symmetry (the z axis). The general effect of this rotation on the CW waveform [23, 33, 44–46] is the addition of the (generally small) precession frequency to the CW harmonic frequencies f_{rot} and f . The precessional rotation does not modify the mass quadrupole, and hence does not appear in the harmonic amplitudes (Table 1).

2.1.3. r -mode oscillations

Neutron stars may exhibit various perturbations from their equilibrium shape. The energy dissipated as the perturbation decays is described by the quasi-normal modes of the star [47]. r -mode oscillations are one of a family of quasi-normal modes, which exist only when the star is rotating, as it is the Coriolis force acting to restore the star to its equilibrium shape.

Long-lived CW emission may be driven by r -modes [24, 48] through the Chandrasekhar-Friedman-Schutz instability [49, 50], as follows (cf. [51]). An oscillation may propagate either in the same direction as the rotation of the star, or in the opposite direction. An oscillation propagating counter to the rotation of the star, but with a slower absolute angular frequency, will still appear to be co-rotating to a inertial observer. Because the mode rotates counter to the star, it contributes *negatively* to the star's angular momentum in the co-rotating frame. On the other hand, because the mode co-rotates with the star to a inertial observer, it contributes *positively* to the star's angular momentum in the inertial frame, and will hence radiate gravitational wave with *positive* angular momentum. The *negative* angular momentum of a mode which loses *positive* angular momentum in gravitational waves therefore become *more* negative over time, resulting in a positive feedback loop which promotes the growth of the mode over time. Eventually, in real stars, the mode is expected to saturate due to viscous or other effects, which have been extensively studied in [52–63].

Some important differences distinguish CW emission from r -modes (bottom panel, Table 1) and from a rigidly rotating star. CW emission from r -modes is predominately through a time-varying current quadrupole, as opposed to a mass quadrupole; this leads to a different basis for the wave frame $(\tilde{x}, \tilde{y}, \tilde{z})$ (Fig. 1) than for a rigidly rotating star. Data analysis algorithms designed for the model of Fig. 1 are still applicable, however, with a simple reinterpretation of the polarisation angle ψ [64, Eq. (18)]. In addition, the gravitational wave luminosity [Eq. (T1.12)] of a current quadrupole scales more steeply with frequency, leading to a characteristic braking index of $n = 7$ instead of 5. Finally, the gravitational wave frequency is approximately $f_\alpha \approx 4f_{\text{rot}}/3$, with corrections depending on the nuclear equation of state of the neutron star [65, 66].

Fiducial equations relevant to r -mode emission are given for: the CW amplitude⁴

$$h_\alpha = 10^{-25} \left(\frac{1 \text{ kpc}}{D} \right) \left(\frac{\alpha}{3.44 \times 10^{-4}} \right) \times \left(\frac{\tilde{J}}{1.64 \times 10^{-2}} \right) \left(\frac{M}{1.4 M_\odot} \right) \left(\frac{f_\alpha}{200 \text{ Hz}} \right)^3 \times \left(\frac{R}{11.7 \text{ km}} \right)^3; \quad (27)$$

a dimensionless amplitude α which sets the magnitude of the r -mode velocity perturbation field,

$$\alpha = 3.44 \times 10^{-4} \left(\frac{200 \text{ Hz}}{f_\alpha} \right)^3 \left(\frac{11.7 \text{ km}}{R} \right)^3 \times \left(\frac{1.64 \times 10^{-2}}{\tilde{J}} \right) \left(\frac{1.4 M_\odot}{M} \right) \times \left(\frac{D}{1 \text{ kpc}} \right) \left(\frac{h_\alpha}{10^{-25}} \right); \quad (28)$$

and the gravitational wave luminosity

$$\dot{E}_{\text{GW}} = 6.07 \times 10^{29} \left(\frac{\alpha}{3.44 \times 10^{-4}} \right)^2 \left(\frac{\tilde{J}}{1.64 \times 10^{-2}} \right)^2 \times \left(\frac{M}{1.4 M_\odot} \right)^2 \left(\frac{R}{11.7 \text{ km}} \right)^6 \left(\frac{f_\alpha}{200 \text{ Hz}} \right)^8 \text{ W}. \quad (29)$$

In these equations, M and R are the mass and radius of the neutron star, and \tilde{J} is determined by the neutron star equation of state [64]. Further expressions give h_α, α in

⁴The CW amplitude for r -mode emission is generally labelled h_0 in the literature; in this review I use h_α for clarity.

terms of the spindown $\dot{f}_\alpha = 4\dot{f}_{\text{rot}}/3$:

$$h_\alpha \leq 10^{-25} \left(\frac{1 \text{ kpc}}{D} \right) \left(\frac{200 \text{ Hz}}{f_\alpha} \right)^{\frac{1}{2}} \times \left(\frac{\dot{f}_\alpha}{-1.37 \times 10^{-12} \text{ Hz s}^{-1}} \right)^{\frac{1}{2}} \left(\frac{I_{zz}}{10^{38} \text{ kg m}^2} \right)^{\frac{1}{2}}, \quad (30)$$

$$\alpha \leq 3.44 \times 10^{-4} \left(\frac{200 \text{ Hz}}{f_\alpha} \right)^{\frac{7}{2}} \left(\frac{11.7 \text{ km}}{R} \right)^3 \times \left(\frac{1.64 \times 10^{-2}}{\tilde{J}} \right) \left(\frac{1.4 M_\odot}{M} \right) \times \left(\frac{\dot{f}_\alpha}{-1.37 \times 10^{-12} \text{ Hz s}^{-1}} \right)^{\frac{1}{2}} \left(\frac{I_{zz}}{10^{38} \text{ kg m}^2} \right)^{\frac{1}{2}}; \quad (31)$$

and in terms of braking index $n = 7$ and characteristic age $\tau = (f_\alpha / -\dot{f}_\alpha) / (n - 1)$:

$$h_\alpha \leq 10^{-25} \left(\frac{1 \text{ kpc}}{D} \right) \left(\frac{773 \text{ kyr}}{\tau} \right)^{\frac{1}{2}} \times \left(\frac{6}{n-1} \right)^{\frac{1}{2}} \left(\frac{I_{zz}}{10^{38} \text{ kg m}^2} \right)^{\frac{1}{2}}, \quad (32)$$

$$\alpha \leq 3.44 \times 10^{-4} \left(\frac{200 \text{ Hz}}{f_\alpha} \right)^3 \left(\frac{11.7 \text{ km}}{R} \right)^3 \times \left(\frac{1.64 \times 10^{-2}}{\tilde{J}} \right) \left(\frac{1.4 M_\odot}{M} \right) \left(\frac{773 \text{ kyr}}{\tau} \right)^{\frac{1}{2}} \times \left(\frac{6}{n-1} \right)^{\frac{1}{2}} \left(\frac{I_{zz}}{10^{38} \text{ kg m}^2} \right)^{\frac{1}{2}}. \quad (33)$$

2.1.4. Accretion from a binary companion

If a neutron star is in orbit about a companion star, it may accrete matter from its companion at certain times during the lifetime of the binary system. This behaviour is observed e.g. in low-mass X-ray binaries. The accretion of matter transfers angular momentum to the neutron star, causing it to spin faster [67]. If, however, the accreted matter builds a non-axisymmetric deformation – a “mountain” – on the neutron star, it will radiate rotational energy as gravitational waves and spin down again [36, 68–74]. If these two processes are in balance with each other, the neutron star will maintain a near-constant spin frequency. This *torque balance* equilibrium has been proposed to explain the observed narrow distribution of the rotation periods of millisecond pulsars [75–82].

CW emission from a mountain on an accreting neutron star is generally assumed to follow the triaxial aligned model (Sec. 2.1.1). By equating the rotational kinetic energy gained through accretion to the energy lost through CW emission, the torque balance equilibrium implies an upper limit on h_0 , analogous to the spindown upper limit. Following [83], fiducial equations for the torque balance

upper limit on h_0, ϵ are

$$h_0 \leq 10^{-25} \left(\frac{300 \text{ Hz}}{f} \right)^{\frac{1}{2}} \left(\frac{1.4 M_\odot}{M} \right)^{\frac{1}{4}} \left(\frac{r_m}{11.7 \text{ km}} \right)^{\frac{1}{4}} \times \left(\frac{R}{11.7 \text{ km}} \right)^{\frac{1}{2}} \left(\frac{F_X/X}{1.3 \times 10^{-6} \text{ erg cm}^{-2} \text{ s}^{-1}} \right)^{\frac{1}{2}}, \quad (34)$$

$$\epsilon \leq 1.05 \times 10^{-6} \left(\frac{300 \text{ Hz}}{f} \right)^{\frac{5}{2}} \left(\frac{10^{38} \text{ kg m}^2}{I_{zz}} \right) \times \left(\frac{1.4 M_\odot}{M} \right)^{\frac{1}{4}} \left(\frac{r_m}{11.7 \text{ km}} \right)^{\frac{1}{4}} \left(\frac{R}{11.7 \text{ km}} \right)^{\frac{1}{2}} \times \left(\frac{F_X/X}{1.3 \times 10^{-6} \text{ erg cm}^{-2} \text{ s}^{-1}} \right)^{\frac{1}{2}} \left(\frac{D}{1 \text{ kpc}} \right). \quad (35)$$

Here r_m is the radius at which the spin-up torque due to accretion is applied to the neutron star, X is the fraction of the maximum accretion luminosity which is radiated away as X-rays, and F_X is the observed X-ray flux.

2.2. Phase parameters

The phase of a CW signal is the function $\phi_{\text{rot}}(t)$ that appears in Eqs. (4) and (5). Given the common assumption of a triaxial aligned star (Sec. 2.1), where CW emission is at the f harmonic only, the phase is most commonly written as $\phi(t) = 2\phi_{\text{rot}}(t)$. The instantaneous frequency (of the f harmonic) of the CW signal $f(t)$ is

$$f(t) = \frac{1}{2\pi} \frac{d\phi(t)}{dt}. \quad (36)$$

Determining the CW signal phase involves considering time standards at three locations: at the neutron star (Sec. 2.2.1), at the Solar System barycentre (SSB; Sec. 2.2.2), and at the detector (Sec. 2.2.3).

2.2.1. Time at the neutron star

At the neutron star, where time is measured by t_{NS} , the CW signal frequency $f(t_{\text{NS}})$ is generally modelled as a Taylor series, truncated to terms of order $t_{\text{NS}}^{s_{\text{max}}}$:

$$f(t_{\text{NS}}) = \sum_{s=0}^{s_{\text{max}}} f^{(s)} \frac{t_{\text{NS}}^s}{s!} = f + \dot{f} t_{\text{NS}} + \frac{1}{2} \ddot{f} t_{\text{NS}}^2 + \dots \quad (37)$$

Note that the *instantaneous* frequency $f(t_{\text{NS}})$ is distinct from the frequency *parameter* $f \equiv f(t_{\text{NS}} = 0)$. It is common to write $\dot{f} \equiv f^{(1)}$, $\ddot{f} \equiv f^{(2)}$, etc.

The $f^{(s)}$ coefficients represent the intrinsic frequency evolution of the star, e.g. as it spins down due to energy lost through CW emission. The CW phase at the neutron star is then given by

$$\phi(t_{\text{NS}}) = 2\pi \int dt_{\text{NS}} f(t_{\text{NS}}) = 2\pi \sum_{s=0}^{s_{\text{max}}} f^{(s)} \frac{t_{\text{NS}}^{s+1}}{(s+1)!}. \quad (38)$$

Note that Eq. (38) does not include the initial phase ϕ_0 , which (counter-intuitively) is considered an *amplitude* parameter; see Sec. 2.1, and also Sec. 3, Eq. (54).

2.2.2. Time at the Solar System barycentre

The reference frame associated with the SSB takes the standard celestial sphere reference frame but centres it at the SSB (Fig. 1). The unit vector \hat{n} points from the SSB to the neutron star, or to the binary barycentre (BB) if a binary companion is present, and defines the sky position of the source. It may be written in terms of the source's right ascension α and declination δ :

$$\hat{n} = (\cos \alpha \cos \delta, \sin \alpha \cos \delta, \sin \delta). \quad (39)$$

At the SSB, where time is measured by t_{SSB} , we must account for the motion of the neutron star relative to the SSB; given a gravitational wavefront emitted by the neutron star at time t_{NS} , at which time t_{SSB} does the same wavefront arrive at the SSB? The relationship between the two timescales may be written as

$$t_{\text{SSB}} = \Delta_{\text{R}}(t_{\text{NS}}) + \Delta_{\text{D}}(t_{\text{NS}}) + \Delta_{\text{E}}(t_{\text{NS}}) + \Delta_{\text{S}}(t_{\text{NS}}). \quad (40)$$

The term $\Delta_{\text{R}}(t_{\text{NS}})$, also known as the Rømer delay, accounts for the changing distance the gravitational wave must travel due to the orbit of the neutron star in a binary system around the BB. The effect of the Rømer delay is to Doppler-shift the CW signal frequency as the neutron star moves first towards, and then away from the detector. For circular orbits [84, 85],

$$\Delta_{\text{R}}(t_{\text{NS}}) = a_p \sin \frac{2\pi(t_{\text{NS}} - t_{\text{asc}})}{P}. \quad (41)$$

Here $a_p = (a/c) \sin i$ is the semi-major axis of the orbit (in units of $1/c$) projected onto the line of sight by i , the inclination angle of the orbit; P is the orbital period; and t_{asc} the time at which the neutron star passes through the ascending node⁵ of the orbit. For eccentric orbits, see the expressions given in [85].

The term $\Delta_{\text{D}}(t_{\text{NS}})$ accounts for the distance from the SSB to the neutron star (or BB if a binary companion is present), as well as any relative motion of the neutron star (or BB) relative to the SSB. For a simple linear motion, where the neutron star (or BB) is initially at a distance D from the SSB and moves with velocity \vec{v}_{NS} , we have [23]

$$\Delta_{\text{D}}(t_{\text{NS}}) = \gamma_{\text{NS}} t_{\text{NS}} + \frac{1}{c} |D\hat{n} + \gamma_{\text{NS}} \vec{v}_{\text{NS}} t_{\text{NS}}|, \quad (42)$$

where $\gamma_{\text{NS}} = (1 - |\vec{v}_{\text{NS}}|/c)^{-1/2}$. If $|\vec{v}_{\text{NS}}|$ is small compared to c , $\gamma_{\text{NS}} \approx 1$ and

$$\Delta_{\text{D}}(t_{\text{NS}}) \approx t_{\text{NS}} + \frac{D}{c}, \quad (43)$$

⁵The ascending node is the point in the neutron star's orbit where it passes through the plane of the sky (which intersects the BB, perpendicular to \hat{n}), in the direction away from Earth; see Fig. 1.

i.e. the CW arrives at the the SSB a time D/c after it was emitted. Most CW searches assume that $|\vec{v}_{\text{NS}}|$ is small enough so that this approximation holds. The effect of radial motion ($\vec{v}_{\text{NS}} \parallel \hat{n}$) is additional Doppler motion of the signal; this effect may be accounted for by redefining the frequency parameters [Eq. (37)] as being observed at the SSB, instead of being intrinsic to the star [23]. As a consequence, for sufficiently large radial motion, the intrinsic spindown of the neutron star may be observed at the SSB as a *spinup*, i.e. $\dot{f} > 0$. To account for this possibility, many CW searches cover a small positive range of frequency derivatives [e.g. 86–88]. The robustness of CW searches to proper motion ($\vec{v}_{\text{NS}} \perp \hat{n}$) is studied in [89].

The terms $\Delta_{\text{E}}(t_{\text{NS}})$ and $\Delta_{\text{S}}(t_{\text{NS}})$ denote the Einstein and Shapiro delays, respectively, associated with the binary system [90]. The Einstein delay collects the effects of gravitational red-shift and time dilation due to motions of the binary stars; the Shapiro delay accounts for the delayed propagation of the gravitational wave through the curved space-time of the binary system. These effects are absent for *isolated* (i.e. single) neutron stars; for binary systems with circular orbits, $\Delta_{\text{E}}(t_{\text{NS}}) = 0$ [90], and $\Delta_{\text{S}}(t_{\text{NS}})$ is small enough to be negligible [84].

2.2.3. Time at the detector

Similar to Eq. (40), we can relate t_{SSB} to the time measured at the detector on Earth, t_{det} :

$$t_{\text{SSB}} = t_{\text{det}} + \Delta_{\text{R}\odot}(t_{\text{det}}) + \Delta_{\text{E}\odot}(t_{\text{det}}) - \Delta_{\text{S}\odot}(t_{\text{det}}). \quad (44)$$

Here the Solar System Rømer delay $\Delta_{\text{R}\odot}(t_{\text{det}})$ accounts for the propagation time of the gravitational wave from the SSB to the detector:

$$\Delta_{\text{R}\odot}(t_{\text{det}}) = \frac{\vec{r}(t_{\text{det}}) \cdot \hat{n}}{c}, \quad (45)$$

where $\vec{r}(t_{\text{det}})$ is the vector from the SSB to the detector, accounting for both the sidereal and orbital motion of the Earth (Fig. 1). The Solar System Einstein and Shapiro delays $\Delta_{\text{E}\odot}(t_{\text{det}})$ and $\Delta_{\text{S}\odot}(t_{\text{det}})$ quantify, respectively, the effect of gravitational red-shift and time dilation due to motions of the Earth and other Solar System bodies, and the delayed propagation of the gravitational wave through the curved space-time of the Sun [90–92].

2.2.4. Determining the phase

Given gravitational wave data is timestamped by t_{det} , we must use the equations in Secs. 2.2.1–2.2.3 to determine t_{NS} as a function of t_{det} . For negligible linear motion of the neutron star ($|\vec{v}_{\text{NS}}| \ll c$), and circular binary orbits, Eq. (40) simplifies to

$$t_{\text{SSB}} = t_0 + t_{\text{NS}} + \Delta_{\text{R}}(t_{\text{NS}}), \quad (46)$$

where the constant D/c has been absorbed into a reference time t_0 . Equating to Eq. (44) gives

$$t_{\text{NS}} + \Delta_{\text{R}}(t_{\text{NS}}) = t_{\text{det}} - t_0 + \Delta_{\text{R}\odot}(t_{\text{det}}) + \Delta_{\text{E}\odot}(t_{\text{det}}) - \Delta_{\text{S}\odot}(t_{\text{det}}). \quad (47)$$

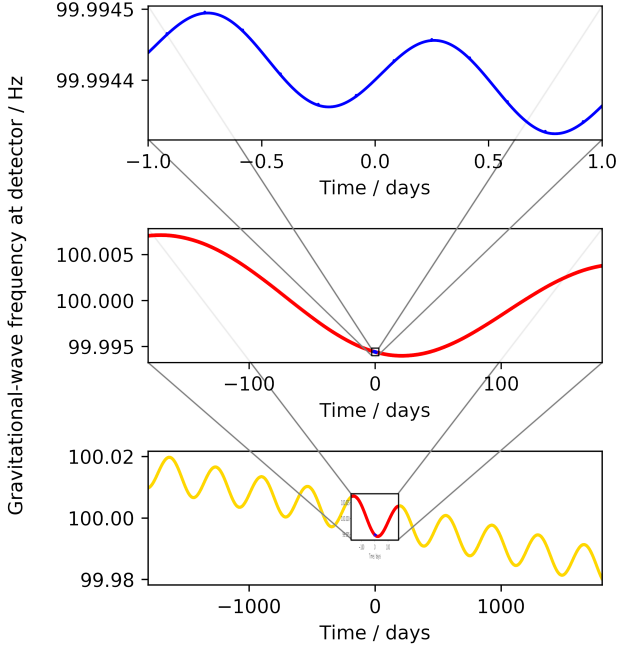


Figure 5: Typical modulations of the CW signal frequency for an isolated neutron star as a function of time. Top: daily modulation (blue) due to the rotation of the Earth. Middle: yearly modulation (red) due to the orbit of the Earth. Bottom: long-term decrease (yellow) due to the spindown of the star.

For isolated stars, $\Delta_{\text{R}}(t_{\text{NS}}) = 0$ and Eq. (47) gives t_{NS} directly in terms of functions of t_{det} ; otherwise, Eq. (47) must be numerically inverted to determine the function $t_{\text{NS}}(t_{\text{det}})$. Finally, the CW phase is

$$\phi(t_{\text{det}}) = 2\pi \sum_{s=0}^{s_{\text{max}}} f^{(s)} \frac{t_{\text{NS}}(t_{\text{det}})^{s+1}}{(s+1)!}. \quad (48)$$

Figure 5 illustrates the typical timescales of modulations for the CW phase of an isolated star. On timescales of a day, the dominant modulation is from Doppler modulation due to the Earth’s sidereal rotation. Over the course of a year, the dominant modulation is Doppler modulation due to the Earth’s orbit. And over many years of observation, we expect a steady spindown in frequency as the neutron star loses energy.

2.2.5. Approximate phase

While the full phase expression of Eq. (48) is required to accurately track the CW phase over long observation times, it is often useful (see e.g. Sec. 4.2) to consider a simpler, approximate form of the phase [23, 85, 93].

We first discard the Einstein and Shapiro delay terms $\Delta_{\text{E}\odot}(t_{\text{det}}), \Delta_{\text{S}\odot}(t_{\text{det}})$, as they are always small compared to the other terms in Eq. (47). We then expand Eq. (48), and discard any terms of order $f^{(s)} t_{\text{NS}}^{s-n+1} \Delta_{\text{R}\dots}^n$, where $n > 1$, and $\Delta_{\text{R}\dots}$ is any of the Rømer delay terms. This is because, over the time-span of an observation T , $f^{(s)}$ typically scales with T^{-s-1} , t_{NS}^{s-n+1} scales with T^{s-n+1} , but

the oscillatory Rømer terms remain of order unity. Terms of order $f^{(s)} t_{\text{NS}}^{s-n+1} \Delta_{\text{R}\dots}^n$, therefore, scale as T^{-n} , and are small enough to be neglected when $n > 1$. Finally, if $\Delta_{\text{R}}(t_{\text{NS}})$ is present, we assume that the orbital motion is slow compared to gravitational wave transit time across the orbit, and we can therefore approximate $\Delta_{\text{R}}(t_{\text{NS}}) \approx \Delta_{\text{R}}(t_{\text{det}})$. Applying these approximations yields:

$$\begin{aligned} \phi(t_{\text{det}}) &\approx 2\pi \sum_{s=0}^{s_{\text{max}}} f^{(s)} \left\{ \frac{(t_{\text{det}} - t_0)^{s+1}}{(s+1)!} \right. \\ &\quad \left. + \frac{(t_{\text{det}} - t_0)^s}{s!} \left[\Delta_{\text{R}\odot}(t_{\text{det}}) - \Delta_{\text{R}}(t_{\text{det}}) \right] \right\} \\ &= 2\pi f(t_{\text{det}} - t_0) \left[\Delta_{\text{R}\odot}(t_{\text{det}}) - \Delta_{\text{R}}(t_{\text{det}}) \right] \\ &\quad + 2\pi \left[f t_{\text{det}} + \frac{1}{2} \dot{f} t_{\text{det}}^2 + \frac{1}{6} \ddot{f} t_{\text{det}}^3 + \dots \right]. \end{aligned} \quad (49)$$

In Eq. (50), the instantaneous frequency $f(t_{\text{det}} - t_0)$ is usually replaced by a constant f_{max} , the maximum frequency of the signal over the observation, thereby giving the maximum modulation from the Rømer terms.

3. Challenges of continuous wave searches

The fundamental challenge of CW searches lies in extracting a very weak signal from comparatively noisy data. While gravitational wave signals from the mergers of binary black holes and neutron star are strong enough to, on occasion, be discernible to the naked eye [e.g. 7, 94], CW signals are comparatively much weaker. We must therefore apply data analysis techniques to the data. All such techniques rely on the idea of *matched filtering*: we formulate a model for the CW signal (Sec. 2), apply that model to the data, and compute a *detection statistic* which tells us which of two hypotheses are favoured: the *signal hypothesis*, that the data contains a CW signal matching our model; or the *noise hypothesis*, that it does not.

A first challenge is breaking the following circular dependency: how we can detect an unknown CW signal, when we must first know its model parameters, in order to apply the model to the data, in order to detect the signal in the first place? It is here that the distinction between *amplitude* and *phase* parameters made in Sec. 2 becomes important. To see why, we first express the detector response functions $F_+(t), F_\times(t)$ using two new functions⁶, $a(t)$ and $b(t)$ [23]:

$$\begin{aligned} F_+(t) &= a(t) \cos 2\psi + b(t) \sin 2\psi, \\ F_\times(t) &= b(t) \cos 2\psi - a(t) \sin 2\psi. \end{aligned} \quad (51)$$

By combining Eqs. (1), (4), (5) and (51), we see that the component $h^{2m}(t)$ of $h(t)$ associated with each harmonic

⁶Note that, in contrast to the definitions given in [23], I have absorbed the factor of $\sin \zeta$ into the definitions $a(t), b(t)$.

(f_{rot} , and f) may be written as the linear product of four amplitudes \mathcal{A}_i^{2m} and four basis functions $h_i^{2m}(t)$ [23]:

$$h(t) = \sum_{m=1}^2 h^{2m}(t) = \sum_{m=1}^2 \sum_{i=1}^4 \mathcal{A}_i^{2m} h_i^{2m}(t). \quad (52)$$

The basis functions are:

$$\begin{aligned} h_1^{2m}(t) &= a(t) \cos m\phi_{\text{rot}}(t), & h_2^{2m}(t) &= b(t) \cos m\phi_{\text{rot}}(t), \\ h_3^{2m}(t) &= a(t) \sin m\phi_{\text{rot}}(t), & h_4^{2m}(t) &= b(t) \sin m\phi_{\text{rot}}(t). \end{aligned} \quad (53)$$

The amplitudes are:

$$\begin{aligned} \mathcal{A}_1^{2m} &= A_+^{2m} \cos \Phi_{2m}^C \cos 2\psi - A_\times^{2m} \sin \Phi_{2m}^C \sin 2\psi, \\ \mathcal{A}_2^{2m} &= A_+^{2m} \cos \Phi_{2m}^C \sin 2\psi + A_\times^{2m} \sin \Phi_{2m}^C \cos 2\psi, \\ \mathcal{A}_3^{2m} &= -A_+^{2m} \sin \Phi_{2m}^C \cos 2\psi - A_\times^{2m} \cos \Phi_{2m}^C \sin 2\psi, \\ \mathcal{A}_4^{2m} &= -A_+^{2m} \sin \Phi_{2m}^C \sin 2\psi + A_\times^{2m} \cos \Phi_{2m}^C \cos 2\psi, \end{aligned} \quad (54)$$

where

$$\begin{aligned} A_+^{22} &= -C_{22}(1 + \cos^2 \iota), & A_+^{21} &= -\frac{1}{2}C_{21} \sin \iota \cos \iota, \\ A_\times^{22} &= -2C_{22} \cos \iota, & A_\times^{21} &= -\frac{1}{2}C_{21} \sin \iota. \end{aligned} \quad (55)$$

The \mathcal{A}_i^{2m} are functions of the four model parameters introduced in Sec. 2.1: the CW amplitude C_{2m} and phase Φ_{2m}^C , inclination angle ι , and polarisation angle ψ . Because $h(t)$ is *linear* in the \mathcal{A}_i^{2m} , we conjecture that we can *analytically* determine best-fit values for the amplitudes, without having to know them *a priori*.

When only one harmonic is present, the four amplitudes may indeed be found analytically, by choosing the values which maximise the *likelihood function*. This function gives the probability of the observed data, given a choice of CW signal model; it is generally computed by subtracting the CW model waveform from the data, and then computing the probability that what remains is pure noise following an assumed distribution (e.g. a Gaussian). The matched filter computed using the maximum likelihood estimators of the four amplitudes is known as the \mathcal{F} -statistic [23] (see also Sec. 7.1.3). In terms of detection power – the ability of a statistic to correctly pick the signal and/or noise hypotheses where appropriate – the maximum likelihood approach of the \mathcal{F} -statistic compares favourably to the theoretically more powerful approach of Bayesian marginalisation [95, 96]. When both harmonics are present, we may apply the \mathcal{F} -statistic to each harmonic individually [23], although this ignores degeneracies between the \mathcal{A}_i^{2m} , e.g. the common dependence on ι and ψ [29–31].

While we are fortunate in that we can find best-fit values for the *amplitude* parameters (via the \mathcal{A}_i^{2m}) without prior knowledge, we are out of luck when it comes to the *phase* parameters (Sec. 2.2): the neutron star’s intrinsic frequency f and spindowns \dot{f}, \ddot{f} , etc.; its position on the sky α, δ ; and, if relevant, its velocity \vec{v}_{NS} and binary

(circular) orbital parameters a_p, P, t_{asc} . Given the nonlinear dependence of $h(t)$ on these parameters, there is little prospect of analytically finding their best-fit values. We must therefore resort to numerical methods, as follows.

A CW *search* is, in essence, a process of numerical maximisation over the phase parameters. We pick values for the phase parameters, apply the CW signal model given by those parameters to the data, and compute a detection statistic e.g. the \mathcal{F} -statistic. We continue to pick sets of phase parameter values until, by trial and error, we find a combination where the detection statistic strongly favours the signal hypothesis. While this process sounds straightforward enough, in reality we must now confront several further challenges:

1. What values for the phase parameters should we pick? In other words, what is the *parameter space* – the subset of the space spanned by the phase parameters – from which we should sample vectors of phase parameter values? What motivates the choice of a particular parameter space? For example, should we search for CW signals at low f_{rot} , where most of the known pulsars reside [97]; or at high f_{rot} , where the gravitational wave amplitude $\propto f_{\text{rot}}^2$ is largest?
2. How many phase parameter vectors should we sample? We assume that, given the parameter space we have selected, at least one vector within that space will yield a model that fits any signal present in the data very well – otherwise the model is at fault – but we do not know the best-fit vector *a priori*. Moreover, the probability of us picking the *exact* best-fit vector is vanishingly small. But can we assume that we will eventually, given enough trials, pick a vector which is “close enough” to the best-fit vector, such that the detection statistic will still favour the signal hypothesis? If so, how do we quantify what we mean by “close enough”? And how many vectors do we need to sample in order to guarantee that we’ll eventually pick one “close enough” to the best-fit vector?
3. Suppose we know how many phase parameter vectors to sample from the parameter space. Is it realistic to compute a detection statistic for every vector? Each computation must take a finite amount of time. Given that CW signals are weak, we expect that we will need to analyse as much available data as possible in order to accumulate signal power versus noise. Can we compute all the required detection statistics in a finite amount of time, using currently-available computer technology? If not, does there exist a *sub-optimal* detection statistic which is either computationally cheaper to compute, or required the computation of few values (i.e. allows us to relax what we require as “close enough” to the best-fit vector)? Will this sub-optimal statistic still allow us to make a detection?
4. Suppose that we can compute (possibly sub-optimal)

detection statistics for all the phase parameter vector we are required to sample (in order to guarantee that at least one is “close enough” to the best-fit vector). Since we have computed multiple detection statistics, we are no longer considering a binary choice of *one* signal hypothesis versus one noise hypothesis; instead we must weigh *multiple* signal hypothesis, one for each detection statistic. How do we determine whether any of the signal hypotheses are favoured strongly enough to claim a detection? We might choose e.g. to set a *threshold* value on the detection statistics, and only consider detection statistics above the threshold as signifying a detection. We must then contend with the law of large numbers, however: as the number of detection statistics increases, eventually one is guaranteed to pass the threshold, even if there is no signal present in the data. How can we make decisions using the detection statistics, e.g. by setting a threshold, while avoiding (with high confidence) the possibilities of falsely claiming a detection, or of falsely rejecting one?

4. Continuous wave search performance measures

One of the challenges of CW searches, as outlined in Sec. 3, is deciding on the parameter space of signals to cover, and the detection statistic to compute. As we will see in Sec. 6, these aspects of CW search design must typically be balanced against each other. Due to limited computational resources, we must typically either choose a sensitive (but computationally expensive) detection statistic over a limited (but computationally cheaper) parameter space; or a wide (but expensive) parameter space and a sub-optimal (but cheaper) detection statistic.

In Sec. 6, I examine the performance of CW searches through the lens of this trade-off. I quantify searches according to the following metrics: sensitivity *depth* (Sec. 4.1), and parameter-space *breadth* (Sec. 4.2).

4.1. Sensitivity depth

The CW search sensitivity depth [98, 99] is a signal-to-noise ratio. As a measure of signal strength, an *upper limit at confidence C* is computed on the gravitational wave amplitude of the signal, typically h_0 . The upper limit h_0^C is computed using a variety of methods [99–101], which generally follow this procedure:

1. Decide on a criterion for detecting CW signals using a given search algorithm. Common practise is to take the maximum detection statistic X^{\max} found by a search as indicating the most promising detection candidate. Then, apply the algorithm to many synthesised data sets containing only noise, take the X^{\max} found from each data set, and set a threshold X^* such that only a fraction A of the X^{\max} satisfy $X^{\max} > X^*$. Here A is the *false alarm probability*:

the probability that we would falsely claim a detection by finding a $X^{\max} > X^*$, despite the data containing no signal. It is typically small; conventionally CW searches establish a $A = 1\%$ false alarm threshold. (Note that this threshold is established using the maximum of many detection statistics computed by the search; the probability of a *single* detection statistic exceeding the threshold is therefore $\ll A$.)

2. Given a fixed h_0 , draw random sets of values for the CW signal model parameters. Amplitude parameters (other than h_0) are drawn from their natural priors; phase parameters are drawn from the search parameter space.
3. For each set of model parameter values, synthesise a CW signal time series $h(t)$ in software using the given parameter values. Add to each $h(t)$ a realistic representation of the detector noise, either by using real detector data, or by synthesising stationary Gaussian noise with power spectral density S_h (which may be assumed constant over the narrow bandwidth of CW signals).
4. Analyse each noisy $h(t)$ time series using the CW search algorithm in question. For each noisy $h(t)$, decide whether the synthesised CW signal would have been detected using the criteria established previously, i.e. is the X^{\max} found from the search of each noisy $h(t)$ greater than X^* ? The fraction of CW signals considered detected is the *detection confidence C*. (The quantity $1 - C$ is the *false dismissal probability*: the probability that we would dismiss claiming a detection because $X^{\max} < X^*$, despite the data containing a signal.) The h_0 fixed in step 2 is then interpreted as an upper limit h_0^C with C confidence; if the data contains a signal with amplitude h_0 , we would have confidence C of detecting it.
5. Adjust h_0 and repeat steps 2–4 above until C converges to the desired confidence; typical choices are 90% or 95%. Given that CW signals have yet to be detected, published CW searches typically quote upper limits h_0^C as a function of search frequency f as their primary scientific result.

The sensitivity depth takes the ratio of an upper limit, given by h_0^C , to an estimate of the noise in the detector, given by S_h . It is defined as:⁷

$$\mathcal{D} = \frac{\sqrt{S_h}/\text{Hz}}{h_0^C}. \quad (56)$$

Note that S_h is defined as the *single*-sided power spectrum, over the same frequency band as the CW signals used to determine h_0^C , and taking the harmonic mean of the data over time (and over multiple detectors). Averaging over

⁷The depth is conventionally defined as $\sqrt{S_h}/h_0$ and therefore has the same units as $\sqrt{S_h}$, typically $\text{Hz}^{-1/2}$. In this review I explicitly normalise S_h by units of Hz, so that \mathcal{D} is a dimensionless quantity.

time gives a representative value of the detector power spectrum, whose value over short time periods may vary over the course of an observation. Non-Gaussian “glitches” in the noise of short ($\lesssim 1$ s) duration generally do not impact long-duration continuous wave searches, unless they are sufficiently short and loud (resembling a Dirac delta function) that their Fourier transform contaminates a wide frequency band [102, 103].

Since a smaller h_0^C implies a more sensitive search, \mathcal{D} increases with search sensitivity. By factoring out the performance of the detector, i.e. its noise power spectrum, \mathcal{D} quantifies the contribution of the CW search algorithm to the overall search sensitivity. Typically, \mathcal{D} is found to be approximately constant for a given CW search, provided we exclude frequency bands where S_h is degraded by excessive detector noise, e.g. instrumental line artefacts.

Sensitivity depth serves as a useful measure for qualitatively comparing the sensitivities achieved by different CW searches and algorithms. This comes with the following caveat, however: a strictly “apples-to-apples” comparison is difficult to achieve in practise, for the following reasons:

- When computing h_0^C , the criteria for considering a CW signal detected (step 1 of the upper limit procedure) often varies between searches. For example, a CW signal may be considered detected only after more sensitive follow-up studies of candidates found by the initial search. This makes it challenging to model the statistical properties of the detection criteria (as discussed in [99]) and thereby determine its false alarm probability A . It is generally assumed that A is both small and weakly dependent on the choice of detection criteria, e.g. X^* scales weakly with A and the number of computed detection statistics [101]. The overall A of a CW search is rarely quantified explicitly, however, which makes a strictly equitable comparison of search sensitivities at equal false alarm rates difficult to achieve.
- The population of signals sampled from in determining h_0^C (step 2 of the upper limit procedure) also varies. For example, searches using the PowerFlux algorithm (Sec. 7.2.4) traditionally fix the inclination angle ι , in addition to h_0 , and report two values of h_0^C for circular (most sensitive/best case) and linear (least sensitive/worst case) polarisations. Analytic scaling to convert upper limits of this type to so-called *population-averaged* upper limits (where $\cos \iota$ is sampled uniformly from $[-1, 1]$) were proposed in [101], while [104] suggests that such scaling must depend on the data being analysed.
- There are different approaches to determining the confidence C (steps 3–4 of the upper limit procedure). Searches using the PowerFlux algorithm determine an upper limit on h_0 on individual signals, rather than over a population of signals, using Feldman-Cousins confidence intervals; the largest

(worst case) upper limit found for an individual signal is then selected to represent the population as a whole (see discussion in [101]). Even when the population-averaged procedure is followed, various approaches are used to find h_0^C at the desired C , usually motivated to reduce computational cost: e.g. linear or spline interpolation of h_0^C as a function of C . (A Bayesian approach, which fits a sigmoid curve to a Boolean array of detections as a function of h_0 , is proposed in [105].)

- The CW data analysis community has historically not converged to a consistent choice of confidence C at which to set upper limits (step 5 of the upper limit procedure), with both 90% and 95% being common choices. (Though perhaps a consensus is now emerging; of the 17 papers reviewed in Sec. 6 which analysed data from the LIGO-Virgo 3rd observing run, only one paper [106] set upper limits at 90% confidence, with the remainder choosing 95%.)
- Finally, choosing an appropriate value for S_h is not entirely straightforward [99]. Unless we have performed the analysis ourselves, we are unlikely to have access to the original data set used in the analysis, and it may be impractical to reconstruct the original data set without access to the software and configuration details used in its preparation. We must therefore rely on generic sensitivity curves [107–113] which give representative S_h for each data set. In addition, computation of S_h over an appropriate frequency band can be sensitive to choices of windowing and/or averaging over frequency.

For these reasons, comparisons of the \mathcal{D} achieved by different CW searches or algorithms should not be taken too seriously beyond the first one or two significant figures.

4.2. Parameter-space breadth

To complement \mathcal{D} as a measure of CW search sensitivity, in this review I introduce the breadth \mathcal{B} as a measure of CW parameter-space coverage:

$$\mathcal{B} = \int_{\mathcal{P}} d\vec{p} \sqrt{g(\vec{p})}. \quad (57)$$

where \mathcal{P} represents that CW search parameter space, from which parameter vectors $\vec{p} \in \mathcal{P}$ are drawn. The function $g(\vec{p})$ is the determinant of the *parameter-space metric* $g_{ij}(\vec{p})$ [114, 115]. The metric $g_{ij}(\vec{p})$ provides a distance measure on the parameter space, as follows: suppose a CW signal is present in the data with best-fit parameters \vec{p} , and we attempt to match that signal to a model waveform with parameters $\vec{p} + \Delta\vec{p}$. The *mismatch* $\mu = g_{ij}(\vec{p}) \Delta p_i \Delta p_j$ measures how much signal power we expect to lose; if $\Delta\vec{p} = \vec{0}$, we have perfectly matched the signal and expect the detection statistic to be at its optimal maximum; for $\Delta\vec{p} \neq \vec{0}$ we expect the detection statistic to be reduced by a factor $\approx 1 - \mu$ for small μ [35, 93].

The metric gives a quantitative measure of how “close” (cf. Sec. 3) signals are to each other in parameter space, in the context of recovering signal power. Its determinant quantifies the “density” of parameter space: denser regions being where signals are “closer” to each other than in sparser regions. The breadth \mathcal{B} is therefore a measure of the number of CW model waveforms (or *templates*) needed to properly search a given parameter space. That said, I do not attempt to rescale \mathcal{B} to give actual template counts for a given CW search, as I consider that to be an implementation detail of the algorithm in question. Ideally, the algorithm would use the minimum number of templates needed to cover the parameter space, while guaranteeing that the mismatch remains under a pre-established maximum [116, 117].

It has been shown [35] that, for observing time-spans longer than a day, the CW parameter-space metric is largely independent of the amplitude parameters of the CW signal. We therefore require only the CW phase to compute the metric; indeed, it is sufficient to use the simplified, approximate phase given by Eq. (50) (Sec. 2.2.5). Using the *phase metric* approximation [35, 118], the metric is then computed from

$$g_{ij}(\vec{p}) = \frac{1}{T} \int_T dt \left. \frac{\partial \phi(t)}{\partial p_i} \frac{\partial \phi(t)}{\partial p_j} \right|_{\vec{p}} - \frac{1}{T^2} \left[\int_T dt \left. \frac{\partial \phi(t)}{\partial p_i} \right|_{\vec{p}} \right] \left[\int_T dt \left. \frac{\partial \phi(t)}{\partial p_j} \right|_{\vec{p}} \right], \quad (58)$$

where we integrate over the observation spanned by T .

In computing the parameter-space breadth, I will assume the parameter-space metric of a *fully-coherent* CW signal, i.e. one where $\phi(t_{\text{det}})$ is matched to the data across the entire observation. Not all detection statistics obey this criteria, however; indeed a common trade-off made by sub-optimal detection statistics is to relax this restriction. The purpose of \mathcal{B} , however, is to quantify the size of the parameter space of the CW signal model, whereas the size of the CW search (in terms of the number of templates it searches) is considered an implementation detail of the search. As discussed in Sec. 3, a CW data analyst must often decide whether to prioritise sensitivity or parameter-space coverage in their CW search design; a particular choice of trade-off is then reflected in the \mathcal{D} and \mathcal{B} achieved for that search. An optimal choice could be to choose a detection statistic which balances sensitivity (thereby increasing depth) with computational efficiency, allowing a wider parameter space to be searched (thereby increasing breadth).

In the following sections I give formulas for \mathcal{B} over the frequency and spindown (Sec. 4.2.1), sky (Sec. 4.2.2), and binary orbital parameter spaces (Sec. 4.2.3). I use Eq. (50) as a suitable approximation to the metric, with $f(t_{\text{det}} - t_0)$ set to f , so that \mathcal{B} is correct when integrated over frequency. This means, however, that the breadth of the sky and binary orbital parameter spaces scale with f , and therefore we must defer integration over f until the end.

I therefore define *raw breadths* B , which have *not* been integrated over f , in the following sections. These factors will be assembled to find the overall breadth \mathcal{B} in Sec. 4.2.4.

4.2.1. Frequency and spindown parameter space

The phase metric over the frequency and spindown parameters is [39, 119]

$$g_{f^{(r)}, f^{(s)}} = \frac{4\pi^2(r+1)(s+1)}{(r+2)!(s+2)!(r+s+3)!} T^{r+s+2}, \quad (59)$$

where $f^{(r)}$, $f^{(s)}$ are the r th, s th spindown parameters respectively. Note that $g_{f^{(r)}, f^{(s)}}$ is independent of the $f^{(s)}$. The square root of the determinants of this metric, up to the 2nd spindown, are

$$B_f = \sqrt{g(f)} = \frac{\pi T}{\sqrt{3}}, \quad (60)$$

$$\sqrt{g(f, \dot{f})} = \frac{\pi^2 T^3}{6\sqrt{15}}, \quad (61)$$

$$\sqrt{g(f, \dot{f}, \ddot{f})} = \frac{\pi^3 T^6}{360\sqrt{105}}, \quad (62)$$

Note that Eq. (59) assumes the observation runs over $t_{\text{det}} \in [0, T]$, while Eqs. (60)–(62) are independent of this choice. Equation (60) immediately gives the raw frequency breadth B_f . In order to separate out the contributions from each spindown parameter, I define their (raw) breadths as ratios to the breadth of the preceding spindown, as follows:

$$B_{\dot{f}} = \frac{1}{B_f} \int d\dot{f} \sqrt{g(f, \dot{f})} = \frac{\pi T^2}{6\sqrt{5}} \left| \dot{f} \right|, \quad (63)$$

$$B_{\ddot{f}} = \frac{1}{B_{\dot{f}}} \int d\ddot{f} \sqrt{g(f, \dot{f}, \ddot{f})} = \frac{\pi T^3}{60\sqrt{7}} \left| \ddot{f} \right|. \quad (64)$$

Here I adopt the notation of [85]: for a parameter p with parameter space $[p_0, p_1] \cup [p_2, p_3] \cup \dots$, define

$$\left| p^q \right| \equiv p_1^q - p_0^q + p_3^q - p_2^q + \dots \quad (65)$$

The breadths in $f^{(s)}$ [Eqs. (60), (63), (64)] scale as T^{s+1} , consistent with the typical spacings $\Delta f^{(s)} \propto T^{-s-1}$ used to construct a rectangular search grid in these parameters.

4.2.2. Sky parameter space

The metric over the sky arises from the Solar System Rømer delay $\Delta_{\text{R}\odot}(t_{\text{det}})$ [Eq. (45)]. I approximate the detector position vector $\vec{r}(t_{\text{det}})$ with a Ptolomaic-like orbit (cf. [119]), where the Earth’s orbit is circular and co-planar with its equator. I also ignore the relative phase differences between the Earth’s sidereal and orbital motions, which should be immaterial over observation times much greater than a day. With these assumptions the sky component of the CW phase simplifies to

$$\phi_{\text{sky}}(t_{\text{det}}) = 2\pi f \cos \delta \left[\tau_s \cos(\alpha - \Omega_s t_{\text{det}}) + \tau_o \cos(\alpha - \Omega_o t_{\text{det}}) \right], \quad (66)$$

where $\tau_s \approx 2.13 \times 10^{-2}$ lt-s is the radius of the Earth, $\tau_o \approx 4.99 \times 10^2$ lt-s is the orbital radius of the Earth around the Sun, and $\Omega_s \approx 7.27 \times 10^{-5}$ Hz, $\Omega_o \approx 1.99 \times 10^{-7}$ Hz are the respective sidereal and orbital angular frequencies. Combining Eqs. (57), (58), and (66), and noting that $\tau_s \ll \tau_o$ and $\Omega_o \ll \Omega_s$, we arrive at the following expression for

$$B_{\text{sky}} = \frac{8}{3} \pi^3 f^2 \tau_o^2 \left\{ 1 - \text{sinc}^2 \Omega_o T - 2 \text{sinc}^2 \frac{\Omega_o T}{2} + 2 \text{sinc}(\Omega_o T) \text{sinc}^2 \frac{\Omega_o T}{2} + \frac{4\tau_s}{\tau_o} \text{sinc} \frac{\Omega_s T}{2} + \mathcal{O} \left[\left(\frac{\tau_s}{\tau_o} \right)^2 \right] \right\}^{1/2}, \quad (67)$$

where $\text{sinc}(x) = \sin(x)/x$. Note that B_{sky} converges to $8\pi^3 f^2 \tau_o^2 / 3$ for $\Omega_o T \gg 1$, i.e. once the observation time spans many years. For CW searches which cover patches of the sky, I rescale B_{sky} by the fraction of the sky covered, thereby assuming that the template density is isotropic over the sky for long observations.

4.2.3. Binary orbital parameter space

The phase metric over the binary orbital parameters is derived in [85, 120]. In calculating the breadth, I use the ‘‘long-segment’’ approximation to the metric, where $T \gg P$, and thus assume that the CW signal is observed over many orbital periods. The metric is most conveniently parameterised by a_p , the angular frequency $\Omega_p = 2\pi/P$ of the orbit, and t_{asc} . It is given by Eq. (71) of [85], and the square root of its determinant is

$$\sqrt{g(a_p, \Omega_p, t_{\text{asc}})} = \sqrt{\frac{2}{3}} \pi^3 f^3 a_p^2 \Omega_p T. \quad (68)$$

When t_{asc} is known, the (raw) breadth B_{bin} is

$$B_{\text{bin}} = \int da_p \int d\Omega_p \int dt_{\text{asc}} \sqrt{g(a_p, \Omega_p, t_{\text{asc}})} = - \left(\frac{2}{3} \right)^{3/2} \pi^5 f^3 \left[a_p^3 \right] \left[P^{-2} \right] \left[t_{\text{asc}} \right] T, \quad (69)$$

where the bounds of the integral over Ω_p are expressed in terms of P for convenience.⁸ When t_{asc} is unknown, we must search over its full range $[0, P]$; the breadth is then

$$B_{\text{bin}} = \int da_p \int d\Omega_p \int_0^{2\pi/\Omega_p} dt_{\text{asc}} \sqrt{g(a_p, \Omega_p, t_{\text{asc}})} = -2 \left(\frac{2}{3} \right)^{3/2} \pi^5 f^3 \left[a_p^3 \right] \left[P^{-1} \right] T. \quad (70)$$

The TwoSpect algorithm (Sec. 7.2.6) conventionally searches over a fixed range of frequency modulation depth

⁸Note that the sign of $\left[P^{-2} \right]$, $\left[P^{-1} \right]$ is negative, hence the overall minus sign in Eqs. (69), (70) respectively.

$\Delta f_{\text{obs}} = f a_p \Omega_p$ instead of a fixed range of a_p . The appropriate formula for its breadth is found by substituting $a_p = \Delta f_{\text{obs}} / f \Omega_p$ in Eq. (68) and integrating over Δf_{obs} :

$$B_{\text{bin}} = \int d\Delta f_{\text{obs}} \int d\Omega_p \int_0^{2\pi/\Omega_p} dt_{\text{asc}} \sqrt{g(a_p, \Omega_p, t_{\text{asc}})} = \frac{1}{2} \left(\frac{2}{3} \right)^{3/2} \pi^3 f \left[\Delta f_{\text{obs}}^3 \right] \left[P \right] T. \quad (71)$$

4.2.4. Assembling the overall breadth

Given the raw breadths defined in Sec. 4.2.1–4.2.3, the overall breadth is then found by multiplying these factors and integrating over f :

$$\mathcal{B} = \int df \prod B_{\dots}, \quad (72)$$

where the product is taken over those B_{\dots} relevant to a particular search.

It is informative to divide \mathcal{B} into factors which arise from each component of the parameter space (frequency, spindown, sky, binary orbit), so that we can see the relative contribution of each component to the overall breadth. I define the factors of \mathcal{B} as follows. Let k be the exponent of f in each raw breadth B_{\dots} relevant for a search – except for B_f , where we set $k = 1$ to account for integration over f . Let κ be the sum over all k . When integrated over f , \mathcal{B} will contain a factor $K = \left[f^\kappa \right] / \kappa$. We now define

$$\mathcal{B}_f = B_f K^{1/\kappa}, \quad \mathcal{B}_{\dots} = \frac{B_{\dots}}{f^k} K^{k/\kappa}; \quad (73)$$

each \mathcal{B}_{\dots} weights B_{\dots} by its contribution to the integration over f . When multiplied together, these factors will give \mathcal{B} consistent with Eq. (72).

As an example, consider a CW search over the frequency, sky, and binary orbital parameters; we therefore require B_f [Eq. (60)], B_{sky} [Eq. (67)], and B_{bin} [either Eq. (69) or (70)]. The exponents of f that appears in B_{sky} and B_{bin} are $k = 2$, $k = 3$ respectively, and for B_f we set $k = 1$; hence $\kappa = 6$. The component breadths are therefore

$$\begin{aligned} \mathcal{B}_f &= B_f \left(\left[f^6 \right] / 6 \right)^{1/6}, \\ \mathcal{B}_{\text{sky}} &= \frac{B_{\text{sky}}}{f^2} \left(\left[f^6 \right] / 6 \right)^{2/6}, \\ \mathcal{B}_{\text{bin}} &= \frac{B_{\text{bin}}}{f^3} \left(\left[f^6 \right] / 6 \right)^{3/6}, \end{aligned} \quad (74)$$

and \mathcal{B} is given equivalently by

$$\mathcal{B} = \int df B_f B_{\text{sky}} B_{\text{bin}} = \mathcal{B}_f \mathcal{B}_{\text{sky}} \mathcal{B}_{\text{bin}}. \quad (75)$$

4.2.5. Hidden Markov models

The parameter-space breadth [Eq. (57)] is intended to be agnostic to the implementation details of a CW search, to enable a fair comparison of CW searches which cover

the same parameter space using different algorithms. One particular CW search algorithm, however, requires special consideration.

In place of the Taylor series representation of the CW signal frequency $f(t)$ [Eq. (37)], Hidden Markov models (HMMs) represent the frequency $f(t)$ as an unobserved (hidden) state variable over a time-frequency representation of $h(t)$, typically discretised into N frequency bins and M time steps. The Viterbi algorithm is then used to determine the most likely sequence of hidden states – i.e. the CW frequency as a function of time – based on a set of observables – a detection statistic computed for each frequency bin and time step.

A fuller description of the Viterbi algorithm is deferred until Sec. 7.2.7. For now, we note that the Viterbi algorithm is efficient at considering a *very* large number of possible CW frequency paths: $N\delta n^M$, where δn is the number of possible paths the CW frequency may take between successive time steps. Given that M is typically of order $10\text{--}10^4$, by this measure the parameter space covered by a CW search using the Viterbi algorithm may be *thousands* of orders of magnitude greater than a comparable search which models the CW frequency as a Taylor series. On the other hand, many of these paths represent small deviations – by a frequency bin here or there – from a CW frequency path that otherwise follows a Taylor series, and one might argue whether it is fair to count these deviations as completely different paths.

As a compromise, I account for the increased parameter space coverage of HMM searches using the Viterbi algorithm as follows. Suppose e.g. that the CW frequency is allowed to jump by ± 1 bins per time step; i.e. $\delta n = 3$. Given a frequency bin n at time step m , at the previous time step $m - 1$ the CW frequency may pass through 3 frequency bins $n - 1, n, n + 1$; at the next previous time step $m - 2$ the CW frequency may pass through 5 frequency bins $n - 2, n - 1, n, n + 1, n + 2$; and so on. In general, the parameter-space volume encompassing the possible CW frequency paths increases by $\delta n - 1$ between time steps. Calculating this volume over all M time steps and normalising by M defines the HMM breadth factor

$$\begin{aligned} \mathcal{B}_{\text{HMM}} &= \frac{1}{M} \sum_{m=0}^{M-1} 1 + m(\delta n - 1) \\ &= \frac{1}{2}(M\delta n - M - \delta n + 3). \end{aligned} \quad (76)$$

This definition is consistent with the spirit of the parameter-space breadth, in that it seeks to quantify the volume of the parameter space, while the placement of templates within that space is considered an implementation choice. Note that $\mathcal{B}_{\text{HMM}} = 1$ when either $M = 1$ or $\delta n = 1$, i.e. when the CW frequency follows a single path consistent with the Taylor series model.

Table 2: Data collection runs of the LIGO and Virgo gravitational wave detectors, 2002–2020. Columns are: detector generation, run label, start date, end date, time-span, and number of CW searches reviewed in Sec. 6 which used data from the run. (Some CW searches use data from more than one run, which is accounted for in column 6.)

Gen.	Obs.	Start	End	T days	CW #
0.5G	S1	23 Aug 2002	9 Sep 2002	17	2
0.5G	S2	14 Feb 2003	14 Apr 2003	59	4
0.5G	S3	31 Oct 2003	9 Jan 2004	70	1
0.5G	S4	22 Feb 2005	23 Mar 2005	29	5
1G	S5	4 Nov 2005	1 Oct 2007	696	14
1G	VSR1	18 May 2007	1 Oct 2007	136	1
1.5G	VSR2	7 Jul 2009	8 Jan 2010	185	9
1.5G	S6	7 Jul 2009	20 Oct 2010	470	22
1.5G	VSR3	11 Aug 2010	19 Oct 2010	69	2
1.5G	VSR4	3 Jun 2011	5 Sep 2011	94	6
2G	O1	12 Sep 2015	19 Jan 2016	129	57
2G	O2	30 Nov 2016	25 Aug 2017	268	79
2G	O3	1 Apr 2019	27 Mar 2020	361	116
	– a	1 Apr 2019	1 Oct 2019	183	
	– b	1 Nov 2019	27 Mar 2020	147	

5. A brief history of gravitational wave data

This section summarises the development of interferometric gravitational wave detectors, and the data collected by them, over the last two decades.

Kilometre-scale gravitational wave observatories have been in operation for nearly 20 years, and have completed 13 data collection runs to date (Table 2). The first few runs of the Initial LIGO [121] detectors – the 0.5 generation (0.5G) in Table 2 – were generally short (a few months or less) with their primary aim being to fully commission the instruments and gain experience in analysing their data. This effort culminated in the 1st generation (1G) of the Initial LIGO and Virgo [122] detectors at their inaugural design sensitivities. A period of further sensitivity improvements followed – the 1.5 generation (1.5G) Enhanced LIGO [123] and Virgo+ [124] detectors – before an extended shutdown period for significant upgrades, in order to achieve sensitivities capable of detecting binary black hole/neutron star mergers.

The commencement of the 1st observing run (O1) of Advanced LIGO [11] – and the first detection, the binary black hole merger GW 150914 [4] two days into the run – began the current era of 2nd-generation (2G) detectors and the beginning of gravitational wave astronomy. Advanced Virgo [12] joined the end of the 2nd observing run (O2), in time to detect the first binary neutron star merger GW 170817 [7]. LIGO and Virgo commenced joint observations with the 3rd observing run (O3).

KAGRA [125], the first kilometre-scale interferometer to use cryogenic cooling to reduce detector noise, first collected data in 2020, and has recently joined the 4th observing run (O4), currently underway, alongside LIGO and

Virgo. A third instrument of the LIGO Observatory is under construction in India [126].

Several sub-kilometre-scale detectors have also existed at various times; given their limited sensitivity to gravitational wave signals, their primary focus has been technology development. Of these detectors, GEO-600 [127, 128] has been in operation the longest at ≈ 16 years, and has opportunistically collected ≈ 10 years of data⁹ in case of a spectacular gravitational wave event.

6. Continuous wave searches, 2003–2022

In this section, I review searches for CW signals in the LIGO and Virgo data. I select searches for review that satisfy the following criteria:

1. Per the subject of this review, I review only searches for CWs from rapidly-spinning neutron stars. This excludes several recent searches [e.g. 129, 130] for beyond Standard Model particles such as ultra-light bosons and dark photons. These phenomena are expected to produce signals that follow the same CW signal morphology as for rapidly-spinning neutron stars, and are therefore amenable to the same CW search techniques.
2. I select only searches which generally assume the CW signal model described in Sec. 2. I have included searches which use an HMM to tracking a wandering CW signal frequency, but excluded searches which assume an unmodeled, stochastic signal [e.g. 131, 132].
3. Finally, I select only searches which set upper limits on h_0 or an equivalent amplitude, so that the sensitivity depth \mathcal{D} may be computed.

These criteria select 297 searches from 80 published articles. They include searches performed by the joint Continuous Wave Working Group of the LIGO Scientific Collaboration, Virgo Collaboration, and KAGRA Collaboration, as well as by other CW research groups.

The intention of this review is to show the development of the field of CW data analysis over time, and illustrate how the challenges outlined in Sec. 3 have been addressed. It does not attempt an “apples-to-apples” comparison between CW search designs or algorithms, i.e. comparing one choice of search design or algorithm against another, while keeping all other choices the same. As the field has developed, CW analysts will have faced constraints on resources – e.g. time, people power, computing power – and made practical choices of search design and algorithm within those constraints. Controlling for those choices equitably is impractical. As discussed in Sec. 4.1, the various differences in determine h_0^C upper limits does not easily allow a precise comparison of sensitivities. Comparing

searches simply by breadth assumes that there is a uniform probability of CW detection per unit parameter space, and therefore broader searches should rank higher. In fact, there are good reasons to target more limited parameter spaces based on promising astrophysically-motivated priors for CW detection.

Figure 6 plots, for the selected CW searches, their sensitivity depths \mathcal{D} against their parameter-space breadths \mathcal{B} . (The raw data for this plot is provided in Table A.3.) The searches are divided in seven categories, commonly used in the literature, based on their astronomical targets:

1. Targeted searches for known pulsars (“Pulsars T” in Fig. 6). These searches¹⁰ assume that the CW signal is phase-locked to the electromagnetic emission from the pulsar, and so that $\phi_{\text{rot}}(t)$ is given by the pulsar’s electromagnetic ephemeris. The phase parameter space is therefore a single point. Canonical targets are the Crab and Vela pulsars, and PSR J0537–6910 [106, 133–135].
2. Narrow-band searches for known pulsars (“Pulsars NB” in Fig. 6). These searches also target known pulsars, but relax the assumption that the electromagnetic and CW phases are phase-locked, and allow f_{rot} , \dot{f}_{rot} , etc. to deviate from their electromagnetically-measured values by a small fraction [136]. Narrow-band searches cover small parameter spaces in the frequency and spindown parameters.
3. Directed searches for central compact objects (CCOs), suspected to be young neutron stars born in core-collapse supernovae. These searches typically require only a single point in the sky parameter space: some CCOs are observed as bright, well-localised X-ray emission from the centre of the remnant, and in any case the size of the remnant can usually be considered small compared to the sky parameter resolution. CCOs are not, however, observed as pulsars, and their rotational frequency evolution is therefore unknown. The searches must therefore cover broad ranges of frequency and (1st, sometimes 2nd) spindowns. The most promising CCOs for CW detection – based on their likely ages (young) and distances (close), and the likelihood that the CCO is a neutron star – are in the supernova remnants Cassiopeia A (Cas A) and Vela Jr. [87, 137]
4. Directed searches for low-mass X-ray binaries (LMXBs). Here, the accretion of matter onto the neutron star from a binary companion may build up an observable

⁹See https://gwosc.org/timeline/show/history/G1_SCI/770000000/501462418/

¹⁰In this review I count a survey of known pulsars from a particular paper and analysis pipeline as one “search”, and define its breadth as equal to the number of upper limits it outputs. (I do not count upper limits which assume restricted priors on ι and/or ψ based on electromagnetic observations.) For example, the most recent known pulsar survey [133] used three analysis pipelines, which are counted as separate searches. The Bayesian analysis pipeline (Sec. 7.1.4) produced 470 upper limits from 236 pulsars at 2 harmonics (with 2 upper limits excluded), and hence has a breadth of 470.

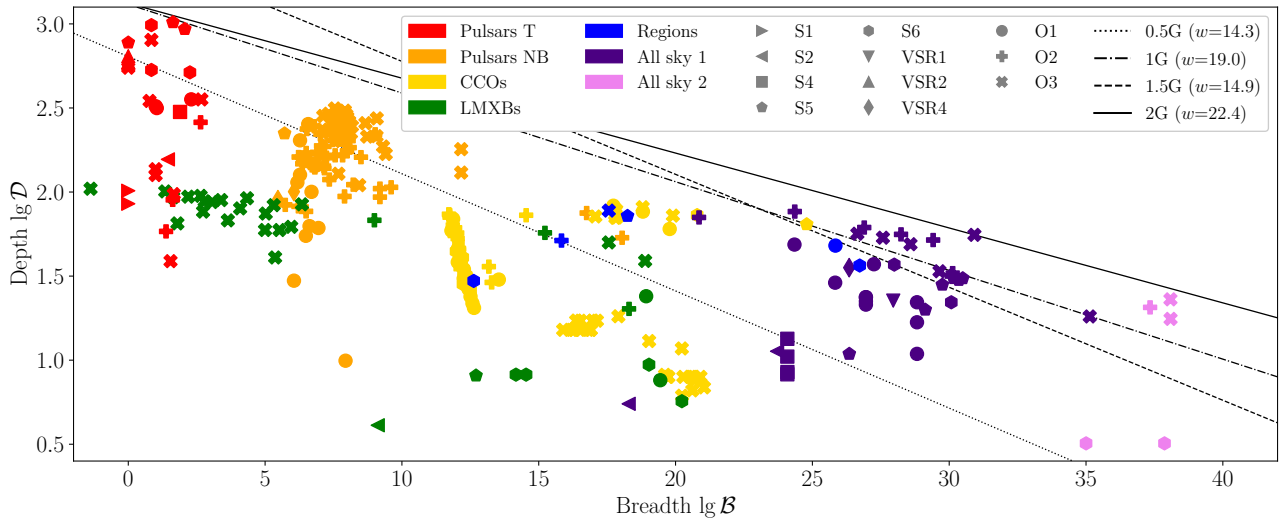


Figure 6: Sensitivity depth $\lg \mathcal{D}$ versus parameter-space breadth $\lg \mathcal{B}$ for 297 CW searches. Colours denote classification into seven search categories (see Sec. 6): targeted (“Pulsars T”) and narrow-band (“Pulsars NB”) searches for known pulsars; directed searches for central compact objects (CCOs) and low-mass X-ray binaries (LMXBs); searches directed at interesting regions of the sky (“Regions”); and all sky searches for isolated neutron stars (“All sky 1”) and neutron stars in binary systems (“All sky 2”). Markers denote the data used by each search (Table 2). The lines represent the weight w used to calculate the weighted volume \mathcal{V} for each detector generation; see Sec. 6 for details.

non-axisymmetry (Sec. 2.1.4). Based on the torque balance upper limit [Eq. (34)], which scales with the observed X-ray flux, Scorpius X-1 (Sco X-1) is the most promising LMXB for CW emission, and has been the primary target of searches to date [138, 139]. Its sky position is well defined, but its spin frequency is unknown [140], and searches must cover (roughly in order of increasing range) P , t_{asc} , a_p , and f . Other LMXBs, where the spin frequency is known from X-ray outbursts, require smaller parameter spaces [141]. An additional challenge is that, due to the time-varying accretion torque, f is likely to wander stochastically over long timescales [142].

5. Searches directed at interesting regions of the sky (“Regions” in Fig. 6). These searches focus on multiple astronomical objects concentrated in a particular region of space, generally chosen for its prospects of containing young neutron stars [143]. These include the Galactic centre [144], globular clusters, and star-forming regions. Searches must cover a wide range of frequencies and spindowns, and possibly multiple sky positions.
6. All sky searches for isolated neutron stars (“All sky 1” in Fig. 6). These searches target unknown, isolated neutron stars in the Galaxy. There are expected to be 10^8 – 10^9 such stars [145], of which only $\approx 10^3$ are observed as pulsars [146]. It is hoped that a sub-population of these neutron stars will be strong gravitational wave emitters, known as *gravitars* [147–150]. Searches cover a 4-dimensional parameter space: sky, frequency, and spindowns [86, 88].

7. All-sky searches for neutron stars in binary systems (“All sky 2” in Fig. 6). These searches target unknown Galactic neutron stars in binary systems, and cover a 6-dimensional parameter space of the sky, frequency, and binary orbital parameters [151, 152]. It is assumed, based on known pulsar observations, that the orbits will be close to circular, and so we can avoid the additional computational expense of searching over the higher-dimensional eccentric orbital parameters.

Figure 6 illustrates that CW searches generally trade-off between high sensitivity, or broad parameter-space coverage. The seven search categories group searches along a spectrum of trade-offs between depth and breadth: targeted searches achieve the greatest sensitivity depth over a limited parameter space, which all-sky searches for binary systems cover the widest parameter spaces at limited sensitivity depths, and generally the other categories fall somewhere in between. (An exception are the LMXB searches performed in [141] where, due to the known spin frequencies of the targets, the parameters spaces are relatively small and more closely resemble the narrow-band pulsar searches.) Noting the data used by each search (Table 2), we see that search depth has typically increased with time; given that \mathcal{D} factors out improvements in detector sensitivity (i.e. S_h), this represents an improvement in CW search techniques themselves. To date, the deepest CW search is a targeted pulsar search of S5 data [30], while the broadest search is an all-sky search for binary neutron stars in O3 data [152].

The parameter spaces of the (targeted, narrow-band) known pulsar searches have remained similar from run to

run (Fig. 6), as they scale with the number of known pulsars within the sensitive band of the detectors $f_{\text{rot}} \gtrsim 50$ Hz; this population of relatively fast-spinning pulsars has grown modestly over time. Similarly, searches for the LMXBs Sco X-1 and XTE J1751–305 (green markers with $\lg \mathcal{B} \gtrsim 9$) have covered generally the same parameter spaces, as e.g. for Sco X-1 the uncertainties in its orbital parameters from electromagnetic observations have remained broadly similar over time [153–156]. In contrast, parameter-space coverage of all-sky isolated searches initially saw dramatic increases, from $\lg \mathcal{B} \approx 18$ in the S2 run to ≈ 30 by the 1G detector era (Tables 2, A.3), where searches in subsequent runs have clustered. The CCO, regional, and all-sky binary searches have seen more mixed evolution in parameter-space coverage, due to different targets and search design choices; e.g. CCOs have typically been targeted using either fully-coherent searches over a limited data sets, or searches of all the data from a run using computationally cheaper, less sensitive algorithms.

Given the inverse correlation between depth and breadth, we might suppose that their product – a sensitivity depth-parameter space *volume* – might serve as a useful figure of merit for CW searches. Given the very different scales of \mathcal{D} and \mathcal{B} , however, it seems naive to simply multiply them. Instead, I define a weighted volume

$$\mathcal{V} = \mathcal{D}^w \mathcal{B}. \quad (77)$$

The weight w is chosen separately for each detector generation (as defined in Table 2) as follows. For a given detector generation, select the two searches with: the maximum \mathcal{D} , and the maximum \mathcal{B} . Then, define w as

$$w = -\frac{\log \mathcal{B}^{\max \mathcal{D}} - \log \mathcal{B}^{\max \mathcal{B}}}{\log \mathcal{D}^{\max \mathcal{D}} - \log \mathcal{D}^{\max \mathcal{B}}}, \quad (78)$$

where $\mathcal{D}^{\max \mathcal{D}}$ and $\mathcal{B}^{\max \mathcal{B}}$ denote a quantity from the search with the maximum \mathcal{D} and \mathcal{B} respectively. Geometrically, a line drawn on Fig. 6 with slope $-1/w$ and appropriate intercept would pass through both the maximum \mathcal{D} and maximum \mathcal{B} searches selected to calculate w .

For each detector generation, lines are drawn in Fig. 6 with slopes $-1/w$. The intercepts of each line are chosen such that the line passes through the search with the maximum \mathcal{V} for that detector generation; note that this search is not necessarily either of the searches with the maximum \mathcal{D} and \mathcal{B} used in compute w . The weights found for each detector generation are given in the legend of Fig. 6. We see that w increases with each generation, reflecting the general trend that CW searches have increased more in depth than in breadth over time.

We should be cautious about using \mathcal{V} as a single ranking measure to decide which CW search is “best”. In addition to the many difficulties to fairly comparing searches (as discussed above in this section, and in Sec. 4.1), we note the following properties of w . First, w is defined separately for each detector generation, and hence follows changes in CW search design and algorithm over time, rather than

giving a time-independent “best” ranking. Second, w is defined by two extreme searches within a detector generation cohort – those with the maximum \mathcal{D} and maximum \mathcal{B} . The \mathcal{V} computed for each search, therefore, depends on which other searches are present in the cohort; addition of new searches with greater \mathcal{D} or \mathcal{B} would change w and therefore the \mathcal{V} of all searches. Consistent with the spirit of this review, we interpret \mathcal{V} as representing the general trend in CW search performance over time and within detector generation cohorts.

Figure 7 plots the weighted volume \mathcal{V} of each CW search against time. We can see a marked increase in volume from 2003 to 2010, corresponding to the initial 0.5–1.5G detectors, followed by a plateau from 2010 to 2016 as the detectors upgraded to the 2G generation. Since 2016 \mathcal{V} has continued to increase, albeit more moderately. Together with Fig. 6, this suggest that CW searches were initially driven by increasing parameter-space coverage in the 1G detector era, but have increasingly been driven by improving sensitivity depth (albeit at a slower rate) in the 2G detector era.

We also see an increased concentration in number of searches performed in the 2G detector era. This reflects increased activity within the Continuous Wave Working Group and from other CW research groups, as well as a growing diversity of CW search algorithms and astronomical targets. It also suggests a shorter cadence from the acquisition of data to the submission of searches for publication, driven by deepening experience of the field with all aspects of search design and execution. Higher quality data with greater incentives to perform analyses, more frequent observing runs, and shorter proprietary periods for LIGO and Virgo data sets may also be relevant factors.

In addition to an increasing density of searches, we also see a broader range in the \mathcal{V} of searches performed in the 2G detector era. In the early years of the field, many CW searches were the first of their kind, and therefore faced little competition. As the number of searches increases, there is likely a desire for each search to differentiate itself from other searches in terms of design and algorithm choices. There is a tradition of multiple CW pipelines covering similar parameter spaces [e.g. 100], in order to guard against software bugs in one pipeline preventing a detection. This essential redundancy must nonetheless be balanced against putting too many resources into analysing identical parameter spaces, and practical concerns such as being able to publish searches which are sufficiently novel.

The broadened range of \mathcal{V} in the 2G detector era suggests that, in seeking to differentiate searches from each other, CW analysts are not solely driven by maximising the obvious metrics of sensitivity depth and parameter-space breadth, but also by other considerations. These include focusing on parameter spaces which are interesting for astrophysical reasons, if not for their size. For example, both the Crab pulsar [157] and PSR J0537–6910 [106, 158] has received special interest in recent years as potential sources of r -mode emission; in particular, obser-

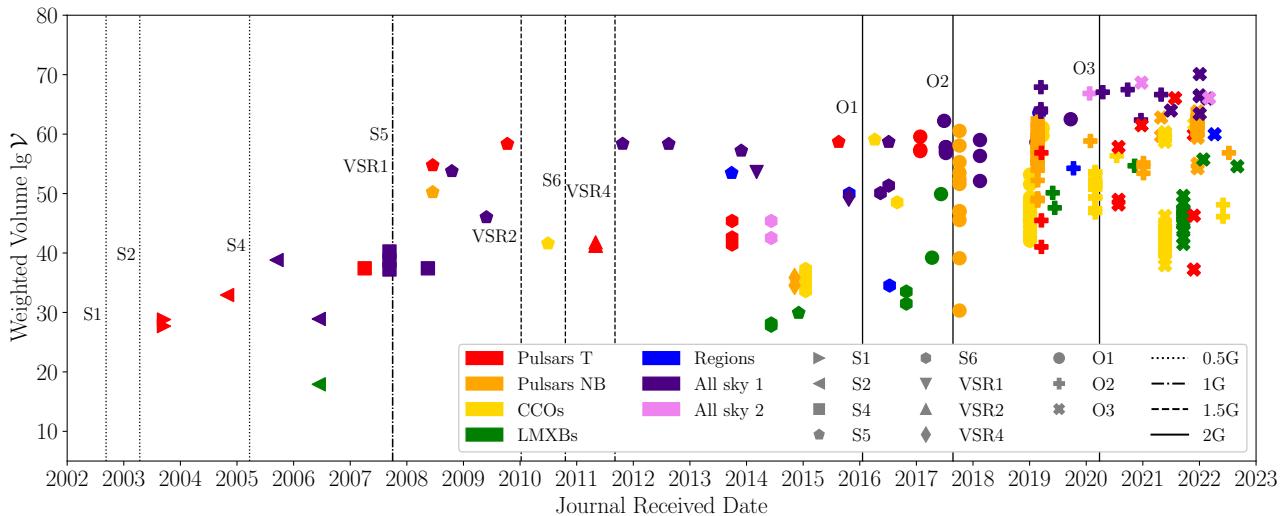


Figure 7: Weighted sensitivity depth-parameter space volume \mathcal{V} of 297 CW searches versus time (given by the journal submission date of the article presenting each search). Colours and markers have the same meanings as in Fig. 6. Vertical lines (with labels on the left) indicate the end date of each data collection run listed in Table 2.

variations of PSR J0537–6910 suggest that, in between frequent glitches, its spindown rate is consistent with a braking index of $n = 7$ which would be consistent with r -modes [159, 160]. Another factor is the expansion of the CW signal space beyond the model of Sec. 2, e.g. by using HMMs (Sec. 7.2.7) which permit the CW signal frequency to randomly wander. Such considerations are not easily captured by the simple metrics used in this section.

7. Continuous wave search algorithms

In this section, I review the algorithms and pipelines used in the CW searches examined in Sec. 6. Following the spirit of the previous section, I aim to qualitatively compare the different algorithms to illustrate general principles and trends. I refer the reader to the cited references for technical descriptions of each algorithm.

Given a model for the CW signal waveform (Sec. 2), the optimal algorithm is to simply match filter the whole data set against the model over the parameter space of interest. While this approach is possible when all phase parameters of the signal are well known, such as for targeted and narrow-band searches for known pulsars, it is otherwise not achievable over any wide parameter space. Let us demonstrate this concretely by attempting to perform an all-sky search of 1 year of data, covering typical ranges of $f \in [50, 1000]$ Hz and $\dot{f} \in [-10^{-8}, 0]$ Hz s $^{-1}$. Applying for formulae for parameter-space breadth given in Sec. 4.2, we calculate $\mathcal{B}_{\text{sky}} = 9.9 \times 10^{12}$, $\mathcal{B}_f = 4.0 \times 10^{10}$, $\mathcal{B}_{\dot{f}} = 2.3 \times 10^{06}$, and $\mathcal{B} = 9.2 \times 10^{29}$. Let us assume that \mathcal{B} gives the rough order of magnitude for the number of matched filters we must apply to the data to cover this parameter space. On contemporary computer hardware, it takes $\approx 8.1 \times 10^{-4}$ s to apply one matched filter to a year’s

worth of data [161]. The computational cost of our search is therefore $\approx 2.3 \times 10^{19}$ yr. We could then complete the search with ~ 5 billion computers running for ~ 5 billion years – just in time before the Sun becomes a red giant and engulfs the Earth. . .

Given this obvious impracticality, CW search algorithms designed to cover wide parameter spaces all follow a *hierarchical* structure [118, 162, 163]. To start, the whole data set (with time-span T) are partitioned in time into N segments, each of which span a *coherence time* $T_{\text{coh}} \ll T$. In the first, *coherent stage* of the hierarchical pipeline, matched filters covering the phase parameter space of interest are applied to each segment individually. The number of matched filters required generally scales with $T_{\text{coh}}^{\tilde{\delta}}$, with $\tilde{\delta} \gtrsim 6$ [164]. (Consider the powers of T in the breadth formulae given in Sec. 4.2.) This steep scaling is too computationally expensive for a fully-coherent search, but we can choose T_{coh} to be short enough to make the computational cost manageable.

In the second, *semi-coherent stage* of the hierarchical pipeline,¹¹ an algorithm is selected to apply to the matched filter results from the N segments. Over the same phase parameter space as the coherent stage, this algorithm adds together N matched filter results from the N segments in a manner consistent (to a degree specified by the algorithm) with the CW signal waveform over the whole data set. In general, semi-coherent algorithms do not require the *phase* of the CW signal $\phi(t_{\text{NS}})$ [Eq. (38)] to be con-

¹¹This stage is sometimes referred to as the “incoherent” stage; the term “semi-coherent” is also often used to describe a hierarchical pipeline as a whole. In this review I use “semi-coherent” to refer specifically to the algorithm used in the second stage, and “hierarchical” to refer to the pipeline as a whole. See [165] for a study of hierarchical pipelines with more than two stages.

sistent over all segments; instead, they require only that the *frequency* of the CW signal $f(t_{\text{NS}})$ [Eq. (37)] be consistent. Put another way, the phase is allowed to jump by some random offset from segment to segment, while the frequency remains consistent across segments:

$$\begin{aligned}\phi(t)_{N+1} &= \phi(t)_N + \phi_{\text{random}}, \\ 2\pi f(t)_{N+1} &= \frac{d\phi(t)_N}{dt} + \frac{d\phi_{\text{random}}}{dt} \\ &= \frac{d\phi(t)_N}{dt} + 0 = 2\pi f(t)_N,\end{aligned}\quad (79)$$

where \cdot_{N+1} and \cdot_N label the $(N+1)$ th and N th segments respectively.

Relaxing phase consistency between segments reduces sensitivity, and makes the detection statistic computed by the semi-coherent algorithm more susceptible to instrumental line artefacts at near-constant frequencies [166]. The significant benefit of this approach, however, is that the computational cost of the semi-coherent stage no longer scales as $T^\delta = N^\delta T_{\text{coh}}^\delta$, but as $N^{\hat{\eta}} T_{\text{coh}}^{\hat{\delta}}$ with $\hat{\eta} \ll \hat{\delta} \lesssim \tilde{\delta}$ [164]. This saves a factor $\sim N^{\tilde{\delta}-\hat{\eta}} T_{\text{coh}}^{\tilde{\delta}-\hat{\delta}}$ in computational cost compared to a fully-coherent analysis, which is generally substantial enough to make hierarchical searches of year-long data sets tractable. Indeed, given the constraint of a fixed computing budget [164], a hierarchical search is often *more sensitive* than a fully-coherent analysis, simply because it is computationally cheap enough to be able to analyse all available data; a fully-coherent search, on the other hand, would be forced to analyse only a subset of the data, due to its steep computational cost scaling with T , and would thereby degrade in sensitivity.

In the remainder of this section I review the algorithms typically employed at the coherent (Sec. 7.1) and semi-coherent (Sec. 7.2) stages of a hierarchical pipeline. Other algorithms and applications are briefly mentioned in Sec. 7.3.

7.1. Coherent matched filtering algorithms

Figure 8 plots \mathcal{D} and \mathcal{B} for each search against the coherence time T_{coh} used in the first coherence stage. (Where a search uses more than one coherence time, the maximum $T_{\text{coh,max}} = \max T_{\text{coh}}$ is shown.) We immediately see that search sensitivity increases with longer coherence times, but parameter-space coverage decreases due to the steep increase in computational cost with T_{coh} . The four coherent algorithms labelled in the figure are described in the remainder of this section.

7.1.1. Frequency-domain power

Over a “short enough” time T_{coh} , the CW signal frequency is approximately constant. In this case, the simplest coherent algorithm is to compute the discrete Fourier transform of a data segment, and then compute the power (i.e. the sum of the squares of the real and imaginary Fourier components) of the bin where the CW signal is expected to be. The condition for T_{coh} to be “short enough”

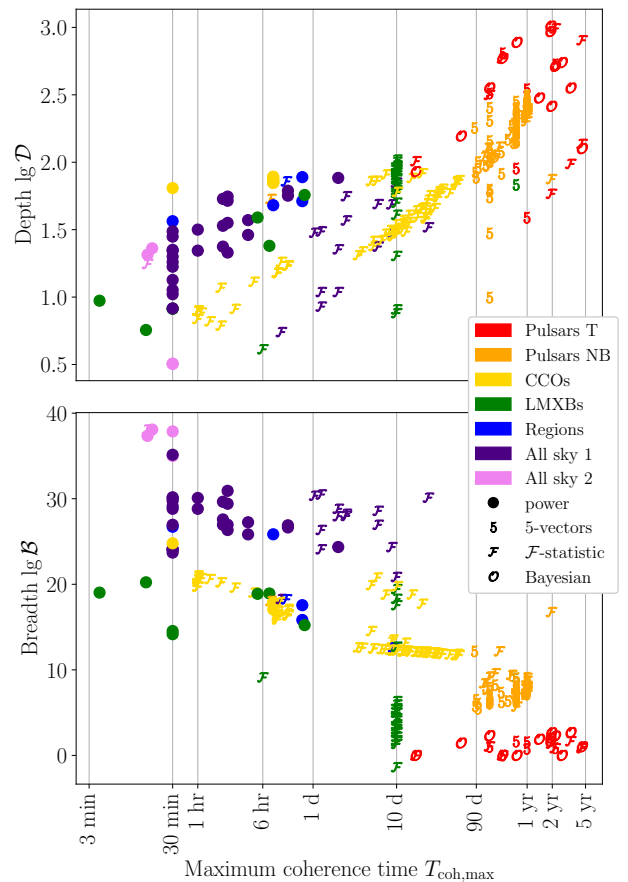


Figure 8: Sensitivity depth \mathcal{D} (top panel) and parameter-space breadth \mathcal{B} (bottom panel) of 297 CW searches, plotted against the maximum coherence time $T_{\text{coh,max}}$ used in each search. Colours have the same meanings as in Fig. 6; markers denote the coherent algorithm employed by each search (described in Sec. 7.1).

so that the CW signal power is concentrated in one bin is, more precisely,¹²

$$T_{\text{coh}}^2 \leq \frac{6\sqrt{5}\mu_{T_{\text{coh}}}}{\pi \max\{f\} \max\{\tau_s, a_p\} \max\{\Omega_s^2, \Omega_p^2\}} \quad (80)$$

where: $\mu_{T_{\text{coh}}}$ sets the fraction of signal power we are prepared to lose for a particular choice of T_{coh} ; $\max\{f\}$ is the maximum frequency over the parameter space; $\max\{\tau_s, a_p\}$ is the maximum of the Earth’s radius (Sec. 4.2.2) and the searched binary orbit projected semi-major axis (if any); and $\max\{\Omega_s^2, \Omega_p^2\}$ maximises the square of either the Earth’s sidereal angular frequency or (if any) the searched angular frequency of a binary orbit.

Gravitational wave data, divided into segments of time-span T_{coh} as above and Fourier transformed, serves as a common input data product, not only for semi-coherent algorithms that sum power in each segment, but also for

¹²Equation (80) is derived in [85] for any Rømer delay, and implemented as given in the function `XLALFstatMaximumSFTLength()` of the LALSuite [167] software package.

algorithms such as the \mathcal{F} -statistic (Sec. 7.1.3). Common file formats are the Short Fourier Transform (SFT; [168]) format, and the Short FFT DataBase (SFDB; [169]).

7.1.2. 5-vectors algorithm

The 5-vectors method [170, 171] is based on the following property of the CW signal; when the phase parameters of the signal are fully specified (i.e. we know precisely the function $h_+(t), h_\times(t)$ in Eq. (1)), one is left with only the modulation from the detector responses $F_+(t), F_\times(t)$. These functions are periodic, with angular frequencies of Ω_s and $2\Omega_s$. Their effect on a CW signal with known angular frequency $2\pi f(t)$ is to generate four side-bands, at $2\pi f(t) \pm \Omega_s, 2\pi f(t) \pm 2\Omega_s$, resulting in five harmonics in total. The 5-vectors method sums these 5 harmonics, with appropriate weights derived from $F_+(t), F_\times(t)$.

To date, the 5-vectors method has been mostly used as a fully-coherent algorithm for targeted and narrow-band searches for known pulsars. The phase demodulation of the signal using the known $h_+(t), h_\times(t)$ is accomplished efficiently using the Band-Sampled Data (BSD; [172]) framework, which provides band-limited data, heterodyned at regular intervals (typically 10 Hz), and down-sampled to speed up further computations. The method was extended in [173] to perform directed searches for LMXBs.

7.1.3. \mathcal{F} -statistic

The \mathcal{F} -statistic is the log-likelihood function of the observed data given a CW phase modulation, maximised over the four amplitudes of Eq. (52); see Sec. 3. It is extensively studied in a series of papers [23, 174–177], the first of which is colloquially referred to by CW analysts as “JKS”. It has been employed in a wide variety of CW searches: for known pulsars (as a full-coherent search), directional targets such as CCOs and LMXBs (both fully-coherently and as the first stage of a hierarchical pipeline), and all-sky searches (as part of a hierarchical pipeline).

The \mathcal{F} -statistic has the following statistical properties. In the absence of a signal, and assuming Gaussian noise, the value of $2\mathcal{F}$ follows a central chi-squared distribution with four degrees of freedom. When a signal is present, $2\mathcal{F}$ follows a non-central chi-squared distribution with four degrees of freedom and non-centrality parameter ρ^2 . Here, ρ^2 is the optimal signal-to-noise ratio when signal and template are perfectly matched [23]. Due to these useful properties, explicit values of the \mathcal{F} -statistic quoted in the literature are usually values of $2\mathcal{F}$ and *not* values of \mathcal{F} .

Several implementations of software to compute the \mathcal{F} -statistic have been developed. A time-domain implementation [178] uses the “resampling” technique first proposed in [23]. This technique uses the Fast Fourier Transform to simultaneously compute N values of $2\mathcal{F}$ at regularly-spaced frequencies. The computational cost of resampling scales as $\mathcal{O}(\log N)$, whereas computing each value of $2\mathcal{F}$ individually would scale as $\mathcal{O}(N)$. The LALSuite [167] software package contains an independent implementation of the “resampling” technique [161, 179–181] which takes

frequency-domain SFT data files as input. LALSuite also contains another frequency-domain technique, known as “demodulation”, which efficiently computes individual $2\mathcal{F}$ values [161, 182, 183].

For neutron star sources in binary orbits, we must demodulate the signal phase according to $\Delta_R(t_{\text{NS}})$ (Sec. 2.2.2). An alternative technique [184] is to compute the \mathcal{F} -statistic omitting $\Delta_R(t_{\text{NS}})$ from the phase; the signal is then split into multiple side-bands according to the Jacobi-Anger expansion [cf. 185]. A subset of the side-bands may then be added together to recover the \mathcal{F} -statistic.

7.1.4. Bayesian inference

Bayes’ theorem gives the probability of a model, given some observed data – the posterior probability – from the following ingredients: a prior probability for the model, the likelihood of the data given the model, and the evidence (or marginal likelihood). Provided that the prior probability distributions are consistent with the population of signals one expects to detect, Bayesian inference provides the most powerful detection statistic [95]. The \mathcal{F} -statistic, for example, does not satisfy this criteria; the maximisation over the \mathcal{A}^i amplitudes implicitly assumes unphysical prior distributions for the underlying model parameters h_0 and $\cos \iota$ [96].

A Bayesian inference pipeline is used to perform surveys of the known pulsars. The relative flexibility of Bayesian inference, compared to ad-hoc constructed statistics, permits the use of the complicated pulsar timing model [92, 186], including eccentric binary orbits and irregular timing noise [187, 188]. The pipeline first heterodynes the data at the prescribed CW phase inferred from the pulsar ephemeris, then computed posterior probabilities on the four physical amplitude parameters $h_0, \cos \iota, \psi, \phi_0$.

The first implementation of the pipeline [189] computed the posterior probability using a Markov Chain Monte Carlo (MCMC). A more efficient implementation [190] uses nested sampling [191]. It is able to search over small ranges of the phase parameters, quantify detection significance, and perform model comparison. It can also search at both harmonics of the CW signal [30], and model gravitational wave polarisations predicted by theories of gravity other than general relativity [192]. This implementation is part of LALSuite [167]. A third generation of the pipeline [193] is written in Python, and can use a variety of Bayesian inference solvers via [194].

7.2. Semi-coherent algorithms

Figure 9 plots \mathcal{D} versus \mathcal{B} , as in Fig. 6; here, however, we highlight the 13 semi-coherent algorithms used by the searches, by plotting polygons whose vertices are the searches. The polygons illustrate the area in \mathcal{B} - \mathcal{D} space each algorithm is demonstrably capable of operating over; this gives some idea of the typical configurations, and the flexibility thereof, for each algorithm. For example, the Viterbi HMM algorithm (Sec. 7.2.7) is capable of a

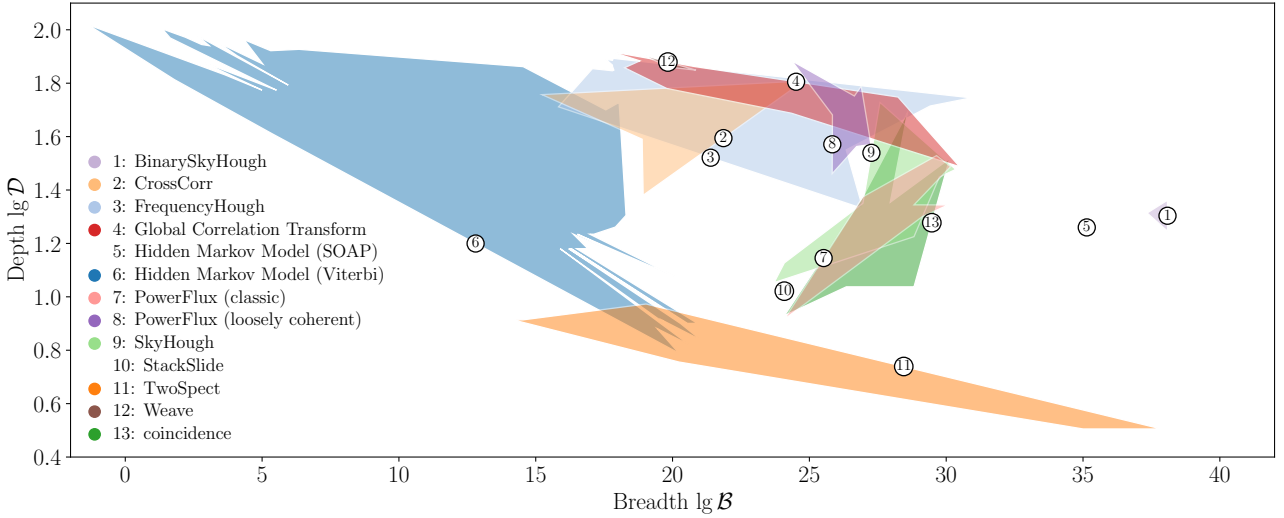


Figure 9: Sensitivity depth $\lg \mathcal{D}$ versus parameter-space breadth $\lg \mathcal{B}$ for 297 CW searches. Plotted are polygons, each of whose vertices indicates a CW search using a given semi-coherent algorithm. Names of all semi-coherent algorithms are listed in the legend. Each polygon is given a numeric label, placed on an arbitrary edge, corresponding to the legend. Where only one CW search uses a particular semi-coherent algorithm, no polygon is plotted and instead the numeric label marks the search ($\lg \mathcal{B}, \lg \mathcal{D}$). Colours are arbitrary.

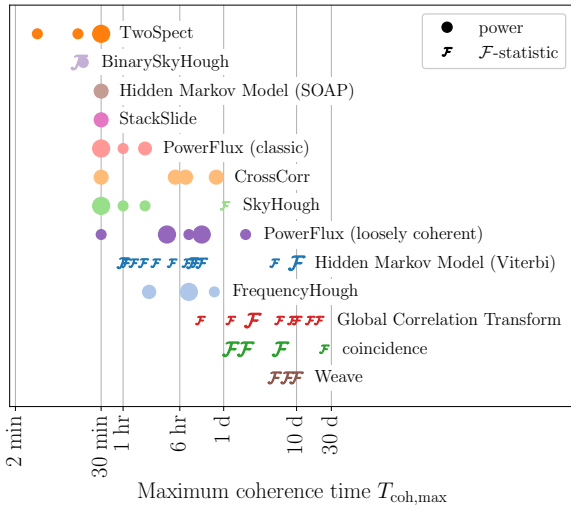


Figure 10: Maximum coherence times $T_{\text{coh,max}}$ chosen by the semi-coherent algorithms used in 297 CW searches. Colours are arbitrary but are the same as in Fig. 9; markers denote the coherent algorithm used by the hierarchical pipelines; marker size indicates the relative popularity of a particular choice of $T_{\text{coh,max}}$ for a given algorithm.

wide variety of configurations due to its computational efficiency; while the TwoSpect algorithm (Sec. 7.2.6), which is specialised for neutron stars in binary systems, can be configured for both all-sky surveys (higher \mathcal{B}) and directed targets (lower \mathcal{B}). Many algorithms have a traditional focus on a particular parameter space. The following algorithms have typically been used for all-sky searches for isolated neutron stars: coincidence (Sec. 7.2.1), SkyHough and FrequencyHough (Sec. 7.2.2), StackSlide, Global Correlation

Transform (Sec. 7.2.3), and PowerFlux (and its loosely coherent extension; Sec. 7.2.4). CrossCorr (Sec. 7.2.5) focuses on LMXBs, Sco X-1 in particular, while BinarySkyHough (Sec. 7.2.2) is designed for all-sky searches for neutron star in binaries. Relatively newer algorithms, such as Weave (Sec. 7.2.3) and the SOAP HMM algorithm (Sec. 7.2.7) have only been used in a few searches to date.

Figure 10 plots the maximum coherence time $T_{\text{coh,max}}$ typically chosen for each semi-coherent algorithm. (A reminder that $T_{\text{coh,max}}$ is the maximum T_{coh} used by a given search, in cases where more than one coherence length is employed.) Seven of the 13 semi-coherent algorithms use power (Sec. 7.1.1) as the first-stage coherent algorithm; four of the 13 use the \mathcal{F} -statistic (Sec. 7.1.3); and two of the 13 may use either. For semi-coherent algorithms using power, $T_{\text{coh}} = 30$ min is a popular choice of coherence time as it satisfies Eq. (80) up to $f \lesssim 2$ kHz,¹³ and for that reason is the standard choice of time-span for SFTs. Longer coherence times are possible when summing power at lower frequencies; on the other hand, searches over binary orbit parameters may require shorter SFTs if $\Omega_P < \Omega_s$ [Eq. (80)]. Semi-coherent algorithms which use the \mathcal{F} -statistic are generally not restricted by Eq. (80), except that computational cost scales steeply with T_{coh} .

The remainder of this section outlines the semi-coherent algorithms referenced in Figs. 9 and 10. In essence, each algorithm ultimately performs the same task: to correctly demodulate the CW signal frequency, while allowing some flexibility in the CW signal phase per Eq. (79). That said,

¹³This is the upper frequency limit on CW searches imposed by the 4 kHz sampling rate of the calibrated $h(t)$ data prepared by the LIGO Scientific Collaboration and Virgo Collaboration.

the algorithms vary considerably in their conceptual basis and design choices.

7.2.1. Coincidence-based algorithms

The simplest method of stitching together the N segments is to not do so; coincidence-based algorithms do not attempt to add together results across segments from the coherent stage. Instead, each segment is treated as an independent search, and coincidences are sought between significant candidates from each segment [178]. Candidates may be considered coincident e.g. by binning their parameters over a grid, thereby collecting candidates with similar parameters [195].

The coincidence method is potentially less sensitive than other semi-coherent methods. For example, a weaker signal may become detectable by building up signal power over segments, whereas it could be lost if it fails to pass a per-segment threshold. This method does have the advantage, however, of sparing the computational expense the second semi-coherent stage. Moreover, it can be applied to data in (relatively) real time – as soon as T_{coh} worth of data is collected and prepared – rather than having to wait until the end of the run for all the data to be collected. The coincidence method has been used in all-sky searches for isolated pulsars.

7.2.2. Hough transform algorithms

The Hough transform [196] is a pattern recognition algorithm originally developed to find particle tracks in bubble chamber photographs. Let us suppose we are analysing a two-dimensional image (x, y) in search of straight line patterns, i.e. of the form $y = mx + c$. The Hough transform is a one-to-many mapping from (x, y) to the set $\{(m, c)\}$ of every line that passes through (x, y) . Now suppose there is a straight line artefact $y = m_0x + c_0$ in the image; as each point (x, y) along the line is mapped, their corresponding sets $\{(m, c)\}$ will intersect at the true parameters of the line (m_0, c_0) . Such intersections may be found by binning mapped sets $\{(m, c)\}$ over a grid in (m, c) , and seeing which bins accumulate the most counts.

The Hough transform has generally been applied to all-sky CW searches. Because it is a two-dimensional transform, one must select two dimensions from the (at least) four dimensions of the all-sky parameter space to apply the transform on. This has led to two implementations: SkyHough [197, 198], which applies the Hough transform to the sky parameter space at fixed frequency and spindown; and FrequencyHough [199, 200], which applies the Hough transform to the frequency–spindown parameter space at fixed sky position. Aside from this choice, the two implementations operate in a similar manner, as follows.

A Hough transform pipeline starts with matched filter results, for each segment, from the first coherent stage; these are usually power, although [201] used the \mathcal{F} -statistic. They then require each matched filter result pass a threshold and be a local maxima with respect to neighbouring filters. This selects a collection of points in the domain of

the Hough transform, known as a *peak map*. The Hough transform is then applied to the peak map, and its results are binned into a grid called a *partial Hough map*; each grid cell is one if it contains a value of the transform, or zero otherwise. Finally, the remaining dimensions of the search parameter space are considered (frequency and spindown for SkyHough, sky position for FrequencyHough): for each vector of parameters selected from these dimensions, the partial Hough maps consistent with a CW signal with these parameters are summed over segments to give a *total Hough map*. The final output of the SkyHough (FrequencyHough) pipelines are total Hough maps over the sky (frequency–spindown) parameter spaces, for fixed values of frequency and spindown (sky position). The detection statistic in each bin of the total Hough map is the *number count*; the number of segments (out of N) in which the corresponding bin of the partial Hough maps registered a one.

Further developments of each implementation have included: weighted summing of the partial Hough maps to account for the amplitude modulation of the CW signal [202, 203]; BinarySkyHough, an extension of the SkyHough implementation to efficiently search over binary orbital parameters [204]; extensions of the FrequencyHough implementation to perform directed searches (i.e. at fixed sky position) efficiently using the BSD framework [205], and to search over binary orbital parameters [206]; and adaptations of the Hough transform beyond the CW realm to search for long-duration but transient gravitational wave signals [207, 208].

7.2.3. StackSlide algorithms

The StackSlide algorithm [163, 209] is based on the following mental picture. Imagine taking a set of SFTs, computing their power spectra, and (taking each spectrum as a vertical column) “stacking” them along a horizontal time axis; the result is a time-frequency plane of power versus time. In this plane, a CW signal would appear as a wavy horizontal line, due to the various modulations of its frequency $f(t)$ [Eq. (37)]. Now imagine, for a given vector of sky and spindown parameters, “sliding” each spectra up and down so as to demodulate the signal, i.e. so that the wavy horizontal line is now perfectly straight. Finally, sum up the frequency bins of the spectra (in their post-“sliding” positions) over time; this accumulates CW signal power over time for a range of frequencies. The summed StackSlide power is distributed according to a chi-squared distribution with $2N$ degrees of freedom [209]. Only one StackSlide-on-power search has been performed [100].

The StackSlide concept has been generalised to use the \mathcal{F} -statistic instead of power, as input [163]. Here, the concept of “sliding” the power spectra of each segment is made concrete by the construction of *coarse* and *fine* grids, as follows. First, in the coherent stage, for each segment, we compute the \mathcal{F} -statistic over the coarse grid: a grid of points in the search parameter space appropriate for an \mathcal{F} -statistic search over time-span T_{coh} , constructed e.g.

by using the parameter-space metric (Sec. 4.2) to decide on the spacings between grid points. In the semi-coherent stage, we then construct the fine grid: here the grid must be appropriate for an *incoherent* sum of \mathcal{F} -statistic values. This requirement is easily satisfied using the parameter space metric; given the *coherent metrics* computed for the N coarse grids in each segment, the *semi-coherent metric* is given by the average¹⁴ of the N coherent metrics. Typically, the fine grid contains γ more points per unit parameter space volume than the average coarse grid; γ is known as the *refinement factor*.

Next, each coarse grid is interpolated onto the fine grid: for each fine grid point, and for each segment, we find and record the coarse grid point to which the fine grid point is “closest” (in the sense of the coherent parameter-space metric for that segment). This gives a one-to- N mapping from each fine grid point to its closest coarse grid points in each segment. Finally, for each fine grid point, the N values of $2\mathcal{F}$ corresponding to its N closest coarse grid points are summed. The output detection statistic is distributed according to a chi-squared distribution with $4N$ degrees of freedom [209].

Implementation of the StackSlide algorithm with the \mathcal{F} -statistic requires knowledge of the coherent and semi-coherent parameter-space metrics. The coherent \mathcal{F} -statistic metric, both its most general form and the phase metric approximation, are detailed in [35]. A particularly desirable property is for the metrics to be *flat*, i.e. $g_{ij}(\vec{p}) = g_{ij}$ is constant with respect to the phase parameters. This property facilitates generation of *template banks* – i.e. grids – which minimise the number of templates and hence computational cost [115–117, 210], although such template banks may not be optimal for detection [211, 212].

An important limitation of the metric is that it is only a quadratic approximation to the true loss of signal power, and therefore remains valid only for relatively small mismatches $\mu \lesssim 0.4$ [35, 93]. As discussed in [213], the semi-coherent mismatch *rarely* satisfies this requirement, due to computational constraints that limit the size of the fine template bank. Nevertheless, empirical studies show that the loss of signal power progresses slowly even at very large mismatches (beyond the domain of validity of the metric). In practise, therefore, StackSlide searches can still achieve good sensitivity; even if the fine grid must be constructed with a large ($\gtrsim 1$) *metric* mismatch μ , the true loss of signal power will still be reasonable. An alternative to the quadratic metric approximation is proposed in [214].

Building on studies of large-scale correlations in phase parameter space [215, 216] and of simplified CW phase models [174], the Global Correlation Transform (GCT)

was derived in [217, 218]. The GCT introduces new phase parameters, where a Taylor expansion of the orbital motion of the Earth is absorbed into new frequency and spindown coordinates. Because such a Taylor expansion remains valid only for $T \ll 1$ year, the GCT metric significantly underestimates the loss of signal power over realistic observing times. Nonetheless, the GCT remains in use for all-sky CW searches.

The supersky metric [93, 219] expands upon some of the ideas of the GCT, while addressing its limitations. The sky parameter space is projected from the 2-sphere to three dimensions, then projected back onto a two-dimensional plane, which corresponds to either the equatorial plane of the Earth’s equator (for short T) or the ecliptic plane of its orbit (for long T). The projection is accomplished by absorbing linear and quadratic (with T) terms in a Taylor expansion of the Earth’s orbital motion into new frequency and spindown coordinates, respectively, while retaining higher-order terms which become important at longer T . Combined with an optimal lattice-based template bank [117], a StackSlide search pipeline based on the supersky metric was implemented, known as Weave [220], and demonstrated improved sensitivity compared to the GCT [221]. Weave requires sufficient computer memory to store the $2\mathcal{F}$ values needed for the one-to-many fine-to-coarse-grid mapping, which may limit its usage in some circumstances [221]. To date Weave has been used for narrow-band searches for known pulsars, and for directed searches for CCOs.

7.2.4. PowerFlux algorithms

PowerFlux [100, 222] is an all-sky search pipeline for isolated neutron stars. It may be seen as an extension of the StackSlide-on-power semi-coherent paradigm. The principal difference is that PowerFlux weights the power from each SFT by the detector response functions, thereby emphasising times during the day when, for a given sky position, the detector is most sensitive. PowerFlux also inversely weights the power from each SFT by its noise, thereby de-weighting times where detector sensitivity is degraded. The implementation of the method is highly optimised [222, 223] and is often used to perform “quick-look” searches of the early data from a run, taking advantage of the typical step-up in detector sensitivity after upgrades and commissioning between runs. PowerFlux has developed a procedure for computing h_0^C upper limits which are strictly conservative (i.e. worst case) even in the presence of spectral artefacts [224].

The loosely coherent extension to the classic PowerFlux algorithm [225, 226] generalises the concept of summation of SFT power over time. Instead, a two-dimension summation over all pairs of SFTs at times t_1, t_2 is considered, where a kernel function $K_{t_1, t_2}(\delta)$ with parameter δ ¹⁵ decides which pairs to add and with what weight.

¹⁴By “average”, we mean that the element \hat{g}_{ij} of the semi-coherent metric is given by $\hat{g}_{ij} = \sum_{k=1}^N \tilde{g}_{ij}^k$, where \tilde{g}_{ij}^k are the equivalent elements of the N coherent metrics. Note that coherent metrics *must* be computed using consistent definitions of the phase parameters; for example, the metric elements for frequency f must have been computed at the same reference time t_0 .

¹⁵Note that this is *not* the declination δ of the source’s sky position.

In this picture, summation of SFT power is equivalent to a kernel which is one when $t_1 = t_2$ and zero otherwise. The kernel blurs the distinction in the hierarchical search paradigm between the coherent and semi-coherent stages, and permits a smoother transition between full phase coherence and phase-incoherent power summing over a timescale determined by δ . It bears similarities with the cross-correlation method (Sec. 7.2.5) as well as the approaches of [227, 228]. The loosely coherent method was first developed to follow up candidates from an initial PowerFlux search, as it allows longer effective coherence times T_{coh} to be used, as seen in Fig. 10. A recent, fast implementation of the method called Falcon [229] enables loose coherence to also be used in the initial search.

7.2.5. Cross-correlation algorithms

Cross-correlation is a well-established concept in signal processing; it quantifies the similarity of two independent time series as a function of their relative time offset. It was first applied to gravitational wave data as a radiometer implemented in software [230] for finding unmodeled stochastic gravitational waves. A modelled cross-correlation algorithm was then developed to search for CW signals [231]. Similar to the kernel of loosely coherent PowerFlux, each pair of independent SFTs labelled I, J – from either different times, or different detectors – are cross-correlated with a filter Q_{IJ} . The filter weights each pair of SFTs according to how a given CW signal would appear in the two SFTs; it essentially performs the role of demodulating the signal in order to maximise signal-to-noise ratio. The filter can be tuned to select which SFTs to cross-correlate; correlating only SFTs close to each other in time recovers a power-like detection statistic, while correlating all SFTs recovers the \mathcal{F} -statistic. The cross-correlation method can therefore tune its degree of phase coherence in a more flexible manner than a traditional two-stage hierarchical search.

The first version of CrossCorr, an implementation of the cross-correlation algorithm, initially targeted a CCO in the supernova remnant SN 1987A [232]. A second version of CrossCorr has been used to target the LMXB Sco X-1 [233]. Recent developments include the addition of “resampling” for efficient computations over frequency [234], similar to the \mathcal{F} -statistic. Lattice template placement has been used to minimise computational cost, in particular by a choice of coordinate transform in the P - t_{asc} space which reduces the template bank to a single point in P [235]. CrossCorr typically tunes its effective coherence length T_{max} as a function of f , a_p , and t_{asc} .

7.2.6. TwoSpect algorithm

TwoSpect [236, 237] is a specialised algorithm for CW signals from neutron stars with binary companions. It starts, in a similar manner to the StackSlide-on-power method, by stacking SFT power spectra and forming a time-frequency plane of SFT frequency (in the vertical direction) versus time (in the horizontal direction). A second

series of Fourier transformations and power spectra are then computed over the time (horizontal) plane, yielding a frequency-frequency plane of SFT frequency (vertical) versus the 2nd Fourier transform frequency (horizontal); see Fig. 1 of [236]. Due to the various modulations of the CW signal from the orbits of the neutron star and Earth, signal power will appear in the TwoSpect frequency-frequency plane at regularly-spaced pixels, indicating the fundamental periods of the modulations and their harmonics. A first stage of analysis incoherently sums power in pixels and their harmonics, to identify promising candidates; a second stage then constructs templates which match the distinctive pattern of pixels expected for a CW signal with given sky, frequency, and binary orbital parameters.

TwoSpect was used to perform the first all-sky search for neutron stars in binary systems using S6 data (Table 2); to date this remains the broadest CW search ever performed (Fig. 6). TwoSpect has also been used in a directed search mode to target the LMXBs Sco X-1 and XTE J1751–305 [238].

7.2.7. Viterbi and SOAP algorithms

An HMM (Sec. 4.2.5) models the CW signal frequency as a randomly-wandering path over a time-frequency plane, as opposed to a pre-determined function. The Viterbi algorithm is used to recover the most likely path of the signal frequency through the plane.

The effect of the Viterbi algorithm is often described as “tracking” the signal (forward) in time. This is somewhat misleading, as in fact the Viterbi algorithm works by looking *backwards* in time. As implemented for CW searches [184, 239–242], the Viterbi algorithm operates as follows. For each time step m and frequency bin n , it considers the frequency bins $n - \delta n_-, n - \delta n_- + 1, \dots, n + \delta n_+$ from the previous time step $m - 1$. Here $\delta n_-, \delta n_+ \geq 0$ are chosen based on the expected properties of the CW frequency, e.g. whether it may decrease ($\delta n_- > 0$) or increase ($\delta n_+ > 0$) with time. Based on the detection statistics computed at these $\delta n = 1 + \delta n_- + \delta n_+$ frequency bins, the Viterbi algorithm chooses the bin with the maximum detection statistic. This indicates the most likely path from time step $m - 1$ to time step m which ends at bin n , out of the δn possibilities. The maximum detection statistic at time step $m - 1$ is then added to the detection statistic computed at the current time step m and frequency bin n . In short, at every time step m , the Viterbi algorithm finds the N most probable past paths of the CW frequency that intersect the N frequency bins. At the final time step $M - 1$, the Viterbi algorithm has found the N most probable paths of the CW frequency through the time-frequency plane that end at the N frequency bins.

The Viterbi algorithm has many advantages, including low computational cost, effective coverage of a vast space of possible signal frequency variations (see Sec. 4.2.5), and straightforward adaptability to a wide variety of search targets. The first implementation of the algorithm for CW searches [184, 239] targeted LMXBs such as Sco X-1 where,

in contrast to templated CW algorithms, the Viterbi algorithm could robustly handle the expected spin wandering of the signal frequency due to the time-varying accretion torque. The same implementation has since been applied to CCOs in young supernova remnants [240] and long-duration transient gravitational waves from a neutron star born in a binary neutron star merger [243].

A variant of the algorithm, SOAP [242], augments the basic Viterbi algorithm with a memory – where the algorithm looks back several time steps instead of just one – to better tune the search toward periodic-like signals. A post-processing step using convolutional neural networks [244] is added to improve robustness towards spectral artefacts. SOAP is intended as a general-purpose, “quick-look” search method for CW signals, as well as a tool for identifying instrumental line artefacts.

7.3. Other algorithms and applications

CW searches over wide parameter spaces typically yield a large number of candidate signals. Post-processing of these candidates may require: a robust determination of their significance, but determining the statistical distribution expected for the maximum detection statistic [245–247]; clustering of candidates with similar parameters [248–254]; vetoing of candidates due to instrumental artefacts [255–257] or use of statistics insensitive to such artefacts [258–261]; and the performance of successive follow-up searches with increasing coherence times to sieve out the most significant candidates [165, 262–266].

Recently there has been interest in addressing the challenges of CW searches using deep learning techniques [267–270], and by engaging expertise from beyond academia through competitive challenges [271]. In anticipation of a first CW detection, there is also growing interest in quantifying what knowledge of neutron star physics we might be able to learn [272–275].

8. Summary

Significant challenges stand in the way of making a first detection of CWs from neutron stars: the very weak nature of the signal compared to contemporary detector sensitivities, the vast breadth of the parameter space in which it may exist, and severe computational prohibitions on using the optimal analysis method. In this review we have seen that, in response to these challenges, CW data analysts have applied a wide variety of algorithms, each with different strengths and compromises, and performed a diverse number of searches of LIGO and Virgo detector data encompassing broad swathes of parameter space.

The field of CW data analysis has developed considerably in the last twenty years. Continued refinement of algorithms and search designs, combined with ever-more sensitive detectors, may one day pay off in the initial thrill of a first detection, followed by a unique and enduring perspective on the extreme physics of neutron stars. Let us hope that Nature is so kind.

Further reading. There are a growing number of informative review articles covering different aspects of CW research. In addition to this review, the reader is encouraged to consult: [276–279] for reviews of CW sources and astrophysics; [210, 280, 281] for reviews with a focus on CW searches and statistical techniques; and [282–286] for broad overviews of CW sources, algorithms, and results.

Acknowledgements

I thank Pep Covas, Paola Leaci, Andrew Miller, Ben Owen, Matt Pitkin, and Keith Riles for helpful comments on the manuscript. The author is supported by the Australian Research Council Centre of Excellence for Gravitational Wave Discovery (OzGrav), project number CE170100004. This manuscript was prepared using the following software: Adobe Convert PDF to Excel [287], Astropy [288], graphreader.com [289], Jupyter [290], Mathematica [291], and Numpy [292]. This manuscript has document number LIGO-P2300131-v4.

References

- [1] D. Kennefick, Einstein Versus the Physical Review, *Physics Today* 58 (2005) 43. doi:10.1063/1.2117822.
- [2] A. Einstein, Näherungsweise Integration der Feldgleichungen der Gravitation, *Sitzungsberichte der Königlich Preußischen Akademie der Wissenschaften* 1 (1916) 688. URL <https://ui.adsabs.harvard.edu/abs/1916SPAW.....688E>
- [3] A. Einstein, Über Gravitationswellen, *Sitzungsberichte der Königlich Preußischen Akademie der Wissenschaften* 1 (1918) 154. URL <https://ui.adsabs.harvard.edu/abs/1918SPAW.....154E>
- [4] B. P. Abbott, et al., Observation of Gravitational Waves from a Binary Black Hole Merger, *Physical Review Letters* 116 (2016) 061102. doi:10.1103/PhysRevLett.116.061102.
- [5] A. Einstein, N. Rosen, On gravitational waves, *Journal of the Franklin Institute* 223 (1937) 43. doi:10.1016/S0016-0032(37)90583-0.
- [6] B. P. Abbott, et al., Binary Black Hole Mergers in the First Advanced LIGO Observing Run, *Physical Review X* 6 (2016) 041015. doi:10.1103/PhysRevX.6.041015.
- [7] B. P. Abbott, et al., GW170817: Observation of Gravitational Waves from a Binary Neutron Star Inspiral, *Physical Review Letters* 119 (2017) 161101. doi:10.1103/PhysRevLett.119.161101.
- [8] B. P. Abbott, et al., GWTC-1: A Gravitational-Wave Transient Catalog of Compact Binary Mergers Observed by LIGO and Virgo during the First and Second Observing Runs, *Physical Review X* 9 (2019) 031040. doi:10.1103/PhysRevX.9.031040.
- [9] R. Abbott, et al., GWTC-2: Compact Binary Coalescences Observed by LIGO and Virgo during the First Half of the Third Observing Run, *Physical Review X* 11 (2021) 021053. doi:10.1103/PhysRevX.11.021053.
- [10] R. Abbott, et al., GWTC-3: Compact Binary Coalescences Observed by LIGO and Virgo During the Second Part of the Third Observing Run, submitted (2021). arXiv:2111.03606.
- [11] J. Aasi, et al., Advanced LIGO, Classical and Quantum Gravity 32 (2015) 074001. doi:10.1088/0264-9381/32/7/074001.
- [12] F. Acernese, et al., Advanced Virgo: a second-generation interferometric gravitational wave detector, *Classical and Quantum Gravity* 32 (2015) 024001. doi:10.1088/0264-9381/32/2/024001.

- [13] B. P. Abbott, et al., Multi-messenger Observations of a Binary Neutron Star Merger, *Astrophysical Journal Letters* 848 (2017) L12. doi:10.3847/2041-8213/aa91c9.
- [14] B. P. Abbott, et al., Binary Black Hole Population Properties Inferred from the First and Second Observing Runs of Advanced LIGO and Advanced Virgo, *Astrophysical Journal Letters* 882 (2019) L24. doi:10.3847/2041-8213/ab3800.
- [15] R. Abbott, et al., Population Properties of Compact Objects from the Second LIGO-Virgo Gravitational-Wave Transient Catalog, *Astrophysical Journal Letters* 913 (2021) L7. doi:10.3847/2041-8213/abe949.
- [16] B. P. Abbott, et al., A gravitational-wave standard siren measurement of the Hubble constant, *Nature* 551 (2017) 85. doi:10.1038/nature24471.
- [17] M. Soares-Santos, et al., First Measurement of the Hubble Constant from a Dark Standard Siren using the Dark Energy Survey Galaxies and the LIGO/Virgo Binary-Black-hole Merger GW170814, *Astrophysical Journal Letters* 876 (2019) L7. doi:10.3847/2041-8213/ab14f1.
- [18] B. P. Abbott, et al., A Gravitational-wave Measurement of the Hubble Constant Following the Second Observing Run of Advanced LIGO and Virgo, *Astrophysical Journal* 909 (2021) 218. doi:10.3847/1538-4357/abdc7.
- [19] M. Ruderman, Neutron Starquakes and Pulsar Periods, *Nature* 223 (1969) 597. doi:10.1038/223597b0.
- [20] C. J. Horowitz, K. Kadau, Breaking Strain of Neutron Star Crust and Gravitational Waves, *Physical Review Letters* 102 (2009) 191102. doi:10.1103/PhysRevLett.102.191102.
- [21] A. Reisenegger, Magnetic Fields of Neutron Stars: an Overview, in: G. Mathys, S. K. Solanki, D. T. Wickramasinghe (Eds.), *Magnetic Fields Across the Hertzsprung-Russell Diagram*, Vol. 248 of *Astronomical Society of the Pacific Conference Series*, 2001, p. 469.
- [22] S. Bonazzola, E. Gourgoulhon, Gravitational waves from pulsars: emission by the magnetic field induced distortion, *Astronomy & Astrophysics* 312 (1996) 675.
- [23] P. Jaranowski, A. Królak, B. F. Schutz, Data analysis of gravitational-wave signals from spinning neutron stars: The signal and its detection, *Physical Review D* 58 (1998) 063001. doi:10.1103/PhysRevD.58.063001.
- [24] L. Lindblom, B. J. Owen, S. M. Morsink, Gravitational Radiation Instability in Hot Young Neutron Stars, *Physical Review Letters* 80 (1998) 4843. doi:10.1103/PhysRevLett.80.4843.
- [25] J. A. Wheeler, Superdense Stars, *Annual Review of Astronomy and Astrophysics* 4 (1966) 393. doi:10.1146/annurev.aa.04.090166.002141.
- [26] W.-Y. Chau, Gravitational Radiation from Neutron Stars, *Astrophysical Journal* 147 (1967) 664. doi:10.1086/149042.
- [27] J. P. Ostriker, J. E. Gunn, On the Nature of Pulsars. I. Theory, *Astrophysical Journal* 157 (1969) 1395. doi:10.1086/150160.
- [28] D. I. Jones, Gravitational wave emission from rotating superfluid neutron stars, *Monthly Notices of the Royal Astronomical Society* 402 (2010) 2503. doi:10.1111/j.1365-2966.2009.16059.x.
- [29] D. I. Jones, Parameter choices and ranges for continuous gravitational wave searches for steadily spinning neutron stars, *Monthly Notices of the Royal Astronomical Society* 453 (2015) 53. doi:10.1093/mnras/stv1584.
- [30] M. Pitkin, C. Gill, D. I. Jones, G. Woan, G. S. Davies, First results and future prospects for dual-harmonic searches for gravitational waves from spinning neutron stars, *Monthly Notices of the Royal Astronomical Society* 453 (2015) 4399. arXiv:1508.00416, doi:10.1093/mnras/stv1931. URL <https://doi.org/10.1093/mnras/stv1931>
- [31] M. Bejger, A. Królak, Searching for gravitational waves from known pulsars at once and twice the spin frequency, *Classical and Quantum Gravity* 31 (2014) 105011. doi:10.1088/0264-9381/31/10/105011.
- [32] W. Y. Chau, Gravitational Radiation and the Oblique Rotator Model, *Nature* 228 (1970) 655. doi:10.1038/228655a0.
- [33] M. Zimmermann, E. Szedenis, Jr., Gravitational waves from rotating and precessing rigid bodies - Simple models and applications to pulsars, *Physical Review D* 20 (1979) 351. doi:10.1103/PhysRevD.20.351.
- [34] M. Zimmermann, Gravitational waves from rotating and precessing rigid bodies. II - General solutions and computationally useful formulas, *Physical Review D* 21 (1980) 891. doi:10.1103/PhysRevD.21.891.
- [35] R. Prix, Search for continuous gravitational waves: Metric of the multidetector \mathcal{F} -statistic, *Physical Review D* 75 (2007) 023004. doi:10.1103/PhysRevD.75.023004.
- [36] G. Ushomirsky, C. Cutler, L. Bildsten, Deformations of accreting neutron star crusts and gravitational wave emission, *Monthly Notices of the Royal Astronomical Society* 319 (2000) 902. doi:10.1046/j.1365-8711.2000.03938.x.
- [37] M. Pitkin, CW Equation Generator (2022). URL <https://pypi.org/project/cweqgen/>
- [38] J. J. Condon, S. M. Ransom, *Essential Radio Astronomy*, Princeton University Press, Princeton, 2016, Ch. 6, pp. 208–232. URL <http://www.jstor.org/stable/j.ctv5vdcww.10>
- [39] K. Wette, et al., Searching for gravitational waves from Cassiopeia A with LIGO, *Classical and Quantum Gravity* 25 (2008) 235011. doi:10.1088/0264-9381/25/23/235011.
- [40] G. Hobbs, A. G. Lyne, M. Kramer, C. E. Martin, C. Jordan, Long-term timing observations of 374 pulsars, *Monthly Notices of the Royal Astronomical Society* 353 (2004) 1311. doi:10.1111/j.1365-2966.2004.08157.x.
- [41] G. Hobbs, A. G. Lyne, M. Kramer, An analysis of the timing irregularities for 366 pulsars, *Monthly Notices of the Royal Astronomical Society* 402 (2010) 1027. doi:10.1111/j.1365-2966.2009.15938.x.
- [42] J. A. Pons, D. Viganò, U. Geppert, Pulsar timing irregularities and the imprint of magnetic field evolution, *Astronomy and Astrophysics* 547 (2012) A9. doi:10.1051/0004-6361/201220091.
- [43] S.-N. Zhang, Y. Xie, Why Do the Braking Indices of Pulsars Span a Range of More Than 100 Millions?, *Astrophysical Journal* 761 (2012) 102. doi:10.1088/0004-637X/761/2/102.
- [44] D. I. Jones, N. Andersson, Freely precessing neutron stars: model and observations, *Monthly Notices of the Royal Astronomical Society* 324 (2001) 811. doi:10.1046/j.1365-8711.2001.04251.x.
- [45] D. I. Jones, N. Andersson, Gravitational waves from freely precessing neutron stars, *Monthly Notices of the Royal Astronomical Society* 331 (2002) 203. doi:10.1046/j.1365-8711.2002.05180.x.
- [46] C. Van Den Broeck, The gravitational wave spectrum of non-axisymmetric, freely precessing neutron stars, *Classical and Quantum Gravity* 22 (2005) 1825. doi:10.1088/0264-9381/22/9/022.
- [47] K. D. Kokkotas, B. G. Schmidt, Quasi-Normal Modes of Stars and Black Holes, *Living Reviews in Relativity* 2 (1999) 2. doi:10.12942/lrr-1999-2.
- [48] N. Andersson, A New Class of Unstable Modes of Rotating Relativistic Stars, *Astrophysical Journal* 502 (1998) 708. doi:10.1086/305919.
- [49] S. Chandrasekhar, Solutions of Two Problems in the Theory of Gravitational Radiation, *Physical Review Letters* 24 (1970) 611, erratum: [293]. doi:10.1103/PhysRevLett.24.611.
- [50] J. L. Friedman, B. F. Schutz, Secular instability of rotating Newtonian stars., *Astrophysical Journal* 222 (1978) 281. doi:10.1086/156143.
- [51] D. I. Jones, The CFS instability (2013). URL <http://www.personal.soton.ac.uk/dij/cfs.html>
- [52] B. J. Owen, L. Lindblom, C. Cutler, B. F. Schutz, A. Vecchio, N. Andersson, Gravitational waves from hot young rapidly rotating neutron stars, *Physical Review D* 58 (1998) 084020. doi:10.1103/PhysRevD.58.084020.
- [53] L. Lindblom, B. J. Owen, G. Ushomirsky, Effect of a neutron-star crust on the r -mode instability, *Physical Review D* 62 (2000) 084030. doi:10.1103/PhysRevD.62.084030.

- [54] L. Bildsten, G. Ushomirsky, Viscous Boundary-Layer Damping of r -Modes in Neutron Stars, *Astrophysical Journal Letters* 529 (2000) L33. doi:10.1086/312454.
- [55] L. Rezzolla, F. K. Lamb, D. Marković, S. L. Shapiro, Properties of r modes in rotating magnetic neutron stars. I. Kinematic secular effects and magnetic evolution equations, *Physical Review D* 64 (2001) 104013. doi:10.1103/PhysRevD.64.104013.
- [56] L. Rezzolla, F. K. Lamb, D. Marković, S. L. Shapiro, Properties of r modes in rotating magnetic neutron stars. II. Evolution of the r modes and stellar magnetic field, *Physical Review D* 64 (2001) 104014. doi:10.1103/PhysRevD.64.104014.
- [57] Y. Wu, C. D. Matzner, P. Arras, r -Modes in Neutron Stars with Crusts: Turbulent Saturation, Spin-down, and Crust Melting, *Astrophysical Journal* 549 (2001) 1011. doi:10.1086/319446.
- [58] R. Bondarescu, S. A. Teukolsky, I. Wasserman, Spinning down newborn neutron stars: Nonlinear development of the r -mode instability, *Physical Review D* 79 (2009) 104003. doi:10.1103/PhysRevD.79.104003.
- [59] N. Andersson, B. Haskell, G. L. Comer, r -modes in low temperature color-flavor-locked superconducting quark stars, *Physical Review D* 82 (2010) 023007. doi:10.1103/PhysRevD.82.023007.
- [60] R. Bondarescu, I. Wasserman, Nonlinear Development of the r -mode Instability and the Maximum Rotation Rate of Neutron Stars, *Astrophysical Journal* 778 (2013) 9. doi:10.1088/0004-637X/778/1/9.
- [61] M. G. Alford, K. Schwenzer, Gravitational Wave Emission and Spin-down of Young Pulsars, *Astrophysical Journal* 781 (2014) 26. doi:10.1088/0004-637X/781/1/26.
- [62] M. G. Alford, K. Schwenzer, Gravitational wave emission from oscillating millisecond pulsars, *Monthly Notices of the Royal Astronomical Society* 446 (2015) 3631. doi:10.1093/mnras/stu2361.
- [63] J. L. Friedman, L. Lindblom, K. H. Lockitch, Differential rotation of the unstable nonlinear r -modes, *Physical Review D* 93 (2016) 024023. doi:10.1103/PhysRevD.93.024023.
- [64] B. J. Owen, How to adapt broad-band gravitational-wave searches for r -modes, *Physical Review D* 82 (2010) 104002. doi:10.1103/PhysRevD.82.104002.
- [65] A. Idrisy, B. J. Owen, D. I. Jones, R -mode frequencies of slowly rotating relativistic neutron stars with realistic equations of state, *Physical Review D* 91 (2015) 024001. doi:10.1103/PhysRevD.91.024001.
- [66] S. Caride, R. Inta, B. J. Owen, B. Rajbhandari, How to search for gravitational waves from r -modes of known pulsars, *Physical Review D* 100 (2019) 064013. doi:10.1103/PhysRevD.100.064013.
- [67] D. Bhattacharya, E. P. J. van den Heuvel, Formation and evolution of binary and millisecond radio pulsars, *Physics Reports* 203 (1991) 1. doi:10.1016/0370-1573(91)90064-S.
- [68] D. J. B. Payne, A. Melatos, Frequency Spectrum of Gravitational Radiation from Global Hydromagnetic Oscillations of a Magnetically Confined Mountain on an Accreting Neutron Star, *Astrophysical Journal* 641 (2006) 471. doi:10.1086/498855.
- [69] M. Vigelius, A. Melatos, Three-dimensional stability of magnetically confined mountains on accreting neutron stars, *Monthly Notices of the Royal Astronomical Society* 386 (2008) 1294. doi:10.1111/j.1365-2966.2008.13139.x.
- [70] M. Vigelius, A. Melatos, Improved estimate of the detectability of gravitational radiation from a magnetically confined mountain on an accreting neutron star, *Monthly Notices of the Royal Astronomical Society* 395 (2009) 1972. doi:10.1111/j.1365-2966.2009.14690.x.
- [71] M. Vigelius, A. Melatos, Resistive relaxation of a magnetically confined mountain on an accreting neutron star, *Monthly Notices of the Royal Astronomical Society* 395 (2009) 1985. doi:10.1111/j.1365-2966.2009.14698.x.
- [72] K. Wette, M. Vigelius, A. Melatos, Sinking of a magnetically confined mountain on an accreting neutron star, *Monthly Notices of the Royal Astronomical Society* 402 (2010) 1099. doi:10.1111/j.1365-2966.2009.15937.x.
- [73] M. Priymak, A. Melatos, D. J. B. Payne, Quadrupole moment of a magnetically confined mountain on an accreting neutron star: effect of the equation of state, *Monthly Notices of the Royal Astronomical Society* 417 (2011) 2696. doi:10.1111/j.1365-2966.2011.19431.x.
- [74] B. Haskell, M. Priymak, A. Patruno, M. Oppenorth, A. Melatos, P. D. Lasky, Detecting gravitational waves from mountains on neutron stars in the advanced detector era, *Monthly Notices of the Royal Astronomical Society* 450 (2015) 2393. doi:10.1093/mnras/stv726.
- [75] L. Bildsten, Gravitational Radiation and Rotation of Accreting Neutron Stars, *Astrophysical Journal Letters* 501 (1998) L89. doi:10.1086/311440.
- [76] N. Andersson, K. Glampedakis, B. Haskell, A. L. Watts, Modelling the spin equilibrium of neutron stars in low-mass X-ray binaries without gravitational radiation, *Monthly Notices of the Royal Astronomical Society* 361 (2005) 1153. doi:10.1111/j.1365-2966.2005.09167.x.
- [77] B. Haskell, A. Patruno, Spin Equilibrium with or without Gravitational Wave Emission: The Case of XTE J1814-338 and SAX J1808.4-3658, *Astrophysical Journal Letters* 738 (2011) L14. doi:10.1088/2041-8205/738/1/L14.
- [78] A. Patruno, B. Haskell, C. D'Angelo, Gravitational Waves and the Maximum Spin Frequency of Neutron Stars, *Astrophysical Journal* 746 (2012) 9. doi:10.1088/0004-637X/746/1/9.
- [79] B. Haskell, A. Patruno, Are Gravitational Waves Spinning Down PSR J1023+0038?, *Physical Review Letters* 119 (2017) 161103. doi:10.1103/PhysRevLett.119.161103.
- [80] F. Gittins, N. Andersson, Population synthesis of accreting neutron stars emitting gravitational waves, *Monthly Notices of the Royal Astronomical Society* 488 (2019) 99. doi:10.1093/mnras/stz1719.
- [81] S. Bhattacharyya, The permanent ellipticity of the neutron star in PSR J1023+0038, *Monthly Notices of the Royal Astronomical Society* 498 (2020) 728. doi:10.1093/mnras/staa2304.
- [82] W.-C. Chen, Constraining the ellipticity of millisecond pulsars with observed spin-down rates, *Physical Review D* 102 (2020) 043020. doi:10.1103/PhysRevD.102.043020.
- [83] Y. Zhang, M. A. Papa, B. Krishnan, A. L. Watts, Search for Continuous Gravitational Waves from Scorpius X-1 in LIGO O2 Data, *Astrophysical Journal Letters* 906 (2021) L14. doi:10.3847/2041-8213/abd256.
- [84] B. Abbott, et al., Searches for periodic gravitational waves from unknown isolated sources and Scorpius X-1: Results from the second LIGO science run, *Physical Review D* 76 (2007) 082001. doi:10.1103/PhysRevD.76.082001.
- [85] P. Leaci, R. Prix, Directed searches for continuous gravitational waves from binary systems: Parameter-space metrics and optimal Scorpius X-1 sensitivity, *Physical Review D* 91 (2015) 102003. doi:10.1103/PhysRevD.91.102003.
- [86] R. Abbott, et al., All-sky search for continuous gravitational waves from isolated neutron stars in the early O3 LIGO data, *Physical Review D* 104 (2021) 082004. doi:10.1103/PhysRevD.104.082004.
- [87] R. Abbott, et al., Searches for Continuous Gravitational Waves from Young Supernova Remnants in the Early Third Observing Run of Advanced LIGO and Virgo, *Astrophysical Journal* 921 (2021) 80. doi:10.3847/1538-4357/ac17ea.
- [88] R. Abbott, et al., All-sky search for continuous gravitational waves from isolated neutron stars using Advanced LIGO and Advanced Virgo O3 data, *Physical Review D* 106 (2022) 102008. doi:10.1103/PhysRevD.106.102008.
- [89] P. B. Covas, Effects of proper motion of neutron stars on continuous gravitational-wave searches, *Monthly Notices of the Royal Astronomical Society* 500 (2021) 5167. doi:10.1093/mnras/staa3624.
- [90] J. H. Taylor, J. M. Weisberg, Further experimental tests of relativistic gravity using the binary pulsar PSR 1913+16, *As-*

- trophysical Journal 345 (1989) 434. doi:10.1086/167917.
- [91] A. W. Irwin, T. Fukushima, A numerical time ephemeris of the Earth, *Astronomy and Astrophysics* 348 (1999) 642. URL <https://ui.adsabs.harvard.edu/abs/1999A&A...348..642I>
- [92] R. T. Edwards, G. B. Hobbs, R. N. Manchester, TEMPO2, a new pulsar timing package - II. The timing model and precision estimates, *Monthly Notices of the Royal Astronomical Society* 372 (2006) 1549. doi:10.1111/j.1365-2966.2006.10870.x.
- [93] K. Wette, R. Prix, Flat parameter-space metric for all-sky searches for gravitational-wave pulsars, *Physical Review D* 88 (2013) 123005. doi:10.1103/PhysRevD.88.123005.
- [94] B. P. Abbott, et al., The basic physics of the binary black hole merger GW150914, *Annalen der Physik* 529 (2017) 1600209. doi:10.1002/andp.201600209.
- [95] A. C. Searle, Monte-Carlo and Bayesian techniques in gravitational wave burst data analysis, arXiv (2008). arXiv:0804.1161. URL <https://arxiv.org/abs/0804.1161>
- [96] R. Prix, B. Krishnan, Targeted search for continuous gravitational waves: Bayesian versus maximum-likelihood statistics, *Classical and Quantum Gravity* 26 (2009) 204013. doi:10.1088/0264-9381/26/20/204013.
- [97] M. Kramer, Pulsars, in: L. I. Gurvits, S. Frey, S. Rawlings (Eds.), *EAS Publications Series*, Vol. 15 of EAS Publications Series, 2005, p. 219. doi:10.1051/eas:2005155.
- [98] B. Behnke, M. A. Papa, R. Prix, Postprocessing methods used in the search for continuous gravitational-wave signals from the Galactic Center, *Physical Review D* 91 (2015) 064007. doi:10.1103/PhysRevD.91.064007.
- [99] C. Dreissigacker, R. Prix, K. Wette, Fast and accurate sensitivity estimation for continuous-gravitational-wave searches, *Physical Review D* 98 (2018) 084058. doi:10.1103/PhysRevD.98.084058.
- [100] B. Abbott, et al., All-sky search for periodic gravitational waves in LIGO S4 data, *Physical Review D* 77 (2008) 022001, erratum: [294]. doi:10.1103/PhysRevD.77.022001.
- [101] K. Wette, Estimating the sensitivity of wide-parameter-space searches for gravitational-wave pulsars, *Physical Review D* 85 (2012) 042003. doi:10.1103/PhysRevD.85.042003.
- [102] J. Zweizig, K. Riles, Information on self-gating of $h(t)$ used in O3 continuous-wave searches, Tech. Rep. T2000384-v4, LIGO (2020). URL <https://dcc.ligo.org/LIGO-T2000384-v4/public>
- [103] B. Steltner, M. A. Papa, H.-B. Eggenstein, Identification and removal of non-Gaussian noise transients for gravitational-wave searches, *Physical Review D* 105 (2022) 022005. doi:10.1103/PhysRevD.105.022005.
- [104] B. P. Abbott, et al., All-sky search for periodic gravitational waves in the O1 LIGO data, *Physical Review D* 96 (2017) 062002. doi:10.1103/PhysRevD.96.062002.
- [105] J. T. Whelan, Bayesian Estimation of Parametrized Efficiency, Tech. Rep. G1500977-v2, LIGO (2015). URL <https://dcc.ligo.org/LIGO-G1500977-v2/public>
- [106] R. Abbott, et al., Constraints from LIGO O3 Data on Gravitational-wave Emission Due to R-modes in the Glitching Pulsar PSR J0537-6910, *Astrophysical Journal* 922 (2021) 71. doi:10.3847/1538-4357/ac0d52.
- [107] LIGO Scientific Collaboration, Strain Sensitivity of the LIGO Interferometers, S5 Performance - August 2007, Tech. Rep. G0900957-v1, LIGO (2009). URL <https://dcc.ligo.org/LIGO-G0900957-v1/public>
- [108] LIGO Scientific Collaboration, Virgo Collaboration, Sensitivity Achieved by the LIGO and Virgo Gravitational Wave Detectors during LIGO's Sixth and Virgo's Second and Third Science Runs, Tech. Rep. T1100338-v13, LIGO (2011). URL <https://dcc.ligo.org/LIGO-T1100338-v13/public>
- [109] T. Accadia, et al., Reconstruction of the gravitational wave signal $h(t)$ during the Virgo science runs and independent validation with a photon calibrator, *Classical and Quantum Gravity* 31 (2014) 165013. doi:10.1088/0264-9381/31/16/165013.
- [110] LIGO Scientific Collaboration, Virgo Collaboration, O1 Sensitivity Curves (2023). URL <https://git.ligo.org/sensitivity-curves/o1-sensitivity-curves>
- [111] LIGO Scientific Collaboration, Virgo Collaboration, Official sensitivity curves from O2 (2023). URL <https://git.ligo.org/sensitivity-curves/o2-sensitivity-curves>
- [112] LIGO Scientific Collaboration, Virgo Collaboration, O3 Sensitivity Curves (2023). URL <https://git.ligo.org/sensitivity-curves/o3-sensitivity-curves>
- [113] D. Verkindt, Sensitivity curves and BNS range for Virgo in O2 and O3, Tech. Rep. VIR-1140A-21, Virgo (2021). URL <https://tds.virgo-gw.eu/ql/?c=17389>
- [114] R. Balasubramanian, B. S. Sathyaprakash, S. V. Dhurandhar, Gravitational waves from coalescing binaries: Detection strategies and Monte Carlo estimation of parameters, *Physical Review D* 53 (1996) 3033. doi:10.1103/PhysRevD.53.3033.
- [115] B. J. Owen, Search templates for gravitational waves from inspiraling binaries: Choice of template spacing, *Physical Review D* 53 (1996) 6749. doi:10.1103/PhysRevD.53.6749.
- [116] R. Prix, Template-based searches for gravitational waves: efficient lattice covering of flat parameter spaces, *Classical and Quantum Gravity* 24 (2007) S481. doi:10.1088/0264-9381/24/19/S11.
- [117] K. Wette, Lattice template placement for coherent all-sky searches for gravitational-wave pulsars, *Physical Review D* 90 (2014) 122010. doi:10.1103/PhysRevD.90.122010.
- [118] P. R. Brady, T. Creighton, C. Cutler, B. F. Schutz, Searching for periodic sources with LIGO, *Physical Review D* 57 (1998) 2101. doi:10.1103/PhysRevD.57.2101.
- [119] D. Whitbeck, Observational Consequences of Gravitational Wave Emission From Spinning Compact Sources, Ph.D. thesis, The Pennsylvania State University (2006). URL <https://etda.libraries.psu.edu/paper/7132/>
- [120] C. Messenger, Semicoherent search strategy for known continuous wave sources in binary systems, *Physical Review D* 84 (2011) 083003. doi:10.1103/PhysRevD.84.083003.
- [121] A. Abramovici, W. E. Althouse, R. W. P. Drever, Y. Gursel, S. Kawamura, F. J. Raab, D. Shoemaker, L. Sievers, R. E. Spero, K. S. Thorne, LIGO - The Laser Interferometer Gravitational-Wave Observatory, *Science* 256 (1992) 325. doi:10.1126/science.256.5055.325.
- [122] T. Accadia, et al., Virgo: a laser interferometer to detect gravitational waves, *Journal of Instrumentation* 7 (2012) P03012. doi:10.1088/1748-0221/7/03/P03012.
- [123] B. P. Abbott, et al., LIGO: the Laser Interferometer Gravitational-Wave Observatory, *Reports on Progress in Physics* 72 (2009) 076901. doi:10.1088/0034-4885/72/7/076901.
- [124] T. Accadia, et al., Status of the Virgo project, *Classical and Quantum Gravity* 28 (2011) 114002. doi:10.1088/0264-9381/28/11/114002.
- [125] T. Akutsu, et al., Overview of KAGRA: Detector design and construction history, *Progress of Theoretical and Experimental Physics* 2021 (2021) 05A101. doi:10.1093/ptep/ptaa125.
- [126] Indian Initiative in Gravitational-wave Observations, LIGO-India: Proposal for an Interferometric Gravitational-wave Observatory, Tech. Rep. M1100296-v2, LIGO (2011). URL <https://dcc.ligo.org/LIGO-M1100296-v2/public>
- [127] H. Grote, et al., The GEO 600 status, *Classical and Quantum Gravity* 27 (2010) 084003. doi:10.1088/0264-9381/27/8/084003.
- [128] K. L. Dooley, et al., GEO 600 and the GEO-HF upgrade program: successes and challenges, *Classical and Quantum Gravity* 33 (2016) 075009. doi:10.1088/0264-9381/33/7/075009.
- [129] R. Abbott, et al., All-sky search for gravitational wave emission from scalar boson clouds around spinning black holes in LIGO O3 data, *Physical Review D* 105 (2022) 102001. doi:10.1103/PhysRevD.105.102001.

- [130] R. Abbott, et al., Constraints on dark photon dark matter using data from LIGO's and Virgo's third observing run, *Physical Review D* 105 (2022) 063030. doi:10.1103/PhysRevD.105.063030.
- [131] R. Abbott, et al., Search for anisotropic gravitational-wave backgrounds using data from Advanced LIGO and Advanced Virgo's first three observing runs, *Physical Review D* 104 (2021) 022005. doi:10.1103/PhysRevD.104.022005.
- [132] R. Abbott, et al., All-sky, all-frequency directional search for persistent gravitational waves from Advanced LIGO's and Advanced Virgo's first three observing runs, *Physical Review D* 105 (2022) 122001. doi:10.1103/PhysRevD.105.122001.
- [133] R. Abbott, et al., Searches for Gravitational Waves from Known Pulsars at Two Harmonics in the Second and Third LIGO-Virgo Observing Runs, *Astrophysical Journal* 935 (2022) 1. doi:10.3847/1538-4357/ac6acf.
- [134] R. Abbott, et al., Gravitational-wave Constraints on the Equatorial Ellipticity of Millisecond Pulsars, *Astrophysical Journal Letters* 902 (2020) L21. doi:10.3847/2041-8213/abb655.
- [135] R. Abbott, et al., Diving below the Spin-down Limit: Constraints on Gravitational Waves from the Energetic Young Pulsar PSR J0537-6910, *Astrophysical Journal Letters* 913 (2021) L27. doi:10.3847/2041-8213/abffcd.
- [136] R. Abbott, et al., Narrowband Searches for Continuous and Long-duration Transient Gravitational Waves from Known Pulsars in the LIGO-Virgo Third Observing Run, *Astrophysical Journal* 932 (2022) 133. doi:10.3847/1538-4357/ac6ad0.
- [137] R. Abbott, et al., Search of the early O3 LIGO data for continuous gravitational waves from the Cassiopeia A and Vela Jr. supernova remnants, *Physical Review D* 105 (2022) 082005. doi:10.1103/PhysRevD.105.082005.
- [138] R. Abbott, et al., Search for gravitational waves from Scorpius X-1 with a hidden Markov model in O3 LIGO data, *Physical Review D* 106 (2022) 062002. doi:10.1103/PhysRevD.106.062002.
- [139] R. Abbott, et al., Model-based Cross-correlation Search for Gravitational Waves from the Low-mass X-Ray Binary Scorpius X-1 in LIGO O3 Data, *Astrophysical Journal Letters* 941 (2022) L30. doi:10.3847/2041-8213/aca1b0.
- [140] S. Galadage, K. Wette, D. K. Galloway, C. Messenger, Deep searches for X-ray pulsations from Scorpius X-1 and Cygnus X-2 in support of continuous gravitational wave searches, *Monthly Notices of the Royal Astronomical Society* 509 (2022) 1745. doi:10.1093/mnras/stab3095.
- [141] R. Abbott, et al., Search for continuous gravitational waves from 20 accreting millisecond x-ray pulsars in O3 LIGO data, *Physical Review D* 105 (2022) 022002. doi:10.1103/PhysRevD.105.022002.
- [142] A. Mukherjee, C. Messenger, K. Riles, Accretion-induced spin-wandering effects on the neutron star in Scorpius X-1: Implications for continuous gravitational wave searches, *Physical Review D* 97 (2018) 043016. doi:10.1103/PhysRevD.97.043016.
- [143] J. Chennamangalam, D. R. Lorimer, The Galactic Centre pulsar population, *Monthly Notices of the Royal Astronomical Society* 440 (2014) L86. doi:10.1093/mnras/1slu025.
- [144] R. Abbott, et al., Search for continuous gravitational wave emission from the Milky Way center in O3 LIGO-Virgo data, *Physical Review D* 106 (2022) 042003. doi:10.1103/PhysRevD.106.042003.
- [145] N. Sartore, E. Ripamonti, A. Treves, R. Turolla, Galactic neutron stars. I. Space and velocity distributions in the disk and in the halo, *Astronomy and Astrophysics* 510 (2010) A23. doi:10.1051/0004-6361/200912222.
- [146] R. N. Manchester, G. B. Hobbs, A. Teoh, M. Hobbs, The Australia Telescope National Facility Pulsar Catalogue, *Astronomical Journal* 129 (2005) 1993. doi:10.1086/428488.
- [147] C. Palomba, Simulation of a population of isolated neutron stars evolving through the emission of gravitational waves, *Monthly Notices of the Royal Astronomical Society* 359 (2005) 1150. doi:10.1111/j.1365-2966.2005.08975.x.
- [148] B. Knispel, B. Allen, Blandford's argument: The strongest continuous gravitational wave signal, *Physical Review D* 78 (2008) 044031. doi:10.1103/PhysRevD.78.044031.
- [149] L. Wade, X. Siemens, D. L. Kaplan, B. Knispel, B. Allen, Continuous gravitational waves from isolated Galactic neutron stars in the advanced detector era, *Physical Review D* 86 (2012) 124011. doi:10.1103/PhysRevD.86.124011.
- [150] M. Cieřlar, T. Bulik, M. Curyło, M. Sieniawska, N. Singh, M. Bejger, Detectability of continuous gravitational waves from isolated neutron stars in the Milky Way. The population synthesis approach, *Astronomy and Astrophysics* 649 (2021) A92. doi:10.1051/0004-6361/202039503.
- [151] R. Abbott, et al., All-sky search in early O3 LIGO data for continuous gravitational-wave signals from unknown neutron stars in binary systems, *Physical Review D* 103 (2021) 064017. doi:10.1103/PhysRevD.103.064017.
- [152] P. B. Covas, M. A. Papa, R. Prix, B. J. Owen, Constraints on r-modes and Mountains on Millisecond Neutron Stars in Binary Systems, *Astrophysical Journal Letters* 929 (2022) L19. doi:10.3847/2041-8213/ac62d7.
- [153] D. K. Galloway, S. Premachandra, D. Steeghs, T. Marsh, J. Casares, R. Cornelisse, Precision Ephemerides for Gravitational-wave Searches. I. Sco X-1, *Astrophysical Journal* 781 (2014) 14. doi:10.1088/0004-637X/781/1/14.
- [154] S. S. Premachandra, D. K. Galloway, J. Casares, D. T. Steeghs, T. R. Marsh, Precision Ephemerides for Gravitational Wave Searches. II. Cyg X-2, *Astrophysical Journal* 823 (2016) 106. doi:10.3847/0004-637X/823/2/106.
- [155] L. Wang, D. Steeghs, D. K. Galloway, T. Marsh, J. Casares, Precision Ephemerides for Gravitational-wave Searches - III. Revised system parameters of Sco X-1, *Monthly Notices of the Royal Astronomical Society* 478 (2018) 5174. doi:10.1093/mnras/sty1441.
- [156] T. L. Killestein, M. Mould, D. Steeghs, J. Casares, D. K. Galloway, J. T. Whelan, Precision Ephemerides for Gravitational-wave Searches - IV. Corrected and refined ephemeris for Scorpius X-1, *Monthly Notices of the Royal Astronomical Society* 520 (2023) 5317. doi:10.1093/mnras/stad366.
- [157] B. Rajbhandari, B. J. Owen, S. Caride, R. Inta, First searches for gravitational waves from r-modes of the Crab pulsar, *Physical Review D* 104 (2021) 122008. doi:10.1103/PhysRevD.104.122008.
- [158] L. Fesik, M. A. Papa, First Search for r-mode Gravitational Waves from PSR J0537-6910, *Astrophysical Journal* 895 (2020) 11, erratum: [295]. doi:10.3847/1538-4357/ab8193.
- [159] N. Andersson, D. Antonopoulou, C. M. Espinoza, B. Haskell, W. C. G. Ho, The Enigmatic Spin Evolution of PSR J0537-6910: r-modes, Gravitational Waves, and the Case for Continued Timing, *Astrophysical Journal* 864 (2018) 137. doi:10.3847/1538-4357/aad6eb.
- [160] W. C. G. Ho, C. M. Espinoza, Z. Arzoumanian, T. Enoto, T. Tamba, D. Antonopoulou, M. Bejger, S. Guillot, B. Haskell, P. S. Ray, Return of the Big Glitcher: NICER timing and glitches of PSR J0537-6910, *Monthly Notices of the Royal Astronomical Society* 498 (2020) 4605. doi:10.1093/mnras/staa2640.
- [161] R. Prix, Characterizing timing and memory-requirements of the \mathcal{F} -statistic implementations in LALSuite, Tech. Rep. T1600531-v4, LIGO (2017). URL <https://dcc.ligo.org/LIGO-T1600531-v4/public>
- [162] B. F. Schutz, M. A. Papa, End-to-end algorithm for hierarchical area searches for long-duration GW sources for GEO 600, in: J. Trn Thanh Vn, J. Dumarchez, S. Reynaud, C. Salomon, S. Thorsett, J. Vinet (Eds.), 34th Rencontres de Moriond: Gravitational Waves and Experimental Gravity, World Publishers, Hanoi, 1999, p. 199. arXiv:gr-qc/9905018.
- [163] P. R. Brady, T. Creighton, Searching for periodic sources with LIGO. II. Hierarchical searches, *Physical Review D* 61 (2000) 082001. doi:10.1103/PhysRevD.61.082001.
- [164] R. Prix, M. Shaltev, Search for continuous gravitational waves: Optimal StackSlide method at fixed computing cost, *Physical Review D* 85 (2012) 084010. doi:10.1103/PhysRevD.85.

084010.

- [165] C. Cutler, I. Gholami, B. Krishnan, Improved stack-slide searches for gravitational-wave pulsars, *Physical Review D* 72 (2005) 042004. doi:10.1103/PhysRevD.72.042004.
- [166] P. B. Covas, et al., Identification and mitigation of narrow spectral artifacts that degrade searches for persistent gravitational waves in the first two observing runs of Advanced LIGO, *Physical Review D* 97 (2018) 082002. doi:10.1103/PhysRevD.97.082002.
- [167] LIGO Scientific Collaboration, LIGO Algorithm Library - LALSuite, Free software (GPL) (2018). doi:10.7935/GT1W-FZ16.
- [168] B. Allen, E. Goetz, D. Keitel, M. Landry, G. Mendell, R. Prix, K. Riles, K. Wette, SFT Data Format Version 2–3 Specification, Tech. Rep. T040164-v2, LIGO (2022). URL <https://dcc.ligo.org/LIGO-T040164-v2/public>
- [169] P. Astone, S. Frasca, C. Palomba, The short FFT database and the peak map for the hierarchical search of periodic sources, *Classical and Quantum Gravity* 22 (2005) S1197. doi:10.1088/0264-9381/22/18/S34.
- [170] P. Astone, S. D’Antonio, S. Frasca, C. Palomba, A method for detection of known sources of continuous gravitational wave signals in non-stationary data, *Classical and Quantum Gravity* 27 (2010) 194016. doi:10.1088/0264-9381/27/19/194016.
- [171] P. Astone, A. Colla, S. D’Antonio, S. Frasca, C. Palomba, Coherent search of continuous gravitational wave signals: extension of the 5-vectors method to a network of detectors, in: 9th Edoardo Amaldi Conference on Gravitational Waves and 2011 Numerical Relativity–Data Analysis Meeting, Vol. 363 of *Journal of Physics Conference Series*, 2012, p. 012038. doi:10.1088/1742-6596/363/1/012038.
- [172] O. J. Piccinni, P. Astone, S. D’Antonio, S. Frasca, G. Intini, P. Leaci, S. Mastrogiovanni, A. Miller, C. Palomba, A. Singhal, A new data analysis framework for the search of continuous gravitational wave signals, *Classical and Quantum Gravity* 36 (2019) 015008. doi:10.1088/1361-6382/aaefb5.
- [173] A. Singhal, P. Leaci, P. Astone, S. D’Antonio, S. Frasca, G. Intini, I. La Rosa, S. Mastrogiovanni, A. Miller, F. Muciaccia, C. Palomba, O. Piccinni, A resampling algorithm to detect continuous gravitational-wave signals from neutron stars in binary systems, *Classical and Quantum Gravity* 36 (2019) 205015. doi:10.1088/1361-6382/ab4367.
- [174] P. Jaranowski, A. Królak, Data analysis of gravitational-wave signals from spinning neutron stars. II. Accuracy of estimation of parameters, *Physical Review D* 59 (1999) 063003. doi:10.1103/PhysRevD.59.063003.
- [175] P. Jaranowski, A. Królak, Data analysis of gravitational-wave signals from spinning neutron stars. III. Detection statistics and computational requirements, *Physical Review D* 61 (2000) 062001. doi:10.1103/PhysRevD.61.062001.
- [176] P. Astone, K. M. Borkowski, P. Jaranowski, A. Królak, Data analysis of gravitational-wave signals from spinning neutron stars. IV. An all-sky search, *Physical Review D* 65 (2002) 042003. doi:10.1103/PhysRevD.65.042003.
- [177] P. Astone, K. M. Borkowski, P. Jaranowski, M. Pietka, A. Królak, Data analysis of gravitational-wave signals from spinning neutron stars. V. A narrow-band all-sky search, *Physical Review D* 82 (2010) 022005. doi:10.1103/PhysRevD.82.022005.
- [178] G. Poghosyan, S. Matta, A. Streit, M. Bejger, A. Królak, Architecture, implementation and parallelization of the software to search for periodic gravitational wave signals, *Computer Physics Communications* 188 (2015) 167. doi:10.1016/j.cpc.2014.10.025.
- [179] P. Patel, X. Siemens, R. Dupuis, J. Betzwieser, Implementation of barycentric resampling for continuous wave searches in gravitational wave data, *Physical Review D* 81 (2010) 084032. doi:10.1103/PhysRevD.81.084032.
- [180] R. Prix, Resampling FFT-based implementation of the \mathcal{F} -statistic, Tech. Rep. T1600531-v3, LIGO (2017). URL <https://dcc.ligo.org/LIGO-T1600531-v3/public>
- [181] L. Dunn, P. Clearwater, A. Melatos, K. Wette, Graphics processing unit implementation of the \mathcal{F} -statistic for continuous gravitational wave searches, *Classical and Quantum Gravity* 39 (2022) 045003. doi:10.1088/1361-6382/ac4616.
- [182] P. R. Williams, B. F. Schutz, An efficient matched filtering algorithm for the detection of continuous gravitational wave signals, in: S. Meshkov (Ed.), *AIP Conference Series*, Vol. 523, American Institute of Physics, Melville, 2000, p. 473. doi:10.1063/1.1291918.
- [183] R. Prix, The \mathcal{F} -statistic and its implementation in ComputeF-statistic_v2, Tech. Rep. T0900149-v6, LIGO (2018). URL <https://dcc.ligo.org/LIGO-T0900149-v6/public>
- [184] S. Suvorova, P. Clearwater, A. Melatos, L. Sun, W. Moran, R. J. Evans, Hidden Markov model tracking of continuous gravitational waves from a binary neutron star with wandering spin. II. Binary orbital phase tracking, *Physical Review D* 96 (2017) 102006. doi:10.1103/PhysRevD.96.102006.
- [185] L. Sammut, C. Messenger, A. Melatos, B. J. Owen, Implementation of the frequency-modulated sideband search method for gravitational waves from low mass x-ray binaries, *Physical Review D* 89 (2014) 043001. doi:10.1103/PhysRevD.89.043001.
- [186] G. B. Hobbs, R. T. Edwards, R. N. Manchester, TEMPO2, a new pulsar-timing package - I. An overview, *Monthly Notices of the Royal Astronomical Society* 369 (2006) 655. doi:10.1111/j.1365-2966.2006.10302.x.
- [187] M. Pitkin, G. Woan, Searching for gravitational waves from the Crab pulsar — the problem of timing noise, *Classical and Quantum Gravity* 21 (2004) 843. doi:10.1088/0264-9381/21/5/069.
- [188] M. Pitkin, G. Woan, Binary system delays and timing noise in searches for gravitational waves from known pulsars, *Physical Review D* 76 (2007) 042006. doi:10.1103/PhysRevD.76.042006.
- [189] R. J. Dupuis, G. Woan, Bayesian estimation of pulsar parameters from gravitational wave data, *Physical Review D* 72 (2005) 102002. doi:10.1103/PhysRevD.72.102002.
- [190] M. Pitkin, M. Isi, J. Veitch, G. Woan, A nested sampling code for targeted searches for continuous gravitational waves from pulsars, *arXiv* (2017). arXiv:1705.08978. URL <https://arxiv.org/abs/1705.08978>
- [191] J. Skilling, Nested sampling for general Bayesian computation, *Bayesian Analysis* 1 (2006) 833. doi:10.1214/06-BA127.
- [192] M. Isi, M. Pitkin, A. J. Weinstein, Probing dynamical gravity with the polarization of continuous gravitational waves, *Physical Review D* 96 (2017) 042001. doi:10.1103/PhysRevD.96.042001.
- [193] M. Pitkin, CWInPy: A Python package for inference with continuous gravitational-wave signals from pulsars, *Journal of Open Source Software* 7 (2022) 4568. doi:10.21105/joss.04568.
- [194] G. Ashton, et al., BILBY: A User-friendly Bayesian Inference Library for Gravitational-wave Astronomy, *Astrophysical Journal Supplement* 241 (2019) 27. doi:10.3847/1538-4365/ab06fc.
- [195] B. Abbott, et al., Einstein@Home search for periodic gravitational waves in LIGO S4 data, *Physical Review D* 79 (2009) 022001. doi:10.1103/PhysRevD.79.022001.
- [196] P. V. C. Hough, Machine Analysis of Bubble Chamber Pictures, in: L. Kowarski (Ed.), *2nd International Conference on High-Energy Accelerators and Instrumentation*, Vol. C590914, CERN, Geneva, 1959, p. 554.
- [197] B. Krishnan, A. M. Sintes, M. A. Papa, B. F. Schutz, S. Frasca, C. Palomba, Hough transform search for continuous gravitational waves, *Physical Review D* 70 (2004) 082001. doi:10.1103/PhysRevD.70.082001.
- [198] B. Krishnan, LIGO Scientific Collaboration, Wide parameter search for isolated pulsars using the Hough transform, *Classical and Quantum Gravity* 22 (2005) S1265. doi:10.1088/0264-9381/22/18/S40.
- [199] F. Antonucci, P. Astone, S. D’Antonio, S. Frasca, C. Palomba, Detection of periodic gravitational wave sources by Hough

- transform in the f versus $f\text{-dot}$ plane, *Classical and Quantum Gravity* 25 (2008) 184015. doi:10.1088/0264-9381/25/18/184015.
- [200] P. Astone, A. Colla, S. D'Antonio, S. Frasca, C. Palomba, Method for all-sky searches of continuous gravitational wave signals using the frequency-Hough transform, *Physical Review D* 90 (2014) 042002. doi:10.1103/PhysRevD.90.042002.
- [201] J. Aasi, et al., Einstein@Home all-sky search for periodic gravitational waves in LIGO S5 data, *Physical Review D* 87 (2013) 042001. doi:10.1103/PhysRevD.87.042001.
- [202] C. Palomba, P. Astone, S. Frasca, Adaptive Hough transform for the search of periodic sources, *Classical and Quantum Gravity* 22 (2005) S1255. doi:10.1088/0264-9381/22/18/S39.
- [203] B. Krishnan, A. M. Sintes, Hough search with improved sensitivity, Tech. Rep. T070124-x0, LIGO (2007). URL <https://dcc.ligo.org/LIGO-T070124-x0/public>
- [204] P. B. Covas, A. M. Sintes, New method to search for continuous gravitational waves from unknown neutron stars in binary systems, *Physical Review D* 99 (2019) 124019. doi:10.1103/PhysRevD.99.124019.
- [205] O. J. Piccinni, P. Astone, S. D'Antonio, S. Frasca, G. Intini, I. La Rosa, P. Leaci, S. Mastrogiovanni, A. Miller, C. Palomba, Directed search for continuous gravitational-wave signals from the Galactic Center in the Advanced LIGO second observing run, *Physical Review D* 101 (2020) 082004. doi:10.1103/PhysRevD.101.082004.
- [206] P. Leaci, P. Astone, S. D'Antonio, S. Frasca, C. Palomba, O. Piccinni, S. Mastrogiovanni, Novel directed search strategy to detect continuous gravitational waves from neutron stars in low- and high-eccentricity binary systems, *Physical Review D* 95 (2017) 122001. doi:10.1103/PhysRevD.95.122001.
- [207] A. Miller, P. Astone, S. D'Antonio, S. Frasca, G. Intini, I. La Rosa, P. Leaci, S. Mastrogiovanni, F. Muciaccia, C. Palomba, O. J. Piccinni, A. Singhal, B. F. Whiting, Method to search for long duration gravitational wave transients from isolated neutron stars using the generalized frequency-Hough transform, *Physical Review D* 98 (2018) 102004. doi:10.1103/PhysRevD.98.102004.
- [208] M. Oliver, D. Keitel, A. M. Sintes, Adaptive transient Hough method for long-duration gravitational wave transients, *Physical Review D* 99 (2019) 104067. doi:10.1103/PhysRevD.99.104067.
- [209] G. Mendell, M. Landry, StackSlide and Hough Search SNR and Statistics, Tech. Rep. T050003-x0, LIGO (2005). URL <https://dcc.ligo.org/LIGO-T050003-x0/public>
- [210] P. Jaranowski, A. Królak, Gravitational-Wave Data Analysis. Formalism and Sample Applications: The Gaussian Case, *Living Reviews in Relativity* 8 (2005) 3. doi:10.12942/lrr-2005-3.
- [211] B. Allen, Optimal template banks, *Physical Review D* 104 (2021) 042005. doi:10.1103/PhysRevD.104.042005.
- [212] B. Allen, A. A. Shoom, Template banks based on Z^n and A_n^* lattices, *Physical Review D* 104 (2021) 122007. doi:10.1103/PhysRevD.104.122007.
- [213] K. Wette, Empirically extending the range of validity of parameter-space metrics for all-sky searches for gravitational-wave pulsars, *Physical Review D* 94 (2016) 122002. doi:10.1103/PhysRevD.94.122002.
- [214] B. Allen, Spherical ansatz for parameter-space metrics, *Physical Review D* 100 (2019) 124004. doi:10.1103/PhysRevD.100.124004.
- [215] R. Prix, Y. Itoh, Global parameter-space correlations of coherent searches for continuous gravitational waves, *Classical and Quantum Gravity* 22 (2005) S1003. doi:10.1088/0264-9381/22/18/S14.
- [216] H. J. Pletsch, Parameter-space correlations of the optimal statistic for continuous gravitational-wave detection, *Physical Review D* 78 (2008) 102005. doi:10.1103/PhysRevD.78.102005.
- [217] H. J. Pletsch, B. Allen, Exploiting Large-Scale Correlations to Detect Continuous Gravitational Waves, *Physical Review Letters* 103 (2009) 181102. doi:10.1103/PhysRevLett.103.181102.
- [218] H. J. Pletsch, Parameter-space metric of semicoherent searches for continuous gravitational waves, *Physical Review D* 82 (2010) 042002. doi:10.1103/PhysRevD.82.042002.
- [219] K. Wette, Parameter-space metric for all-sky semicoherent searches for gravitational-wave pulsars, *Physical Review D* 92 (2015) 082003. doi:10.1103/PhysRevD.92.082003.
- [220] K. Wette, S. Walsh, R. Prix, M. A. Papa, Implementing a semicoherent search for continuous gravitational waves using optimally constructed template banks, *Physical Review D* 97 (2018) 123016. doi:10.1103/PhysRevD.97.123016.
- [221] S. Walsh, K. Wette, M. A. Papa, R. Prix, Optimizing the choice of analysis method for all-sky searches for continuous gravitational waves with Einstein@Home, *Physical Review D* 99 (2019) 082004. doi:10.1103/PhysRevD.99.082004.
- [222] V. Dergachev, Description of PowerFlux algorithms and implementation, Tech. Rep. T050186-x0, LIGO (2005). URL <https://dcc.ligo.org/LIGO-T050186-x0/public>
- [223] V. Dergachev, Description of PowerFlux 2 algorithms and implementation, Tech. Rep. T1000272-v5, LIGO (2011). URL <https://dcc.ligo.org/LIGO-T1000272-v5/public>
- [224] V. Dergachev, Novel universal statistic for computing upper limits in an ill-behaved background, *Physical Review D* 87 (2013) 062001. doi:10.1103/PhysRevD.87.062001.
- [225] V. Dergachev, On blind searches for noise dominated signals: a loosely coherent approach, *Classical and Quantum Gravity* 27 (2010) 205017. doi:10.1088/0264-9381/27/20/205017.
- [226] V. Dergachev, Loosely coherent searches for sets of well-modeled signals, *Physical Review D* 85 (2012) 062003. doi:10.1103/PhysRevD.85.062003.
- [227] H. J. Pletsch, Sliding coherence window technique for hierarchical detection of continuous gravitational waves, *Physical Review D* 83 (2011) 122003. doi:10.1103/PhysRevD.83.122003.
- [228] C. Cutler, An improved, "phase-relaxed" \mathcal{F} -statistic for gravitational-wave data analysis, *Physical Review D* 86 (2012) 063012. doi:10.1103/PhysRevD.86.063012.
- [229] V. Dergachev, M. A. Papa, Sensitivity Improvements in the Search for Periodic Gravitational Waves Using O1 LIGO Data, *Physical Review Letters* 123 (2019) 101101. doi:10.1103/PhysRevLett.123.101101.
- [230] S. W. Ballmer, A radiometer for stochastic gravitational waves, *Classical and Quantum Gravity* 23 (2006) 179. doi:10.1088/0264-9381/23/8/S23.
- [231] S. Dhurandhar, B. Krishnan, H. Mukhopadhyay, J. T. Whelan, Cross-correlation search for periodic gravitational waves, *Physical Review D* 77 (2008) 082001. doi:10.1103/PhysRevD.77.082001.
- [232] C. T. Y. Chung, A. Melatos, B. Krishnan, J. T. Whelan, Designing a cross-correlation search for continuous-wave gravitational radiation from a neutron star in the supernova remnant SNR 1987A, *Monthly Notices of the Royal Astronomical Society* 414 (2011) 2650. doi:10.1111/j.1365-2966.2011.18585.x.
- [233] J. T. Whelan, S. Sundaesan, Y. Zhang, P. Peiris, Model-based cross-correlation search for gravitational waves from Scorpius X-1, *Physical Review D* 91 (2015) 102005. doi:10.1103/PhysRevD.91.102005.
- [234] G. D. Meadors, B. Krishnan, M. A. Papa, J. T. Whelan, Y. Zhang, Resampling to accelerate cross-correlation searches for continuous gravitational waves from binary systems, *Physical Review D* 97 (2018) 044017. doi:10.1103/PhysRevD.97.044017.
- [235] K. J. Wagner, J. T. Whelan, J. K. Wofford, K. Wette, Template lattices for a cross-correlation search for gravitational waves from Scorpius X-1, *Classical and Quantum Gravity* 39 (2022) 075013. doi:10.1088/1361-6382/ac5012.
- [236] E. Goetz, K. Riles, An all-sky search algorithm for continuous gravitational waves from spinning neutron stars in binary systems, *Classical and Quantum Gravity* 28 (2011) 215006.

- doi:10.1088/0264-9381/28/21/215006.
- [237] E. Goetz, K. Riles, Coherently combining data between detectors for all-sky semi-coherent continuous gravitational wave searches, *Classical and Quantum Gravity* 33 (2016) 085007. doi:10.1088/0264-9381/33/8/085007.
- [238] G. D. Meadors, E. Goetz, K. Riles, Tuning into Scorpius X-1: adapting a continuous gravitational-wave search for a known binary system, *Classical and Quantum Gravity* 33 (2016) 105017. doi:10.1088/0264-9381/33/10/105017.
- [239] S. Suvorova, L. Sun, A. Melatos, W. Moran, R. J. Evans, Hidden Markov model tracking of continuous gravitational waves from a neutron star with wandering spin, *Physical Review D* 93 (2016) 123009. doi:10.1103/PhysRevD.93.123009.
- [240] L. Sun, A. Melatos, S. Suvorova, W. Moran, R. J. Evans, Hidden Markov model tracking of continuous gravitational waves from young supernova remnants, *Physical Review D* 97 (2018) 043013. doi:10.1103/PhysRevD.97.043013.
- [241] A. Melatos, P. Clearwater, S. Suvorova, L. Sun, W. Moran, R. J. Evans, Hidden Markov model tracking of continuous gravitational waves from a binary neutron star with wandering spin. III. Rotational phase tracking, *Physical Review D* 104 (2021) 042003. doi:10.1103/PhysRevD.104.042003.
- [242] J. Bayley, C. Messenger, G. Woan, Generalized application of the Viterbi algorithm to searches for continuous gravitational-wave signals, *Physical Review D* 100 (2019) 023006. doi:10.1103/PhysRevD.100.023006.
- [243] L. Sun, A. Melatos, Application of hidden Markov model tracking to the search for long-duration transient gravitational waves from the remnant of the binary neutron star merger GW170817, *Physical Review D* 99 (2019) 123003. doi:10.1103/PhysRevD.99.123003.
- [244] J. Bayley, C. Messenger, G. Woan, Robust machine learning algorithm to search for continuous gravitational waves, *Physical Review D* 102 (2020) 083024. doi:10.1103/PhysRevD.102.083024.
- [245] J. Abadie, et al., First Search for Gravitational Waves from the Youngest Known Neutron Star, *Astrophysical Journal* 722 (2010) 1504. doi:10.1088/0004-637X/722/2/1504.
- [246] K. Wette, L. Dunn, P. Clearwater, A. Melatos, Deep exploration for continuous gravitational waves at 171–172 Hz in LIGO second observing run data, *Physical Review D* 103 (2021) 083020. doi:10.1103/PhysRevD.103.083020.
- [247] R. Tenorio, L. M. Modafferi, D. Keitel, A. M. Sintes, Empirically estimating the distribution of the loudest candidate from a gravitational-wave search, *Physical Review D* 105 (2022) 044029. doi:10.1103/PhysRevD.105.044029.
- [248] A. Singh, M. A. Papa, H.-B. Eggenstein, S. Walsh, Adaptive clustering procedure for continuous gravitational wave searches, *Physical Review D* 96 (2017) 082003. doi:10.1103/PhysRevD.96.082003.
- [249] F. Morawski, M. Bejger, P. Ciecieląg, Machine learning classification of continuous gravitational-wave signal candidates, in: K. Małek, M. Polińska, A. Majczyna, G. Stachowski, R. Poleski, Ł. Wyrzykowski, A. Różańska (Eds.), XXXIX Polish Astronomical Society Meeting, Vol. 10, 2020, p. 33. URL <https://ui.adsabs.harvard.edu/abs/2020past.conf..33M>
- [250] B. Beheshtipour, M. A. Papa, Deep learning for clustering of continuous gravitational wave candidates, *Physical Review D* 101 (2020) 064009. doi:10.1103/PhysRevD.101.064009.
- [251] B. Beheshtipour, M. A. Papa, Deep learning for clustering of continuous gravitational wave candidates. II. Identification of low-SNR candidates, *Physical Review D* 103 (2021) 064027. doi:10.1103/PhysRevD.103.064027.
- [252] R. Tenorio, D. Keitel, A. M. Sintes, Time-frequency track distance for comparing continuous gravitational wave signals, *Physical Review D* 103 (2021) 064053. doi:10.1103/PhysRevD.103.064053.
- [253] L. Pierini, P. Astone, C. Palomba, A. Nyquist, S. Dall’Osso, S. D’Antonio, S. Frasca, I. La Rosa, P. Leaci, F. Muciaccia, O. J. Piccinni, L. Rei, Impact of signal clusters in wide-band searches for continuous gravitational waves, *Physical Review D* 106 (2022) 042009. doi:10.1103/PhysRevD.106.042009.
- [254] B. Steltner, T. Menne, M. A. Papa, H.-B. Eggenstein, Density-clustering of continuous gravitational wave candidates from large surveys, *Physical Review D* 106 (2022) 104063. doi:10.1103/PhysRevD.106.104063.
- [255] P. Leaci, Methods to filter out spurious disturbances in continuous-wave searches from gravitational-wave detectors, *Physica Scripta* 90 (2015) 125001. doi:10.1088/0031-8949/90/12/125001.
- [256] S. J. Zhu, M. A. Papa, S. Walsh, New veto for continuous gravitational wave searches, *Physical Review D* 96 (2017) 124007. doi:10.1103/PhysRevD.96.124007.
- [257] G. Intini, P. Leaci, P. Astone, S. D. Antonio, S. Frasca, I. La Rosa, A. Miller, C. Palomba, O. Piccinni, A Doppler-modulation based veto to discard false continuous gravitational-wave candidates, *Classical and Quantum Gravity* 37 (2020) 225007. doi:10.1088/1361-6382/abac43.
- [258] D. Keitel, R. Prix, Line-robust statistics for continuous gravitational waves: safety in the case of unequal detector sensitivities, *Classical and Quantum Gravity* 32 (2015) 035004. doi:10.1088/0264-9381/32/3/035004.
- [259] D. Keitel, R. Prix, M. A. Papa, P. Leaci, M. Siddiqi, Search for continuous gravitational waves: Improving robustness versus instrumental artifacts, *Physical Review D* 89 (2014) 064023. doi:10.1103/PhysRevD.89.064023.
- [260] D. Keitel, Robust semicoherent searches for continuous gravitational waves with noise and signal models including hours to days long transients, *Physical Review D* 93 (2016) 084024. doi:10.1103/PhysRevD.93.084024.
- [261] G. Ashton, R. Prix, D. I. Jones, A semicoherent glitch-robust continuous-gravitational-wave search method, *Physical Review D* 98 (2018) 063011. doi:10.1103/PhysRevD.98.063011.
- [262] M. Shaltev, Coherent follow-up of Continuous Gravitational-Wave candidates: minimal required observation time, in: 9th Edoardo Amaldi Conference on Gravitational Waves and 2011 Numerical Relativity–Data Analysis Meeting, Vol. 363 of Journal of Physics Conference Series, 2012, p. 012043. doi:10.1088/1742-6596/363/1/012043.
- [263] M. Shaltev, R. Prix, Fully coherent follow-up of continuous gravitational-wave candidates, *Physical Review D* 87 (2013) 084057. doi:10.1103/PhysRevD.87.084057.
- [264] G. Ashton, R. Prix, Hierarchical multistage MCMC follow-up of continuous gravitational wave candidates, *Physical Review D* 97 (2018) 103020. doi:10.1103/PhysRevD.97.103020.
- [265] D. Keitel, R. Tenorio, G. Ashton, R. Prix, PyFstat: a Python package for continuous gravitational-wave data analysis, *The Journal of Open Source Software* 6 (2021) 3000. doi:10.21105/joss.03000.
- [266] R. Tenorio, D. Keitel, A. M. Sintes, Application of a hierarchical MCMC follow-up to Advanced LIGO continuous gravitational-wave candidates, *Physical Review D* 104 (2021) 084012. doi:10.1103/PhysRevD.104.084012.
- [267] C. Dreissigacker, R. Sharma, C. Messenger, R. Zhao, R. Prix, Deep-learning continuous gravitational waves, *Physical Review D* 100 (2019) 044009. doi:10.1103/PhysRevD.100.044009.
- [268] A. L. Miller, P. Astone, S. D’Antonio, S. Frasca, G. Intini, I. La Rosa, P. Leaci, S. Mastrogiovanni, F. Muciaccia, A. Mitidis, C. Palomba, O. J. Piccinni, A. Singhal, B. F. Whiting, L. Rei, How effective is machine learning to detect long transient gravitational waves from neutron stars in a real search?, *Physical Review D* 100 (2019) 062005. doi:10.1103/PhysRevD.100.062005.
- [269] C. Dreissigacker, R. Prix, Deep-learning continuous gravitational waves: Multiple detectors and realistic noise, *Physical Review D* 102 (2020) 022005. doi:10.1103/PhysRevD.102.022005.
- [270] T. S. Yamamoto, T. Tanaka, Use of an excess power method and a convolutional neural network in an all-sky search for continuous gravitational waves, *Physical Review D* 103 (2021) 084049. doi:10.1103/PhysRevD.103.084049.

- [271] R. Tenorio, M. J. Williams, C. Messenger, Learning to detect continuous gravitational waves, Tech. rep. (2022). URL <https://www.kaggle.com/competitions/g2net-detecting-continuous-gravitational-waves/overview>
- [272] D. I. Jones, Learning from the Frequency Content of Continuous Gravitational Wave Signals, World Scientific, 2022, Ch. Chapter 6, pp. 201–217. doi:10.1142/9789811220944_0006.
- [273] M. Sieniawska, D. I. Jones, Gravitational waves from spinning neutron stars as not-quite-standard sirens, Monthly Notices of the Royal Astronomical Society 509 (2022) 5179. doi:10.1093/mnras/stab3315.
- [274] N. Lu, K. Wette, S. M. Scott, A. Melatos, Inferring neutron star properties with continuous gravitational waves, Monthly Notices of the Royal Astronomical Society 521 (2023) 2103. doi:10.1093/mnras/stad390.
- [275] M. Sieniawska, D. I. Jones, A. L. Miller, Measuring neutron-star distances and properties with gravitational-wave parallax, Monthly Notices of the Royal Astronomical Society 521 (2023) 1924. doi:10.1093/mnras/stad624.
- [276] B. Haskell, M. Bejger, Astrophysics with Continuous Gravitational Waves, submitted (2023).
- [277] B. Haskell, K. Schwenzer, Isolated Neutron Stars, Springer Singapore, Singapore, 2020, pp. 1–28. doi:10.1007/978-981-15-4702-7_12-1.
- [278] B. Haskell, N. Andersson, C. D’Angelo, N. Degenaar, K. Glampedakis, W. C. G. Ho, P. D. Lasky, A. Melatos, M. Oppenorth, A. Patruno, M. Priymak, Gravitational Waves from Rapidly Rotating Neutron Stars, in: C. F. Sopuerta (Ed.), Gravitational Wave Astrophysics, Vol. 40 of Astrophysics and Space Science Proceedings, 2015, p. 85. doi:10.1007/978-3-319-10488-1_8.
- [279] P. D. Lasky, Gravitational Waves from Neutron Stars: A Review, Publications of the Astronomical Society of Australia 32 (2015) e034. doi:10.1017/pasa.2015.35.
- [280] R. Tenorio, D. Keitel, A. M. Sintes, Search Methods for Continuous Gravitational-Wave Signals from Unknown Sources in the Advanced-Detector Era, Universe 7 (2021) 474. doi:10.3390/universe7120474.
- [281] R. Prix, Gravitational Waves from Spinning Neutron Stars, in: W. Becker (Ed.), Neutron Stars and Pulsars, Vol. 357 of Astrophysics and Space Science Library, Springer, Berlin/Heidelberg, 2009, p. 651. doi:10.1007/978-3-540-76965-1_24.
- [282] K. Riles, Searches for continuous-wave gravitational radiation, Living Reviews in Relativity 26 (2023) 3. doi:10.1007/s41114-023-00044-3.
- [283] O. J. Piccinni, Status and Perspectives of Continuous Gravitational Wave Searches, Galaxies 10 (2022). doi:10.3390/galaxies10030072.
- [284] M. Sieniawska, M. Bejger, Continuous Gravitational Waves from Neutron Stars: Current Status and Prospects, Universe 5 (2019) 217. doi:10.3390/universe5110217.
- [285] K. Riles, Recent searches for continuous gravitational waves, Modern Physics Letters A 32 (2017) 1730035. doi:10.1142/S021773231730035X.
- [286] P. Leaci, LIGO Scientific Collaboration, Virgo Collaboration, Searching for continuous gravitational wave signals using LIGO and Virgo detectors, in: 3rd Italian-Pakistani Workshop on Relativistic Astrophysics, Vol. 354 of Journal of Physics Conference Series, 2012, p. 012010. doi:10.1088/1742-6596/354/1/012010.
- [287] Adobe, Inc, Convert PDF to Excel (2023). URL <https://www.adobe.com/acrobat/online/pdf-to-excel.html>
- [288] A. M. Price-Whelan, et al., The Astropy Project: Sustaining and Growing a Community-oriented Open-source Project and the Latest Major Release (v5.0) of the Core Package, Astrophysical Journal 935 (2022) 167. doi:10.3847/1538-4357/ac7c74.
- [289] K. P. Larsen, graphreader.com (2023). URL <http://www.graphreader.com/>
- [290] T. Kluyver, et al., Jupyter Notebooks - a publishing format for reproducible computational workflows, in: F. Loizides, B. Schmidt (Eds.), Positioning and Power in Academic Publishing: Players, Agents and Agendas, IOS Press, Netherlands, 2016, p. 87. doi:10.3233/978-1-61499-649-1-87.
- [291] Wolfram Research, Inc, Mathematica, Version 12.0 (2019). URL <https://www.wolfram.com/mathematica>
- [292] C. R. Harris, et al., Array programming with NumPy, Nature 585 (2020) 357–362. doi:10.1038/s41586-020-2649-2.
- [293] S. Chandrasekhar, Erratum: Solutions of Two Problems in the Theory of Gravitational Radiation, Physical Review Letters 24 (1970) 762. doi:10.1103/PhysRevLett.24.762.3.
- [294] B. Abbott, et al., Erratum: All-sky search for periodic gravitational waves in LIGO S4 data [Phys. Rev. D 77, 022001 (2008)], Physical Review D 80 (2009) 129904. doi:10.1103/PhysRevD.80.129904.
- [295] L. Fesik, M. A. Papa, Erratum: “First Search for r-mode Gravitational Waves from PSR J0537-6910” (2020, ApJ, 895, 11), Astrophysical Journal 897 (2020) 185. doi:10.3847/1538-4357/aba04e.
- [296] B. P. Abbott, et al., Erratum: “Searches for Gravitational Waves from Known Pulsars at Two Harmonics in 2015-2017 LIGO Data” (2019, ApJ, 879, 10), Astrophysical Journal 882 (2019) 73. doi:10.3847/1538-4357/ab3231.
- [297] B. P. Abbott, et al., Erratum: “Searches for Gravitational Waves from Known Pulsars at Two Harmonics in 2015-2017 LIGO Data” (2019, ApJ, 879, 10), Astrophysical Journal 899 (2020) 170. doi:10.3847/1538-4357/abaabb.
- [298] B. Abbott, et al., Erratum: “Beating the Spin-Down Limit on Gravitational Wave Emission from the Crab Pulsar” (2008, ApJ, 683, L45), Astrophysical Journal Letters 706 (2009) L203. doi:10.1088/0004-637X/706/1/L203.
- [299] B. P. Abbott, et al., Erratum: “First Search for Gravitational Waves from Known Pulsars with Advanced LIGO” (2017, ApJ, 839, 12), Astrophysical Journal 851 (2017) 71. doi:10.3847/1538-4357/aa9aee.
- [300] B. P. Abbott, et al., Erratum: First narrow-band search for continuous gravitational waves from known pulsars in advanced detector data [Phys. Rev. D 96, 122006 (2017)], Physical Review D 97 (2018) 129903. doi:10.1103/PhysRevD.97.129903.
- [301] J. Aasi, et al., Erratum: “Searches for Continuous Gravitational Waves from Nine Young Supernova Remnants” (2015, ApJ, 813, 39), Astrophysical Journal 918 (2021) 90. doi:10.3847/1538-4357/ac1f2d.
- [302] B. P. Abbott, et al., Erratum: “Searches for Continuous Gravitational Waves from 15 Supernova Remnants and Fomalhaut b with Advanced LIGO” (2019, ApJ, 875, 122), Astrophysical Journal 918 (2021) 91. doi:10.3847/1538-4357/ac1f2c.
- [303] L. Lindblom, B. J. Owen, Erratum: Directed searches for continuous gravitational waves from twelve supernova remnants in data from Advanced LIGO’s second observing run [Phys. Rev. D 101, 083023 (2020)], Physical Review D 104 (2021) 109902. doi:10.1103/PhysRevD.104.109902.
- [304] B. P. Abbott, et al., Erratum: Search for gravitational waves from Scorpius X-1 in the first Advanced LIGO observing run with a hidden Markov model [Phys. Rev. D 95, 122003 (2017)], Physical Review D 104 (2021) 129901. doi:10.1103/PhysRevD.104.129901.
- [305] B. P. Abbott, et al., Erratum: Search for gravitational waves from Scorpius X-1 in the second Advanced LIGO observing run with an improved hidden Markov model [Phys. Rev. D 100, 122002 (2019)], Physical Review D 104 (2021) 109903. doi:10.1103/PhysRevD.104.109903.
- [306] B. Abbott, et al., Setting upper limits on the strength of periodic gravitational waves from PSR J1939+2134 using the first science data from the GEO 600 and LIGO detectors, Physical Review D 69 (2004) 082004. doi:10.1103/PhysRevD.69.082004.
- [307] B. Abbott, et al., Limits on Gravitational-Wave Emission from

- Selected Pulsars Using LIGO Data, *Physical Review Letters* 94 (2005) 181103. doi:10.1103/PhysRevLett.94.181103.
- [308] B. Abbott, et al., Upper limits on gravitational wave emission from 78 radio pulsars, *Physical Review D* 76 (2007) 042001. doi:10.1103/PhysRevD.76.042001.
- [309] B. P. Abbott, et al., Searches for Gravitational Waves from Known Pulsars at Two Harmonics in 2015-2017 LIGO Data, *Astrophysical Journal* 879 (2019) 10, errata: [296, 297]. doi:10.3847/1538-4357/ab20cb.
- [310] J. Abadie, et al., Beating the spin-down limit on gravitational wave emission from the Vela pulsar, *Astrophysical Journal* 737 (2011) 93. doi:10.1088/0004-637X/737/2/93.
- [311] J. Aasi, et al., Gravitational Waves from Known Pulsars: Results from the Initial Detector Era, *Astrophysical Journal* 785 (2014) 119. doi:10.1088/0004-637X/785/2/119.
- [312] B. Abbott, et al., Beating the Spin-Down Limit on Gravitational Wave Emission from the Crab Pulsar, *Astrophysical Journal Letters* 683 (2008) L45, erratum: [298]. doi:10.1086/591526.
- [313] B. P. Abbott, et al., First Search for Gravitational Waves from Known Pulsars with Advanced LIGO, *Astrophysical Journal* 839 (2017) 12, erratum: [299]. doi:10.3847/1538-4357/aa677f.
- [314] B. P. Abbott, et al., Searches for Gravitational Waves from Known Pulsars with Science Run 5 LIGO Data, *Astrophysical Journal* 713 (2010) 671. doi:10.1088/0004-637X/713/1/671.
- [315] A. Ashok, B. Beheshtipour, M. A. Papa, P. C. C. Freire, B. Steltner, B. Machenschalk, O. Behnke, B. Allen, R. Prix, New Searches for Continuous Gravitational Waves from Seven Fast Pulsars, *Astrophysical Journal* 923 (2021) 85. doi:10.3847/1538-4357/ac2582.
- [316] B. P. Abbott, et al., First narrow-band search for continuous gravitational waves from known pulsars in advanced detector data, *Physical Review D* 96 (2017) 122006, erratum: [300]. doi:10.1103/PhysRevD.96.122006.
- [317] J. Aasi, et al., Narrow-band search of continuous gravitational-wave signals from Crab and Vela pulsars in Virgo VSR4 data, *Physical Review D* 91 (2015) 022004. doi:10.1103/PhysRevD.91.022004.
- [318] B. P. Abbott, et al., Narrow-band search for gravitational waves from known pulsars using the second LIGO observing run, *Physical Review D* 99 (2019) 122002. doi:10.1103/PhysRevD.99.122002.
- [319] D. Beniwal, P. Clearwater, L. Dunn, L. Strang, G. Rowell, A. Melatos, D. Ottaway, Search for continuous gravitational waves from HESS J1427-608 with a hidden Markov model, *Physical Review D* 106 (2022) 103018. doi:10.1103/PhysRevD.106.103018.
- [320] J. Aasi, et al., Searches for Continuous Gravitational Waves from Nine Young Supernova Remnants, *Astrophysical Journal* 813 (2015) 39, erratum: [301]. doi:10.1088/0004-637X/813/1/39.
- [321] B. P. Abbott, et al., Searches for Continuous Gravitational Waves from 15 Supernova Remnants and Fomalhaut b with Advanced LIGO, *Astrophysical Journal* 875 (2019) 122, erratum: [302]. doi:10.3847/1538-4357/ab113b.
- [322] B. J. Owen, L. Lindblom, L. S. Pinheiro, First Constraining Upper Limits on Gravitational-wave Emission from NS 1987A in SNR 1987A, *Astrophysical Journal Letters* 935 (2022) L7. doi:10.3847/2041-8213/ac84dc.
- [323] L. Lindblom, B. J. Owen, Directed searches for continuous gravitational waves from twelve supernova remnants in data from Advanced LIGO's second observing run, *Physical Review D* 101 (2020) 083023, erratum: [303]. doi:10.1103/PhysRevD.101.083023.
- [324] S. J. Zhu, M. A. Papa, H.-B. Eggenstein, R. Prix, K. Wette, B. Allen, O. Bock, D. Keitel, B. Krishnan, B. Machenschalk, M. Shaltev, X. Siemens, Einstein@Home search for continuous gravitational waves from Cassiopeia A, *Physical Review D* 94 (2016) 082008. doi:10.1103/PhysRevD.94.082008.
- [325] D. Jones, L. Sun, Search for continuous gravitational waves from Fomalhaut b in the second Advanced LIGO observing run with a hidden Markov model, *Physical Review D* 103 (2021) 023020. doi:10.1103/PhysRevD.103.023020.
- [326] L. Sun, A. Melatos, P. D. Lasky, C. T. Y. Chung, N. S. Darman, Cross-correlation search for continuous gravitational waves from a compact object in SNR 1987A in LIGO Science run 5, *Physical Review D* 94 (2016) 082004. doi:10.1103/PhysRevD.94.082004.
- [327] J. Ming, M. A. Papa, A. Singh, H.-B. Eggenstein, S. J. Zhu, V. Dergachev, Y. Hu, R. Prix, B. Machenschalk, C. Beer, O. Behnke, B. Allen, Results from an Einstein@Home search for continuous gravitational waves from Cassiopeia A, Vela Jr., and G347.3, *Physical Review D* 100 (2019) 024063. doi:10.1103/PhysRevD.100.024063.
- [328] J. Aasi, et al., First all-sky search for continuous gravitational waves from unknown sources in binary systems, *Physical Review D* 90 (2014) 062010. doi:10.1103/PhysRevD.90.062010.
- [329] J. Aasi, et al., Directed search for gravitational waves from Scorpius X-1 with initial LIGO data, *Physical Review D* 91 (2015) 062008. doi:10.1103/PhysRevD.91.062008.
- [330] G. D. Meadors, E. Goetz, K. Riles, T. Creighton, F. Robinet, Searches for continuous gravitational waves from Scorpius X-1 and XTE J1751-305 in LIGO's sixth science run, *Physical Review D* 95 (2017) 042005. doi:10.1103/PhysRevD.95.042005.
- [331] B. P. Abbott, et al., Search for gravitational waves from Scorpius X-1 in the first Advanced LIGO observing run with a hidden Markov model, *Physical Review D* 95 (2017) 122003, erratum: [304]. doi:10.1103/PhysRevD.95.122003.
- [332] B. P. Abbott, et al., Search for gravitational waves from Scorpius X-1 in the second Advanced LIGO observing run with an improved hidden Markov model, *Physical Review D* 100 (2019) 122002, erratum: [305]. doi:10.1103/PhysRevD.100.122002.
- [333] B. P. Abbott, et al., Upper Limits on Gravitational Waves from Scorpius X-1 from a Model-based Cross-correlation Search in Advanced LIGO Data, *Astrophysical Journal* 847 (2017) 47. doi:10.3847/1538-4357/aa86f0.
- [334] B. P. Abbott, et al., Search for continuous gravitational waves from neutron stars in globular cluster NGC 6544, *Physical Review D* 95 (2017) 082005. doi:10.1103/PhysRevD.95.082005.
- [335] J. Aasi, et al., Search of the Orion spur for continuous gravitational waves using a loosely coherent algorithm on data from LIGO interferometers, *Physical Review D* 93 (2016) 042006. doi:10.1103/PhysRevD.93.042006.
- [336] J. Aasi, et al., Directed search for continuous gravitational waves from the Galactic center, *Physical Review D* 88 (2013) 102002. doi:10.1103/PhysRevD.88.102002.
- [337] V. Dergachev, M. A. Papa, B. Steltner, H.-B. Eggenstein, Loosely coherent search in LIGO O1 data for continuous gravitational waves from Terzan 5 and the Galactic Center, *Physical Review D* 99 (2019) 084048. doi:10.1103/PhysRevD.99.084048.
- [338] B. Abbott, et al., First all-sky upper limits from LIGO on the strength of periodic gravitational waves using the Hough transform, *Physical Review D* 72 (2005) 102004. doi:10.1103/PhysRevD.72.102004.
- [339] B. P. Abbott, et al., Einstein@Home search for periodic gravitational waves in early S5 LIGO data, *Physical Review D* 80 (2009) 042003. doi:10.1103/PhysRevD.80.042003.
- [340] J. Aasi, et al., First low frequency all-sky search for continuous gravitational wave signals, *Physical Review D* 93 (2016) 042007. doi:10.1103/PhysRevD.93.042007.
- [341] B. P. Abbott, et al., Comprehensive all-sky search for periodic gravitational waves in the sixth science run LIGO data, *Physical Review D* 94 (2016) 042002. doi:10.1103/PhysRevD.94.042002.
- [342] B. P. Abbott, et al., Results of the deepest all-sky survey for continuous gravitational waves on LIGO S6 data running on the Einstein@Home volunteer distributed computing project, *Physical Review D* 94 (2016) 102002. doi:10.1103/PhysRevD.94.102002.
- [343] B. P. Abbott, et al., Full band all-sky search for periodic grav-

- itational waves in the O1 LIGO data, *Physical Review D* 97 (2018) 102003. doi:10.1103/PhysRevD.97.102003.
- [344] J. Aasi, et al., Implementation of an \mathcal{F} -statistic all-sky search for continuous gravitational waves in Virgo VSR1 data, *Classical and Quantum Gravity* 31 (2014) 165014. doi:10.1088/0264-9381/31/16/165014.
- [345] B. P. Abbott, et al., All-Sky LIGO Search for Periodic Gravitational Waves in the Early Fifth-Science-Run Data, *Physical Review Letters* 102 (2009) 111102. doi:10.1103/PhysRevLett.102.111102.
- [346] J. Aasi, et al., Application of a Hough search for continuous gravitational waves on data from the fifth LIGO science run, *Classical and Quantum Gravity* 31 (2014) 085014. doi:10.1088/0264-9381/31/8/085014.
- [347] J. Abadie, et al., All-sky search for periodic gravitational waves in the full S5 LIGO data, *Physical Review D* 85 (2012) 022001. doi:10.1103/PhysRevD.85.022001.
- [348] A. Singh, M. A. Papa, H.-B. Eggenstein, S. Zhu, H. Pletsch, B. Allen, O. Bock, B. Maschenschalk, R. Prix, X. Siemens, Results of an all-sky high-frequency Einstein@Home search for continuous gravitational waves in LIGO's fifth science run, *Physical Review D* 94 (2016) 064061. doi:10.1103/PhysRevD.94.064061.
- [349] B. P. Abbott, et al., First low-frequency Einstein@Home all-sky search for continuous gravitational waves in Advanced LIGO data, *Physical Review D* 96 (2017) 122004. doi:10.1103/PhysRevD.96.122004.
- [350] V. Dergachev, M. A. Papa, Results from an extended Falcon all-sky survey for continuous gravitational waves, *Physical Review D* 101 (2020) 022001. doi:10.1103/PhysRevD.101.022001.
- [351] B. P. Abbott, et al., All-sky search for continuous gravitational waves from isolated neutron stars using Advanced LIGO O2 data, *Physical Review D* 100 (2019) 024004. doi:10.1103/PhysRevD.100.024004.
- [352] V. Dergachev, M. A. Papa, Frequency-Resolved Atlas of the Sky in Continuous Gravitational Waves, *Physical Review X* 13 (2023) 021020. doi:10.1103/PhysRevX.13.021020.
- [353] V. Dergachev, M. A. Papa, Search for continuous gravitational waves from small-ellipticity sources at low frequencies, *Physical Review D* 104 (2021) 043003. doi:10.1103/PhysRevD.104.043003.
- [354] V. Dergachev, M. A. Papa, Results from the First All-Sky Search for Continuous Gravitational Waves from Small-Ellipticity Sources, *Physical Review Letters* 125 (2020) 171101. doi:10.1103/PhysRevLett.125.171101.
- [355] B. Steltner, M. A. Papa, H.-B. Eggenstein, B. Allen, V. Dergachev, R. Prix, B. Machenschalk, S. Walsh, S. J. Zhu, O. Behnke, S. Kwang, Einstein@Home All-sky Search for Continuous Gravitational Waves in LIGO O2 Public Data, *Astrophysical Journal* 909 (2021) 79. doi:10.3847/1538-4357/abc7c9.
- [356] P. B. Covas, A. M. Sintes, First All-Sky Search for Continuous Gravitational-Wave Signals from Unknown Neutron Stars in Binary Systems Using Advanced LIGO Data, *Physical Review Letters* 124 (2020) 191102. doi:10.1103/PhysRevLett.124.191102.

Appendix A. Table of continuous wave searches

Table A.3: CW searches, 2003–2022, organised by target parameter space. Columns are: most recent observing run data used, astrophysical target, (coherent, incoherent) analysis algorithm used, parameter-space breadth, sensitivity depth, weighted search volume, and references. Notes to the table, labelled with superscript letters, are listed following the table (starting on page 44). A machine-readable version is provided in the supplementary material to this review.

Obs.	Target ^a	Algorithm ^b		Breadth						Depth		Vol.	Ref.	
		Coh.	Inc.	\mathcal{B}_f	\mathcal{B}_j	$\mathcal{B}_{\dot{f}}$	\mathcal{B}_{sky}	\mathcal{B}_{bin}	\mathcal{B}_{HMM}	\mathcal{B}	\mathcal{D}			$f_{\mathcal{D}}$
				lg	lg	lg	lg	lg	lg	lg	Hz	lg		
Targeted searches for known pulsars (“Pulsars T”)														
S1	J1939	Bayes	–	–	–	–	–	–	–	0	85.0 ^c	–	27.7	306
S1	J1939	\mathcal{F} -stat	–	–	–	–	–	–	–	0	100.0 ^c	–	28.8	306
S2	28 pulsars	Bayes	–	–	–	–	–	–	–	1.45	160.0 ^c	–	32.9	307
O3	35 pulsars	5-vec	–	–	–	–	–	–	–	1.54	39.0 ^d	89.6	37.2	133
S4	78 pulsars	Bayes	–	–	–	–	–	–	–	1.89	300.0 ^c	–	37.4	308
O2	24 pulsars	\mathcal{F} -stat	–	–	–	–	–	–	–	1.38	58.0 ^e	41.6	41.0	309
VSR2	Vela	Bayes	–	–	–	–	–	–	–	0	590.0 ^f	22.4	41.2	310
VSR2	Vela	\mathcal{F} -stat	–	–	–	–	–	–	–	0	590.0 ^f	22.4	41.2	310
S6	7 pulsars	5-vec	–	–	–	–	–	–	–	0.845	530.0 ^g	50.6	41.4	311
VSR2	Vela	5-vec	–	–	–	–	–	–	–	0	640.0 ^f	22.4	41.8	310
S6	179 pulsars	Bayes	–	–	–	–	–	–	–	2.25	510.0 ^c	–	42.6	311
S6	7 pulsars	\mathcal{F} -stat	–	–	–	–	–	–	–	0.845	980.0 ^g	59.4	45.4	311
O2	42 pulsars	5-vec	–	–	–	–	–	–	–	1.62	90.0 ^h	116.0	45.5	309
O3	46 pulsars	\mathcal{F} -stat	–	–	–	–	–	–	–	1.66	97.0 ⁱ	70.2	46.3	133
O3	10 pulsars	Bayes	–	–	–	–	–	–	–	1.0	130.0 ^j	182.1	48.2	134
O3	10 pulsars	\mathcal{F} -stat	–	–	–	–	–	–	–	1.0	140.0 ^j	182.1	48.9	134
S5	Crab	Bayes	–	–	–	–	–	–	–	0	770.0 ^c	–	54.8	312
O2	439 pulsars	Bayes	–	–	–	–	–	–	–	2.64	260.0 ^e	391.2	56.9	309
O1	11 pulsars	\mathcal{F} -stat	–	–	–	–	–	–	–	1.04	320.0 ^k	30.4	57.1	313
O1	10 pulsars	5-vec	–	–	–	–	–	–	–	1.0	320.0 ^k	29.1	57.4	313
O3	6 pulsars	5-vec	–	–	–	–	–	–	–	0.778	350.0 ^l	22.4	57.8	134
S5	116 pulsars	Bayes	–	–	–	–	–	–	–	2.06	930.0 ^c	–	58.3	314
S5	43 pulsars	Bayes	–	–	–	–	–	–	–	1.63	1000.0 ^m	654.9	58.7	30
O1	200 pulsars	Bayes	–	–	–	–	–	–	–	2.3	360.0 ^c	–	59.6	313
O3	470 pulsars	Bayes	–	–	–	–	–	–	–	2.67	360.0 ⁱ	242.2	59.9	133
O3	J0537	Bayes	–	–	–	–	–	–	–	0	550.0 ^d	123.8	61.5	135
O3	7 pulsars	\mathcal{F} -stat	–	–	–	–	–	–	–	0.845	800.0 ^j	845.8	66.0	315
Narrow-band searches for known pulsars (“Pulsars NB”)														
O1	Crab	5-vec	–	6.31	1.63	–	–	–	–	7.94	9.9 ^k	59.3	30.3	316
VSR4	Vela	5-vec	–	5.47	0	–	–	–	–	5.47	90.0 ^c	–	34.6	317
VSR4	Crab	5-vec	–	5.47	0.585	–	–	–	–	6.05	100.0 ^c	–	35.9	317
O1	Vela	5-vec	–	5.78	0.272	–	–	–	–	6.05	30.0 ^k	22.4	39.1	316
O1	J0205	5-vec	–	5.78	0.707	–	–	–	–	6.49	55.0 ^k	30.4	45.5	316
O1	J2229	5-vec	–	6.08	0.539	–	–	–	–	6.62	63.0 ^k	38.7	47.0	316
O1	J1813	5-vec	–	6.0	0.945	–	–	–	–	6.95	61.0 ^k	44.7	47.0	316
O2	J0205 ⁿ	5-vec	–	5.92	0.576	–	–	–	–	6.5	77.0 ^h	30.4	48.8	318
O2	J1028 ⁿ	5-vec	–	5.74	0	–	–	–	–	5.74	84.0 ^h	21.9	48.9	318
O2	J1028 ^o	5-vec	–	6.05	0.168	–	–	–	–	6.22	82.0 ^h	21.9	49.2	318
S5	Crab	\mathcal{F} -stat	–	5.71	–	–	–	–	–	5.71	220.0 ^c	–	50.2	312
O1	J1833	5-vec	–	5.91	0.788	–	–	–	–	6.7	100.0 ^k	32.3	51.6	316
O2	Crab ^o	5-vec	–	6.34	1.56	–	–	–	–	7.9	94.0 ^h	59.3	52.2	318
O1	J1813	5-vec	–	5.91	0.272	–	–	–	–	6.18	110.0 ^k	41.6	52.4	316
O2	Crab	\mathcal{F} -stat	–	8.04	1.16 ^p	0 ^q	–	–	–	9.2	93.0 ^h	46.4	53.4	157
O1	J1952	5-vec	–	6.0	0.272	–	–	–	–	6.28	130.0 ^k	50.6	53.5	316

Table A.3 continued.

Obs.	Target ^a	Algorithm ^b		Breadth						Depth		Vol.	Ref.	
		Coh.	Inc.	\mathcal{B}_f	\mathcal{B}_j	\mathcal{B}_f	\mathcal{B}_{sky}	\mathcal{B}_{bin}	\mathcal{B}_{HMM}	\mathcal{B}	\mathcal{D}			$f_{\mathcal{D}}$
				lg	lg	lg	lg	lg	lg	lg		Hz	lg	
O2	J0205 ^o	5-vec	–	6.22	1.13	–	–	–	–	7.35	120.0 ^h	30.4	53.9	318
O2	Crab ⁿ	5-vec	–	6.45	1.77	–	–	–	–	8.22	110.0 ^h	59.3	54.1	318
O3	Crab ^o	\mathcal{F} -stat	–	6.63	1.81	–	–	–	–	8.44	110.0 ^d	59.2	54.3	136
O2	Crab	\mathcal{F} -stat	–	8.04	1.16 ^P	0 ^q	–	–	–	9.2	100.0 ^k	46.4	54.6	157
O2	J0940	5-vec	–	6.32	0.497	–	–	–	–	6.82	140.0 ^h	22.9	55.0	318
O3	J1813 ^o	\mathcal{F} -stat	–	6.54	1.14	–	–	–	–	7.68	130.0 ^d	44.7	55.0	136
O2	J1718 ^o	5-vec	–	6.22	0.135	–	–	–	–	6.36	150.0 ^h	26.8	55.0	318
O2	Crab	\mathcal{F} -stat	–	8.1	1.29 ^P	0.21 ^q	–	–	–	9.61	110.0 ^h	45.7	55.1	157
O2	J1747	5-vec	–	6.23	0.576	–	–	–	–	6.8	140.0 ^h	20.3	55.1	318
O2	J1809	5-vec	–	6.32	0.4	–	–	–	–	6.72	140.0 ^h	24.2	55.2	318
O2	Vela ⁿ	5-vec	–	6.2	0.972	–	–	–	–	7.17	140.0 ^h	22.4	55.2	318
O1	J1400	5-vec	–	6.15	0.707	–	–	–	–	6.86	140.0 ^k	64.1	55.3	316
O2	J1811	5-vec	–	6.4	0.752	–	–	–	–	7.15	140.0 ^h	30.9	55.5	318
O2	J2043	5-vec	–	6.23	0	–	–	–	–	6.23	160.0 ^h	20.8	55.8	318
O2	J1531	5-vec	–	6.32	0.275	–	–	–	–	6.6	160.0 ^h	23.7	55.9	318
O2	J1831	5-vec	–	6.4	0.0988	–	–	–	–	6.5	170.0 ^h	29.7	56.6	318
O2	J1838	5-vec	–	6.4	0.84	–	–	–	–	7.24	160.0 ^h	28.4	56.7	318
O2	J1427	\mathcal{F} -stat	Vtrbi	9.88	5.24	–	–	–	2.93	18.0	53.0 ^h	185.0	56.8	319
O2	J1913	5-vec	–	6.66	0.275	–	–	–	–	6.94	170.0 ^h	55.7	56.9	318
O2	J1524	5-vec	–	6.32	0.576	–	–	–	–	6.9	170.0 ^h	25.5	57.1	318
O2	J1617	5-vec	–	6.4	1.16	–	–	–	–	7.56	170.0 ^h	28.8	57.4	318
O2	J1833	5-vec	–	6.4	1.43	–	–	–	–	7.83	170.0 ^h	32.3	57.6	318
O2	J0540	5-vec	–	6.53	1.98	–	–	–	–	8.5	160.0 ^h	39.4	58.1	318
O1	J2043	5-vec	–	6.0	0.272	–	–	–	–	6.28	200.0 ^k	20.8	58.1	316
O2	J1112	5-vec	–	6.4	0.643	–	–	–	–	7.04	190.0 ^h	30.8	58.1	318
O2	J1813	5-vec	–	6.53	0.643	–	–	–	–	7.17	190.0 ^h	41.6	58.2	318
O2	J1747	5-vec	–	6.53	1.47	–	–	–	–	8.0	170.0 ^h	38.3	58.3	318
O2	J0537	\mathcal{F} -stat	–	9.1	5.53	2.12	–	–	–	16.8	75.0 ^r	–	58.8	158
O2	J1813	5-vec	–	6.58	1.51	–	–	–	–	8.09	180.0 ^h	44.7	58.9	318
O2	J1410	5-vec	–	6.53	0.945	–	–	–	–	7.47	200.0 ^h	40.0	59.3	318
O3	Crab ⁿ	\mathcal{F} -stat	–	6.95	2.46	–	–	–	–	9.41	170.0 ^d	59.2	59.4	136
O3	J1913	\mathcal{F} -stat	–	7.1	0.68	–	–	–	–	7.77	200.0 ^d	55.7	59.5	136
O2	J1952	5-vec	–	6.62	0.4	–	–	–	–	7.02	220.0 ^h	50.5	59.6	318
O2	J2229	5-vec	–	6.53	1.18	–	–	–	–	7.7	210.0 ^h	38.7	59.6	318
O3	J0537	\mathcal{F} -stat	–	8.79	2.42 ^P	0.948 ^q	–	–	–	12.2	130.0 ^d	93.9	59.7	106
O2	J2022	5-vec	–	6.53	1.27	–	–	–	–	7.8	200.0 ^h	41.1	59.7	318
O2	J1400	5-vec	–	6.74	1.32	–	–	–	–	8.05	200.0 ^h	64.1	59.8	318
O2	J1302	5-vec	–	6.53	0	–	–	–	–	6.53	240.0 ^h	41.9	59.8	318
O3	J1925	\mathcal{F} -stat	–	6.79	0.534	–	–	–	–	7.33	230.0 ^d	26.4	60.2	136
O3	Crab ⁿ	5-vec	–	6.95	2.36	–	–	–	–	9.31	190.0 ^d	59.2	60.3	136
O3	J1833	\mathcal{F} -stat	–	6.73	0.358	–	–	–	–	7.08	240.0 ^d	23.4	60.3	136
O3	J1809	\mathcal{F} -stat	–	6.74	0.835	–	–	–	–	7.57	230.0 ^d	24.2	60.4	136
O3	J1828	\mathcal{F} -stat	–	6.79	0.719	–	–	–	–	7.51	230.0 ^d	27.8	60.5	136
O2	J1105	5-vec	–	6.4	0.4	–	–	–	–	6.8	250.0 ^h	31.6	60.5	318
O1	J2022	5-vec	–	5.91	0.668	–	–	–	–	6.58	250.0 ^k	41.2	60.5	316
O3	J1105 ⁿ	\mathcal{F} -stat	–	6.85	0.838	–	–	–	–	7.69	230.0 ^d	31.6	60.6	136
O2	J1300	5-vec	–	7.43	0	–	–	–	–	7.43	240.0 ^h	321.5	60.8	318
O3	J1952	\mathcal{F} -stat	–	7.05	0.835	–	–	–	–	7.89	230.0 ^d	50.6	60.8	136
O3	Vela	\mathcal{F} -stat	–	6.7	1.44	–	–	–	–	8.14	220.0 ^d	22.4	60.9	136
O3	J1101	\mathcal{F} -stat	–	6.87	0.613	–	–	–	–	7.48	240.0 ^d	31.8	60.9	136
O3	J2229	\mathcal{F} -stat	–	6.96	1.77	–	–	–	–	8.73	210.0 ^d	38.7	61.0	136

Table A.3 continued.

Obs.	Target ^a	Algorithm ^b		Breadth						Depth		Vol.	Ref.	
		Coh.	Inc.	\mathcal{B}_f	\mathcal{B}_j	$\mathcal{B}_{\dot{f}}$	\mathcal{B}_{sky}	\mathcal{B}_{bin}	\mathcal{B}_{HMM}	\mathcal{B}	\mathcal{D}			$f_{\mathcal{D}}$
				lg	lg	lg	lg	lg	lg	lg		Hz	lg	
O3	J1935	\mathcal{F} -stat	–	6.75	1.24	–	–	–	–	7.99	240.0 ^d	25.0	61.3	136
O3	J1928	\mathcal{F} -stat	–	6.83	0.7	–	–	–	–	7.53	250.0 ^d	29.1	61.4	136
O3	J1813	\mathcal{F} -stat	–	7.01	2.07	–	–	–	–	9.07	210.0 ^d	44.7	61.4	136
O2	J1420	5-vec	–	6.4	1.1	–	–	–	–	7.5	250.0 ^h	29.3	61.5	318
O3	J1838	\mathcal{F} -stat	–	6.79	1.26	–	–	–	–	8.05	240.0 ^d	28.4	61.5	136
O3	J1828	5-vec	–	6.79	0.719	–	–	–	–	7.51	260.0 ^d	27.8	61.6	136
O3	J2124	\mathcal{F} -stat	–	7.96	0	–	–	–	–	7.96	250.0 ^d	405.6	61.6	136
O2	J0537	5-vec	–	7.02	2.0	–	–	–	–	9.02	220.0 ^h	123.9	61.6	318
O3	J0711	\mathcal{F} -stat	–	7.93	0	–	–	–	–	7.93	250.0 ^d	364.2	61.8	136
O3	Vela	5-vec	–	6.7	1.47	–	–	–	–	8.17	250.0 ^d	22.4	61.9	136
O3	J1913	5-vec	–	7.1	0.719	–	–	–	–	7.81	260.0 ^d	55.7	62.1	136
O3	J1833	5-vec	–	6.73	0.399	–	–	–	–	7.12	280.0 ^d	23.4	62.2	136
O3	J1101	5-vec	–	6.87	0.636	–	–	–	–	7.5	280.0 ^d	31.8	62.3	136
O3	J1105 ^u	5-vec	–	6.85	0.838	–	–	–	–	7.69	270.0 ^d	31.6	62.4	136
O3	J1838	5-vec	–	6.79	1.28	–	–	–	–	8.07	260.0 ^d	28.4	62.4	136
O3	J1809	5-vec	–	6.74	0.863	–	–	–	–	7.6	280.0 ^d	24.2	62.5	136
O2	J2124	5-vec	–	7.53	0	–	–	–	–	7.53	280.0 ^h	405.6	62.5	318
O3	J1925	5-vec	–	6.79	0.534	–	–	–	–	7.33	290.0 ^d	26.4	62.7	136
O3	J2229	5-vec	–	6.93	1.74	–	–	–	–	8.67	260.0 ^d	38.7	62.8	136
O3	J0537	5-vec	–	8.79	2.42 ^P	0.948 ^q	–	–	–	12.2	180.0 ^d	94.5	62.8	106
O3	J1856	5-vec	–	6.75	1.26	–	–	–	–	8.0	280.0 ^d	24.7	62.9	136
O3	J0711	5-vec	–	7.61	0	–	–	–	–	7.61	290.0 ^d	364.2	62.9	136
O3	J1935	5-vec	–	6.72	1.26	–	–	–	–	7.97	290.0 ^d	25.0	63.2	136
O3	J2124	5-vec	–	7.71	0	–	–	–	–	7.71	300.0 ^d	405.6	63.3	136
O3	J1928	5-vec	–	6.83	0.719	–	–	–	–	7.55	310.0 ^d	29.1	63.6	136
O3	J1952	5-vec	–	7.05	0.863	–	–	–	–	7.92	300.0 ^d	50.6	63.7	136
O3	J1813	5-vec	–	7.01	2.07	–	–	–	–	9.08	270.0 ^d	44.7	63.8	136
Directed searches for central compact objects (“CCOs”)														
S6	Vela Jr.	\mathcal{F} -stat	–	9.22	3.29 ^P	0 ^q	–	–	–	12.5	26.0 ^c	–	33.6	320
S6	G1.9	\mathcal{F} -stat	–	8.32	3.91 ^P	0 ^q	–	–	–	12.2	28.0 ^c	–	33.8	320
S6	Cas A	\mathcal{F} -stat	–	8.8	3.56 ^P	0 ^q	–	–	–	12.4	32.0 ^c	–	34.7	320
S6	G347.3	\mathcal{F} -stat	–	9.14	3.2 ^P	0 ^q	–	–	–	12.3	32.0 ^c	–	34.8	320
S6	G350.1	\mathcal{F} -stat	–	8.59	3.56 ^P	0 ^q	–	–	–	12.1	36.0 ^c	–	35.3	320
S6	G189.1	\mathcal{F} -stat	–	9.01	3.15 ^P	0 ^q	–	–	–	12.2	39.0 ^c	–	35.9	320
S6	Vela Jr.	\mathcal{F} -stat	–	9.23	3.0 ^P	0 ^q	–	–	–	12.2	41.0 ^c	–	36.2	320
S6	G18.9	\mathcal{F} -stat	–	8.82	3.16 ^P	0 ^q	–	–	–	12.0	44.0 ^c	–	36.5	320
S6	G291.0	\mathcal{F} -stat	–	8.71	3.4 ^P	0 ^q	–	–	–	12.1	44.0 ^c	–	36.6	320
S6	G93.3	\mathcal{F} -stat	–	8.98	3.08 ^P	0 ^q	–	–	–	12.1	50.0 ^c	–	37.3	320
O3	G18.9	\mathcal{F} -stat	Vtrbi	10.6	6.25	–	–	–	3.36	20.2	6.1 ^s	210.7	37.9	87
O3	G189.1	\mathcal{F} -stat	Vtrbi	10.8	6.36	–	–	–	3.5	20.6	6.6 ^s	225.9	39.0	87
O3	G347.3	\mathcal{F} -stat	Vtrbi	10.7	6.65	–	–	–	3.64	21.0	6.9 ^s	206.9	39.9	87
O3	G1.9	\mathcal{F} -stat	Vtrbi	9.41	6.65	–	–	–	3.64	19.7	8.0 ^s	167.0	39.9	87
O3	G354.4	\mathcal{F} -stat	Vtrbi	9.44	6.65	–	–	–	3.64	19.7	8.0 ^s	167.0	40.0	87
O3	G39.2	\mathcal{F} -stat	Vtrbi	10.1	6.36	–	–	–	3.2	19.6	8.2 ^s	230.8	40.1	87
O3	G111.7	\mathcal{F} -stat	Vtrbi	9.99	6.65	–	–	–	3.64	20.3	8.0 ^s	167.0	40.5	87
O3	G330.2	\mathcal{F} -stat	Vtrbi	10.5	6.65	–	–	–	3.6	20.7	7.7 ^s	205.6	40.6	87
O3	G15.9	\mathcal{F} -stat	Vtrbi	10.2	6.65	–	–	–	3.64	20.5	8.0 ^s	167.0	40.8	87
O3	G350.1	\mathcal{F} -stat	Vtrbi	10.3	6.65	–	–	–	3.64	20.6	8.0 ^s	167.0	40.8	87
O3	G266.2	\mathcal{F} -stat	Vtrbi	10.4	6.65	–	–	–	3.64	20.7	8.0 ^s	167.0	40.9	87
O3	G291.0	\mathcal{F} -stat	Vtrbi	10.6	6.65	–	–	–	3.64	20.9	8.0 ^s	167.0	41.1	87
S5	Cas A	\mathcal{F} -stat	–	8.58	3.65 ^P	0 ^q	–	–	–	12.2	36.0 ^c	–	41.6	245

Table A.3 continued.

Obs.	Target ^a	Algorithm ^b		Breadth							Depth		Vol.	Ref.
		Coh.	Inc.	\mathcal{B}_f	\mathcal{B}_j	\mathcal{B}_f	\mathcal{B}_{sky}	\mathcal{B}_{bin}	\mathcal{B}_{HMM}	\mathcal{B}	\mathcal{D}	$f_{\mathcal{D}}$		
				lg	lg	lg	lg	lg	lg	lg		Hz	lg	
O1	G354.4	\mathcal{F} -stat	–	8.95	3.68 ^P	0 ^q	–	–	–	12.6	20.0 ^k	176.0	42.1	321
O3	G39.2	\mathcal{F} -stat	Vtrbi	9.06	4.14	–	–	–	2.69	15.9	15.0 ^s	248.0	42.4	87
O1	G1.9	\mathcal{F} -stat	–	8.9	3.68 ^P	0 ^q	–	–	–	12.6	22.0 ^k	171.0	42.6	321
O3	G18.9	\mathcal{F} -stat	Vtrbi	9.37	4.14	–	–	–	2.69	16.2	15.0 ^s	248.0	42.7	87
O3	G93.3	\mathcal{F} -stat	Vtrbi	9.46	4.14	–	–	–	2.69	16.3	15.0 ^s	248.0	42.8	87
O3	G266.2	\mathcal{F} -stat	Vtrbi	9.47	4.14	–	–	–	2.69	16.3	15.0 ^s	248.0	42.8	87
O3	G39.2	\mathcal{F} -stat	Vtrbi	9.36	4.45	–	–	–	2.69	16.5	15.0 ^s	248.0	43.0	87
O3	G18.9	\mathcal{F} -stat	Vtrbi	9.67	4.45	–	–	–	2.69	16.8	15.0 ^s	248.0	43.3	87
O3	G93.3	\mathcal{F} -stat	Vtrbi	9.76	4.45	–	–	–	2.69	16.9	15.0 ^s	248.0	43.4	87
O3	G266.2	\mathcal{F} -stat	Vtrbi	9.77	4.45	–	–	–	2.69	16.9	15.0 ^s	248.0	43.4	87
O1	G266.2	\mathcal{F} -stat	–	9.22	3.29 ^P	0 ^q	–	–	–	12.5	24.0 ^k	201.0	43.5	321
O3	G65.7	\mathcal{F} -stat	Vtrbi	10.5	5.57	–	–	–	2.97	19.0	13.0 ^s	235.7	44.0	87
O3	G189.1	\mathcal{F} -stat	Vtrbi	9.92	3.89	–	–	–	2.56	16.4	17.0 ^s	318.0	44.1	87
O3	G65.7	\mathcal{F} -stat	Vtrbi	9.92	3.89	–	–	–	2.56	16.4	17.0 ^s	318.0	44.1	87
O3	G353.6	\mathcal{F} -stat	Vtrbi	10.1	3.89	–	–	–	2.56	16.5	17.0 ^s	318.0	44.2	87
O3	G93.3	\mathcal{F} -stat	Vtrbi	10.7	6.19	–	–	–	3.36	20.2	12.0 ^s	240.8	44.2	87
O1	G347.3	\mathcal{F} -stat	–	9.32	3.12 ^P	0 ^q	–	–	–	12.4	27.0 ^k	175.0	44.4	321
O3	G189.1	\mathcal{F} -stat	Vtrbi	10.2	4.2	–	–	–	2.56	17.0	17.0 ^s	318.0	44.7	87
O3	G65.7	\mathcal{F} -stat	Vtrbi	10.2	4.2	–	–	–	2.56	17.0	17.0 ^s	318.0	44.7	87
O3	G353.6	\mathcal{F} -stat	Vtrbi	10.4	4.2	–	–	–	2.56	17.1	17.0 ^s	318.0	44.8	87
O1	G266.2	\mathcal{F} -stat	–	9.46	2.9 ^P	0 ^q	–	–	–	12.4	29.0 ^k	159.0	45.3	321
O1	G15.9	\mathcal{F} -stat	–	8.88	3.44 ^P	0 ^q	–	–	–	12.3	30.0 ^k	172.0	45.4	321
O1	G350.1	\mathcal{F} -stat	–	9.06	3.35 ^P	0 ^q	–	–	–	12.4	30.0 ^k	173.0	45.4	321
O1	G354.4	\mathcal{F} -stat	–	8.91	3.43 ^P	0 ^q	–	–	–	12.3	30.0 ^k	210.0	45.5	321
O1	G18.9	\mathcal{F} -stat	–	9.29	2.97 ^P	0 ^q	–	–	–	12.3	31.0 ^k	175.0	45.6	321
O1	G291.0	\mathcal{F} -stat	–	9.13	3.22 ^P	0 ^q	–	–	–	12.3	31.0 ^k	210.0	45.7	321
O1	G189.1	\mathcal{F} -stat	–	9.34	3.02 ^P	0 ^q	–	–	–	12.4	31.0 ^k	195.0	45.9	321
O2	SN 1987A	\mathcal{F} -stat	–	8.31	4.37 ^P	0.597 ^q	–	–	–	13.3	29.0 ^r	–	46.1	322
O3	G353.6	\mathcal{F} -stat	Vtrbi	9.84	5.43	–	–	–	2.64	17.9	18.0 ^s	231.8	46.2	87
O1	G93.3	\mathcal{F} -stat	–	9.35	2.93 ^P	0 ^q	–	–	–	12.3	33.0 ^k	167.0	46.2	321
O1	G111.7	\mathcal{F} -stat	–	9.44	4.1 ^P	0 ^q	–	–	–	13.5	30.0 ^k	172.0	46.8	321
O2	G1.9	\mathcal{F} -stat	–	8.4	3.74 ^P	0 ^q	–	–	–	12.1	35.0 ^h	134.0	46.8	323
O1	G330.2	\mathcal{F} -stat	–	9.02	3.25 ^P	0 ^q	–	–	–	12.3	35.0 ^k	196.0	46.8	321
O2	G354.4	\mathcal{F} -stat	–	8.41	3.74 ^P	0 ^q	–	–	–	12.1	37.0 ^h	127.0	47.5	323
O1	G39.2	\mathcal{F} -stat	–	8.85	3.19 ^P	0 ^q	–	–	–	12.0	38.0 ^k	201.0	47.6	321
O1	G65.7	\mathcal{F} -stat	–	9.41	2.69 ^P	0 ^q	–	–	–	12.1	39.0 ^k	215.0	47.9	321
O2	SN 1987A	\mathcal{F} -stat	–	8.0	4.4 ^P	0.779 ^q	–	–	–	13.2	36.0 ^r	–	48.1	322
S6	Cas A	\mathcal{F} -stat	GCT	10.6	6.8 ^P	3.4 ^q	–	–	–	20.8	73.0 ^c	–	48.5	324
O1	G189.1	\mathcal{F} -stat	–	9.42	2.69 ^P	0 ^q	–	–	–	12.1	42.0 ^k	187.0	48.5	321
O2	G354.4	\mathcal{F} -stat	–	8.62	3.47 ^P	0 ^q	–	–	–	12.1	45.0 ^h	134.0	49.2	323
O1	Fom. b	\mathcal{F} -stat	–	9.95	2.09 ^P	0 ^q	–	–	–	12.0	46.0 ^k	160.0	49.3	321
O2	G15.9	\mathcal{F} -stat	–	8.63	3.46 ^P	0 ^q	–	–	–	12.1	46.0 ^h	133.0	49.4	323
O2	G350.1	\mathcal{F} -stat	–	8.64	3.44 ^P	0 ^q	–	–	–	12.1	46.0 ^h	134.0	49.5	323
O2	G330.2	\mathcal{F} -stat	–	8.7	3.33 ^P	0 ^q	–	–	–	12.0	53.0 ^h	131.0	50.7	323
O2	G39.2	\mathcal{F} -stat	–	8.83	3.1 ^P	0 ^q	–	–	–	11.9	55.0 ^h	134.0	51.0	323
O2	G15.9	\mathcal{F} -stat	–	8.8	3.16 ^P	0 ^q	–	–	–	12.0	56.0 ^h	135.0	51.3	323
O2	G291.0	\mathcal{F} -stat	–	8.72	3.3 ^P	0 ^q	–	–	–	12.0	57.0 ^h	133.0	51.4	323
O1	G353.6	\mathcal{F} -stat	–	8.99	2.82 ^P	0 ^q	–	–	–	11.8	59.0 ^k	195.0	51.6	321
O2	G189.1	\mathcal{F} -stat	–	8.83	3.11 ^P	0 ^q	–	–	–	11.9	59.0 ^h	125.0	51.6	323
O2	G18.9	\mathcal{F} -stat	–	8.87	3.02 ^P	0 ^q	–	–	–	11.9	60.0 ^h	133.0	51.9	323
O2	G330.2	\mathcal{F} -stat	–	8.83	3.11 ^P	0 ^q	–	–	–	11.9	61.0 ^h	136.0	52.1	323

Table A.3 continued.

Obs.	Target ^a	Algorithm ^b		Breadth							Depth		Vol.	Ref.
		Coh.	Inc.	\mathcal{B}_f	\mathcal{B}_j	\mathcal{B}_f	\mathcal{B}_{sky}	\mathcal{B}_{bin}	\mathcal{B}_{HMM}	\mathcal{B}	\mathcal{D}	$f_{\mathcal{D}}$		
				lg	lg	lg	lg	lg	lg	lg		Hz	lg	
O2	G93.3	\mathcal{F} -stat	–	8.88	2.98 ^P	0 ^q	–	–	–	11.9	64.0 ^h	134.0	52.3	323
O1	Fom. b	\mathcal{F} -stat	–	10.2	1.65 ^P	0 ^q	–	–	–	11.9	69.0 ^k	224.0	53.2	321
O2	G65.7	\mathcal{F} -stat	–	9.04	2.7 ^P	0 ^q	–	–	–	11.7	71.0 ^h	136.0	53.3	323
O2	G189.1	\mathcal{F} -stat	–	9.04	2.71 ^P	0 ^q	–	–	–	11.7	73.0 ^h	147.0	53.5	323
O2	G353.6	\mathcal{F} -stat	–	9.07	2.64 ^P	0 ^q	–	–	–	11.7	74.0 ^h	133.0	53.6	323
O2	Fom. b	\mathcal{F} -stat	Vtrbi	10.6	2.53	–	–	–	1.44	14.5	73.0 ^h	195.1	56.3	325
O3	G353.6	pwr	FrHgh	10.5	3.88	–	–	–	2.74	17.1	72.0 ^s	206.7	58.7	87
S5	SN 1987A	pwr	XCorr	10.3	14.5 ^P	–	–	–	–	24.8	64.0 ^m	150.0	59.1	326
O3	G189.1	pwr	FrHgh	10.2	4.83	–	–	–	2.74	17.8	70.0 ^s	206.7	59.3	87
O3	G18.9	pwr	FrHgh	10.5	4.66	–	–	–	2.74	17.9	71.0 ^s	207.7	59.4	87
O3	G266.2	pwr	FrHgh	10.2	4.83	–	–	–	2.74	17.8	73.0 ^s	206.7	59.6	87
O3	G93.3	pwr	FrHgh	10.5	4.61	–	–	–	2.74	17.8	74.0 ^s	153.7	59.7	87
O1	Cas A	\mathcal{F} -stat	GCT	10.5	6.33 ^P	2.98 ^q	–	–	–	19.8	60.0 ^r	–	59.8	327
O3	G65.7	pwr	FrHgh	10.2	4.83	–	–	–	2.74	17.8	77.0 ^s	206.7	60.1	87
O3	G39.2	pwr	FrHgh	10.5	4.64	–	–	–	2.74	17.8	78.0 ^s	206.7	60.3	87
O1	G347.3	\mathcal{F} -stat	GCT	10.5	5.64 ^P	1.61 ^q	–	–	–	17.7	83.0 ^r	–	60.8	327
O1	Vela Jr.	\mathcal{F} -stat	GCT	10.5	6.0 ^P	2.33 ^q	–	–	–	18.8	76.0 ^r	–	61.1	327
O3	Cas A	\mathcal{F} -stat	Weave	10.4	6.49 ^P	2.98 ^q	–	–	–	19.9	72.0 ^r	–	61.7	137
O3	Vela Jr.	\mathcal{F} -stat	Weave	10.4	6.12 ^P	2.24 ^q	–	–	–	18.8	81.0 ^r	–	61.7	137
Directed searches for low-mass X-ray binaries (“LMXBs”)														
S2	Sco X-1	\mathcal{F} -stat	–	7.05	–	–	–	2.06	–	9.12	4.1 ^c	–	17.9	84
S6	Sco X-1	pwr	2Spect	9.38	–	–	–	4.79	–	14.2	8.2 ^c	–	27.8	328
S6	Sco X-1	pwr	2Spect	9.47	–	–	–	5.07	–	14.5	8.2 ^c	–	28.1	328
S5	Sco X-1	\mathcal{F} -stat	–	8.78	–	–	–	3.92 ^t	–	12.7	8.1 ^c	–	29.9	329
S6	Sco X-1	pwr	2Spect	11.0	–	–	–	9.2	–	20.2	5.7 ^c	–	31.5	330
S6	J1751	pwr	2Spect	10.2	–	–	–	8.85	–	19.0	9.4 ^c	–	33.5	330
O1	Sco X-1	\mathcal{F} -stat	Vtrbi	9.97	–	–	–	8.36	1.11	19.4	7.6 ^c	–	39.2	331
O3	J1749.4	\mathcal{F} -stat	Vtrbi	8.5	–	–	–	-4.69	1.56	5.37	41.0 ^d	690.6	41.5	141
O3	J17591	\mathcal{F} -stat	Vtrbi	8.3	–	–	–	-8.07	1.56	1.8	65.0 ^d	703.2	42.5	141
O3	J17062	\mathcal{F} -stat	Vtrbi	7.92	–	–	–	-10.9	1.56	-1.38	100.0 ^d	327.3	44.0	141
O3	J17379	\mathcal{F} -stat	Vtrbi	8.24	–	–	–	-6.16	1.56	3.64	68.0 ^d	468.1	44.8	141
O3	J1748.9	\mathcal{F} -stat	Vtrbi	8.58	–	–	–	-5.14	1.56	5.0	59.0 ^d	442.4	44.8	141
O3	J17498	\mathcal{F} -stat	Vtrbi	8.34	–	–	–	-7.17	1.56	2.73	76.0 ^d	401.0	45.0	141
O3	J1756.9	\mathcal{F} -stat	Vtrbi	8.23	–	–	–	-4.26	1.56	5.53	59.0 ^d	182.1	45.4	141
O3	J1807	\mathcal{F} -stat	Vtrbi	8.13	–	–	–	-8.05	1.56	1.64	93.0 ^d	381.2	45.8	141
O3	J17494	\mathcal{F} -stat	Vtrbi	8.34	–	–	–	-3.94	1.56	5.96	62.0 ^d	376.1	46.2	141
O3	J00291	\mathcal{F} -stat	Vtrbi	8.55	–	–	–	-8.75	1.56	1.35	100.0 ^d	798.5	46.3	141
O3	J17511	\mathcal{F} -stat	Vtrbi	8.3	–	–	–	-7.07	1.56	2.79	88.0 ^d	489.7	46.5	141
O3	J1814	\mathcal{F} -stat	Vtrbi	8.15	–	–	–	-7.51	1.56	2.19	94.0 ^d	628.7	46.5	141
O3	J1808.4	\mathcal{F} -stat	Vtrbi	8.23	–	–	–	-6.72	1.56	3.07	87.0 ^d	534.6	46.6	141
O3	J18245	\mathcal{F} -stat	Vtrbi	8.16	–	–	–	-5.63	1.56	4.09	80.0 ^d	339.1	46.8	141
O3	J1900.1	\mathcal{F} -stat	Vtrbi	8.11	–	–	–	-7.02	1.56	2.65	95.0 ^d	377.3	47.0	141
O3	NGC 6440	\mathcal{F} -stat	Vtrbi	8.83	–	–	–	-5.37	1.56	5.02	74.0 ^d	205.9	47.0	141
O3	J0929	\mathcal{F} -stat	Vtrbi	7.96	–	–	–	-6.13	1.56	3.39	90.0 ^d	246.8	47.2	141
O2	Sco X-1	\mathcal{F} -stat	Vtrbi	10.3	–	–	–	6.59	1.43	18.3	20.0 ^h	194.6	47.6	332
O3	J0911	\mathcal{F} -stat	Vtrbi	8.54	–	–	–	-5.76	1.56	4.34	92.0 ^d	680.0	48.4	141
O3	J1751	\mathcal{F} -stat	Vtrbi	8.37	–	–	–	-4.61	1.56	5.31	84.0 ^d	870.6	48.5	141
O3	J16597	\mathcal{F} -stat	Vtrbi	8.14	–	–	–	-3.35	1.56	6.35	85.0 ^d	210.4	49.6	141
O1	Sco X-1	pwr	XCorr	10.5	–	–	–	8.47	–	18.9	24.0 ^c	–	49.9	333
O2	Sco X-1	5-vec	–	9.76	–	–	–	-0.77	–	8.99	68.0 ^u	154.5	50.1	173
O3	Sco X-1	pwr	XCorr	10.8	–	–	–	8.08	–	18.9	39.0 ^d	153.2	54.6	139

Table A.3 continued.

Obs.	Target ^a	Algorithm ^b		Breadth							Depth		Vol.	Ref.
		Coh.	Inc.	\mathcal{B}_f	\mathcal{B}_j	\mathcal{B}_f	\mathcal{B}_{sky}	\mathcal{B}_{bin}	\mathcal{B}_{HMM}	\mathcal{B}	\mathcal{D}	$f_{\mathcal{D}}$		
				lg	lg	lg	lg	lg	lg	lg	Hz	lg		
O2	Sco X-1	pwr	XCorr	9.73	–	–	–	5.5	–	15.2	57.0 ^h	153.2	54.7	83
O3	Sco X-1	\mathcal{F} -stat	Vtrbi	10.3	–	–	–	5.7	1.56	17.6	50.0 ^d	256.1	55.7	138
Searches directed at interesting regions of the sky (“Regions”)														
S6	NGC 6544	\mathcal{F} -stat	–	8.92	3.7 ^P	0 ^q	–	–	–	12.6	30.0 ^c	–	34.5	334
S6	Orion Arm	pwr	PFlxLC	10.6	5.67	–	10.5	–	–	26.7	37.0 ^v	–	50.0	335
S5	G.C.	\mathcal{F} -stat	GCT	10.7	7.59 ^P	–	–	–	–	18.2	72.0 ^c	–	53.5	336
O2	G.C.	pwr	FrHgh	10.5	5.36 ^P	–	–	–	–	15.8	51.0 ^h	160.0	54.3	205
O3	G.C.	pwr	FrHgh	11.1	6.51 ^P	–	–	–	–	17.6	78.0 ^d	142.0	60.0	144
O1	Trz 5, G.C.	pwr	PFlxLC	10.3	5.96	–	9.57	–	–	25.8	48.0 ^w	475.6	63.6	337
All sky searches for isolated neutron stars (“All sky 1”)														
S2	–	\mathcal{F} -stat	–	7.52	0	–	10.8	–	–	18.3	5.5 ^c	–	28.9	84
S4	–	pwr	PFlx	9.5	4.17	–	10.4	–	–	24.1	8.2 ^v	–	37.2	100
S4	–	\mathcal{F} -stat	coinc	9.67	3.64 ^P	–	10.8	–	–	24.1	8.5 ^c	–	37.4	195
S4	–	pwr	SSlide	9.5	4.17	–	10.4	–	–	24.1	10.0 ^c	–	38.7	100
S2	–	pwr	SkHgh	9.39	3.83	–	10.5	–	–	23.7	11.0 ^c	–	38.8	338
S4	–	pwr	SkHgh	9.5	4.17	–	10.4	–	–	24.1	13.0 ^c	–	40.3	100
S5	–	\mathcal{F} -stat	coinc	10.0	4.5 ^P	–	11.8	–	–	26.3	11.0 ^c	–	46.0	339
VSR4	–	pwr	FrHgh	10.0	5.1	–	11.2	–	–	26.3	36.0 ^c	–	49.4	340
S6	–	pwr	PFlx	10.6	6.31	–	13.2	–	–	30.1	22.0 ^v	–	50.1	341
S6	–	\mathcal{F} -stat	GCT	10.2	5.54	–	12.3	–	–	28.0	37.0 ^c	–	51.3	342
O1	–	\mathcal{F} -stat	coinc	10.4	5.51	–	12.9	–	–	28.8	11.0 ^c	–	52.1	343
VSR1	–	\mathcal{F} -stat	coinc	10.2	5.45 ^P	–	12.3	–	–	28.0	23.0 ^c	–	53.6	344
S5	–	pwr	PFlx	10.5	5.71	–	12.9	–	–	29.1	20.0 ^v	–	53.8	345
O1	–	pwr	SkHgh	10.4	5.51	–	12.9	–	–	28.8	17.0 ^c	–	56.3	343
O1	–	pwr	FrHgh	9.82	5.51	–	11.6	–	–	27.0	21.0 ^c	–	56.8	104
S5	–	pwr	SkHgh	10.9	5.88	–	13.0	–	–	29.7	28.0 ^c	–	57.2	346
O1	–	pwr	SkHgh	9.82	5.51	–	11.6	–	–	27.0	22.0 ^c	–	57.3	104
O1	–	pwr	PFlx	9.82	5.51	–	11.6	–	–	27.0	24.0 ^v	–	57.8	104
O1	–	\mathcal{F} -stat	coinc	9.82	5.51	–	11.6	–	–	27.0	24.0 ^c	–	57.8	104
S5	–	\mathcal{F} -stat	SkHgh	11.0	6.25	–	13.1	–	–	30.4	30.0 ^c	–	58.3	201
S5	–	pwr	PFlx	10.7	6.71	–	12.7	–	–	30.2	31.0 ^v	–	58.4	347
O1	–	pwr	PFlxLC	9.45	5.51	–	10.9	–	–	25.8	29.0 ^c	–	58.6	229
S5	–	\mathcal{F} -stat	GCT	10.9	6.47	–	13.1	–	–	30.5	31.0 ^c	–	58.7	348
O1	–	pwr	PFlx	10.4	5.51	–	12.9	–	–	28.8	22.0 ^v	–	59.0	343
O1	–	\mathcal{F} -stat	GCT	9.15	4.93	–	10.3	–	–	24.3	49.0 ^c	–	62.2	349
O2	–	\mathcal{F} -stat	Weave	9.11	1.53	–	10.2	–	–	20.9	71.0 ^h	171.5	62.4	246
O1	–	pwr	PFlxLC	9.92	5.51	–	11.8	–	–	27.2	37.0 ^k	202.6	62.5	350
O3	–	pwr	SOAP	10.9	6.41 ^P	–	13.6	–	4.24	35.1	18.0 ^d	158.0	63.4	88
O2	–	pwr	SkHgh	10.6	6.18	–	13.3	–	–	30.1	32.0 ^h	171.0	63.8	351
O3	–	pwr	PFlx	10.6	5.81	–	13.2	–	–	29.6	34.0 ^s	200.0	64.0	86
O2	–	\mathcal{F} -stat	coinc	10.7	6.18	–	13.3	–	–	30.1	33.0 ^h	89.4	64.2	351
O3	–	pwr	PFlxLC	10.3	3.77	–	12.6	–	–	26.6	57.0 ^s	523.3	66.0	352
O3	–	pwr	SkHgh	10.1	5.36	–	12.1	–	–	27.6	53.0 ^d	153.1	66.4	88
O3	–	\mathcal{F} -stat	coinc	10.5	5.37 ^P	–	12.7	–	–	28.6	49.0 ^d	157.8	66.5	88
O2	–	pwr	PFlxLC	10.2	1.88	–	12.3	–	–	24.4	77.0 ^h	170.0	66.6	353
O2	–	pwr	PFlxLC	10.7	2.83 ^P	–	13.4	–	–	26.9	62.0 ^h	518.5	67.1	354
O2	–	\mathcal{F} -stat	GCT	10.2	5.56	–	12.5	–	–	28.2	56.0 ^r	–	67.5	355
O2	–	pwr	FrHgh	10.5	6.0 ^P	–	12.9	–	–	29.4	52.0 ^h	122.5	67.9	351
O3	–	pwr	FrHgh	10.9	6.4	–	13.6	–	–	30.9	56.0 ^d	112.0	70.1	88
All-sky searches for neutron stars in binary systems (“All sky 2”)														
S6	–	pwr	2Spect	9.72	–	–	11.0	14.3 ^x	–	35.0	3.2 ^c	–	42.5	328

Table A.3 continued.

Obs.	Target ^a	Algorithm ^b		Breadth						Depth		Vol.	Ref.	
		Coh.	Inc.	\mathcal{B}_f lg	$\mathcal{B}_{\dot{f}}$ lg	$\mathcal{B}_{\ddot{f}}$ lg	\mathcal{B}_{sky} lg	\mathcal{B}_{bin} lg	\mathcal{B}_{HMM} lg	\mathcal{B} lg	\mathcal{D}			$f_{\mathcal{D}}$ Hz
S6	–	pwr	2Spect	10.4	–	–	12.4	15.0 ^x	–	37.9	3.2 ^c	–	45.4	328
O3	–	\mathcal{F} -stat	BShgh	10.0	–	–	12.1	16.0	–	38.1	18.0 ^r	–	66.0	152
O2	–	pwr	BShgh	9.97	–	–	11.9	15.4	–	37.3	21.0 ^h	195.1	66.8	356
O3	–	pwr	BShgh	10.0	–	–	12.1	16.0	–	38.1	23.0 ^r	–	68.7	151

Notes to Table A.3.

- a. Abbreviations: “G.C.”: Galactic centre. Names of astronomical objects have also been abbreviated; see the reference for the full identifiers.
- b. Abbreviations: “ \mathcal{F} -stat”: \mathcal{F} -statistic, “2Spect”: TwoSpect, “5-vec”: 5-vectors, “Bayes”: Bayesian, “BShgh”: BinarySkyHough, “coinc”: coincidence, “FrHgh”: FrequencyHough, “GCT”: Global Correlation Transform, “PFlx”: PowerFlux (classic), “PFlxLC”: PowerFlux (loosely coherent), “pwr”: power, “SkHgh”: SkyHough, “SOAP”: Hidden Markov Model (SOAP), “SSlide”: StackSlide, “Vtrbi”: Hidden Markov Model (Viterbi), “XCorr”: CrossCorr.
- c. \mathcal{D} taken from [99].
- d. \mathcal{D} derived from $h_0(f_{\mathcal{D}})$ upper limit quoted in reference and S_h for O3 [112, 113] in a 1 Hz band around $f_{\mathcal{D}}$.
- e. \mathcal{D} derived from $h_0(f_{\mathcal{D}})$ upper limit quoted in reference and S_h for O1 [110], O2 [111] in a 1 Hz band around $f_{\mathcal{D}}$.
- f. \mathcal{D} derived from $h_0(f_{\mathcal{D}})$ upper limit quoted in reference and S_h for VSR2 [108] in a 1 Hz band around $f_{\mathcal{D}}$.
- g. \mathcal{D} derived from $h_0(f_{\mathcal{D}})$ upper limit quoted in reference and S_h for S6 [108], VSR2 [108], VSR4 [109] in a 1 Hz band around $f_{\mathcal{D}}$.
- h. \mathcal{D} derived from $h_0(f_{\mathcal{D}})$ upper limit quoted in reference and S_h for O2 [111] in a 1 Hz band around $f_{\mathcal{D}}$.
- i. \mathcal{D} derived from $h_0(f_{\mathcal{D}})$ upper limit quoted in reference and S_h for O2 [111], O3 [112, 113] in a 1 Hz band around $f_{\mathcal{D}}$.
- j. \mathcal{D} derived from $h_0(f_{\mathcal{D}})$ upper limit quoted in reference and S_h for O1 [110], O2 [111], O3a [112, 113], O3b [112, 113] in a 1 Hz band around $f_{\mathcal{D}}$.
- k. \mathcal{D} derived from $h_0(f_{\mathcal{D}})$ upper limit quoted in reference and S_h for O1 [110] in a 1 Hz band around $f_{\mathcal{D}}$.
- l. \mathcal{D} derived from $h_0(f_{\mathcal{D}})$ upper limit quoted in reference and S_h for O3a [112, 113], O3b [112, 113] in a 1 Hz band around $f_{\mathcal{D}}$.
- m. \mathcal{D} derived from $h_0(f_{\mathcal{D}})$ upper limit quoted in reference and S_h for S5 [107] in a 1 Hz band around $f_{\mathcal{D}}$.
- n. Known pulsar search conducted after a glitch; see the reference for details.
- o. Known pulsar search conducted prior to a glitch; see the reference for details.
- p. $B_{\dot{f}}$ computed from integral form of Eq. (63) over non-rectangular \dot{f} parameter space.
- q. $B_{\ddot{f}}$ computed from integral form of Eq. (64) over non-rectangular \ddot{f} parameter space.
- r. \mathcal{D} taken from reference.
- s. \mathcal{D} derived from $h_0(f_{\mathcal{D}})$ upper limit quoted in reference and S_h for O3a [112, 113] in a 1 Hz band around $f_{\mathcal{D}}$.
- t. \mathcal{B}_{bin} computed with range of t_{asc} taken from [185].
- u. \mathcal{D} derived from $H_0(f_{\mathcal{D}})$ upper limit quoted in reference, converted to h_0 using their Eq. (5) and averaged over $\cos \iota \in [-1, 1]$, and S_h for O2 [111] in a 1 Hz band around $f_{\mathcal{D}}$.

- v. \mathcal{D} taken from [99] and converted from PowerFlux circular/linear polarisation upper limits to population-averaged upper limits using conversion factors given in [101].
- w. \mathcal{D} derived from $h_0(f_{\mathcal{D}})$ upper limit quoted in reference, converted from PowerFlux circular polarisation upper limits to population-averaged upper limits using the conversion factors given in [101], and S_h for O1 [110] in a 1 Hz band around $f_{\mathcal{D}}$.
- x. \mathcal{B}_{bin} computed using Eq. (71) for fixed range of frequency modulation depth Δf_{obs} .